

Nonequilibrium dynamics in nanoscale resonators driven by mesoscopic conductors

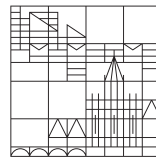
**Dissertation zur Erlangung des
akademischen Grades eines Doktors
der Naturwissenschaften
(Dr.rer.nat.)**

vorgelegt von

Mantovani, Mattia

an der

Universität
Konstanz



Mathematisch-Naturwissenschaftliche Sektion
Fachbereich Physik

Tag der mündlichen Prüfung: 30.10.2020

1. Referent: Dr. Gianluca Rastelli

2. Referent: Prof. Dr. Guido Burkard

Preface

The work presented in this Dissertation has been carried out during my PhD studies under the supervision of Dr. Gianluca Rastelli and Prof. Dr. Wolfgang Belzig between May 2017 and March 2020 in the Quantum Transport Group of the Department of Physics, Universität of Konstanz. The results presented in Chapters 3,¹ 4² and 5³ are published as articles in peer-reviewed international journals. Except where the references are made, this Thesis is entirely the outcome of multiple scientific collaborations established by Dr. Rastelli and Prof. Belzig and thereby contains a lot of valuable inputs from their side. The numerical code implemented to obtain the results of this Dissertation has been developed by me. Dr. Robert Hussein from the University of Konstanz is greatly acknowledged for the fruitful discussions and the technical support received during the path that led to the work presented in Ch. 4. I would like to appreciate here the hospitality received from Prof. Dr. Andrew Armour at the University of Nottingham, during my visits in February 2017 and February 2019, that led to the development of the results presented in Chs. 3 and 5.

¹**M. Mantovani**, A. D. Armour, W. Belzig, and G. Rastelli, *Dynamical multistability in a quantum-dot laser*, Phys. Rev. B **99**, 045442 (2019).

²**M. Mantovani**, W. Belzig, G. Rastelli, and R. Hussein, *Single-photon pump by Cooper-pair splitting*, Phys. Rev. Research **1**, 033098 (2019).

³W. T. Morley, A. Di Marco, **M. Mantovani**, P. Stadler, W. Belzig, G. Rastelli, and A. D. Armour, *Theory of double Cooper-pair tunneling and light emission mediated by a resonator*, Phys. Rev. B **100**, 054515 (2019).

Abstract

In hybrid quantum circuits, different mesoscopic systems can be combined to harness advantages and properties of each constituent, facilitating the unraveling of new phenomena which surmount the usual paradigm of light-matter interaction. Specifically, they can exhibit complex behavior as they operate far from equilibrium, and strong nonlinear interactions can emerge. Furthermore, their open dynamics due to the unavoidable coupling to the environment can be tailored using engineered reservoirs. In this Thesis, I have addressed these fundamental aspects in three specific systems formed by mesoscopic conductors and quantum dots coupled to localized resonators.

First, I have considered a solid-state implementation of a single-atom laser in a quantum-dot spin valve, where electronic spin is coupled to a harmonic oscillator. A spin-polarized current injected in the dot induces lasing, whereby energy is pumped with high efficiency into the resonator. This pumping mechanism rapidly leads to a breakdown of the widely employed rotating-wave approximation (RWA) without any requirement of ultrastrong light-matter coupling. Such RWA breakdown is associated with multistability of the resonator, characterized by multiple peaks in its Fock distribution and detectable with simple current measurements displaying telegraph dynamics.

In a second work, I have examined a Cooper-pair splitter consisting of two quantum dots, each coupled capacitively to a local resonator and a common superconductor. I derived an effective Hamiltonian validated by numerical simulations, and I demonstrated that the process of cross-Andreev reflection can be used to pump nonlocally single photons between the two resonators or to simultaneously cool them into their ground state. The system has possible applications such as coherent heat-control, cooling with single-photon precision, and microwave photon buses.

The third system that I studied consists of a Josephson junction in series with an electromagnetic resonator. When a voltage is applied to the junction, such that each Cooper pair can provide half the energy to generate a cavity photon, charge transport and photon emission can be dominated by effective inelastic tunneling of two Cooper pairs. The system displays a crossover from incoherent to coherent double Cooper-pair tunneling and can be further used as a single-photon source due to a form of photon-blockade effect.

Zusammenfassung

In hybriden quanten Schaltkreisen können verschiedene mesoskopische Systeme kombiniert und dabei die Vorteile und Eigenschaften der einzelnen Komponenten genutzt werden, um das Auftreten neuer Phänomene zu ermöglichen, welche die üblichen Paradigmen der Licht-Materie Wechselwirkung umgehen. Speziell können sie komplexes Verhalten entfalten wenn sie weit entfernt von ihrem Gleichgewichtszustand arbeiten, und nichtlineare Wechselwirkungen können hervorgehen. Ferner kann ihre, aufgrund der unausweichlichen Kopplung an die Umgebung, entstehende dissipative Dynamik mittels reservoir engineering nachvollzogen werden. In dieser Dissertation habe ich diese fundamentalen Aspekte anhand von drei spezifischen Systemen, bestehend aus mesoskopischen Leitern und an Resonatoren gekoppelten Quantenpunkten, adressiert.

Zunächst habe ich eine Festkörper Implementierung eines Einatom-Lasers in einem Quantenpunkt Spin-Ventil beschrieben, in welchem der elektronische Spin an einen Harmonischen Oszillator gekoppelt ist. Das Injizieren eines Spin-polarisierten Stroms in den Quantenpunkt induziert Lasing, wobei Energie mit hoher Effizienz in den Resonator gepumpt wird. Dieser Pump-Mechanismus führt sehr schnell auf ein Versagen der üblich verwendeten rotating wave approximation (RWA), ohne jegliche Anforderung einer ultrastarke Licht-Materie Wechselwirkung.

Solch ein Versagen der RWA führt zu einer Multistabilität des Resonators. Diese ist durch mehrere Peaks in seiner Fock-Verteilungsfunktion charakterisiert und durch einfache Strommessungen, welche Telegraphendynamik anzeigen, messbar.

In einem zweiten Projekt habe ich einen Cooper Pair Splitter untersucht, der aus zwei Quantenpunkten besteht, welche jeweils kapazitiv an einen lokalen Resonator und an einen gemeinsamen Supraleiter gekoppelt sind. Ich berechne einen effektiven Hamiltonoperator, validiert mittels numerischer Simulation, und demonstriere, dass der Prozess der Andreev Reflexion benutzt werden kann um nichtlokal einzelne Photonen zwischen den beiden Resonatoren zu transportieren, oder um beide gleichzeitig in ihren Grundzustand zu kühlen. Dieses System hat mögliche Applikationen in der kohärente Temperaturkontrolle, im Kühlen mit Ein-Photon Präzession und kann für Mikrowellenphotonenbusse benutzt werden.

Das dritte System das ich untersucht habe besteht aus einem Josephson Kontakt in Reihe geschaltet mit einem elektromagnetischen Resonator. Wenn eine Spannung an dem Josephson Kontakt angelegt wird, sodass jedes Cooper Paar die halbe Energie zum Erzeugen eines Photons in der Kavität beitragen kann, besteht die Möglichkeit, dass der Ladungstransport und die Photon Emission durch ein effektives Tunneln von zwei Cooper Paaren dominiert ist. Das System zeigt einen Übergang von inkohärentem zu kohärentem Doppel-Cooper-Paar Tunneln und kann des Weiteren wegen eines Photon-Blockade Effekts

als Einzel-Photon Quelle verwendet werden.

Contents

Preface	v
Abstract	vii
Zusammenfassung	ix
1 Introduction	1
1.1 Coupling light and matter: Cavity quantum electrodynamics	1
1.2 Light-matter coupling in hybrid systems: beyond the atomic QED architecture	3
1.2.1 Quantum dots	3
1.2.2 Superconducting devices	4
1.2.3 Electromagnetic cavities and mechanical resonators	6
1.2.4 Engineering the interaction	7
1.3 Structure of this Thesis and goals	8
2 Theory of the quantum master equation	9
2.1 Introduction	9
2.2 Microscopic derivation of the quantum master equation	9
2.2.1 Liouville-von Neumann equation	10
2.2.2 Interaction picture	11
2.2.3 Born approximation	12
2.2.4 Markov approximation	13
2.2.5 Secular approximation	14
2.2.6 Master equation in the energy representation	16
2.2.7 Equivalence to rate equations	17
2.3 Solution of the master equation	17

2.3.1	Analytical techniques	17
2.3.2	Numerical techniques	19
3	Dynamical multistability in a quantum-dot laser	25
3.1	Introduction	25
3.2	Quantum-dot laser in the spin-valve setup	26
3.3	Quantum master equation	27
3.4	Single-atom laser within the rotating-wave approximation (RWA)	29
3.4.1	RWA Hamiltonian and Jaynes-Cummings model	29
3.4.2	Density matrix theory	30
3.4.3	Semiclassical theory	32
3.5	Beyond the rotating-wave approximation: Multistability	34
3.5.1	Semiclassical equations beyond RWA	36
3.5.2	Multistability analysis of the resonator	39
3.6	Detecting lasing and multistability with transport measurements	41
3.6.1	Current jumps and two-state model	41
3.7	Experimental feasibility: Multistability in nonideal cases	44
3.7.1	Effect of finite temperature and finite polarization	44
3.7.2	Effect of spin relaxation	44
3.7.3	Effect of Duffing nonlinearity	46
3.7.4	Implementations	46
3.8	Conclusions	47
4	Single-photon pump by Cooper-pair splitting	49
4.1	Introduction	49
4.2	Double-quantum-dot Cooper-pair splitter coupled to resonators	50
4.2.1	Cooper-pair splitter in quantum-dot setup	50
4.2.2	Large-gap and large-Coulomb-repulsion limit	51
4.2.3	Capacitive coupling to resonators	52
4.3	Master equation and stationary current	52
4.3.1	Large bias limit and stationary current in the absence of resonators	53
4.4	Polaron transformation and effective Hamiltonian	55
4.5	Simultaneous ground-state cooling of nanoresonators	56

4.6	Photon transfer between resonators	58
4.7	Efficiency	59
4.8	Higher-order resonances	60
4.9	Conclusions	61
5	Theory of double Cooper-pair tunneling and light emission mediated by a resonator	63
5.1	Introduction	63
5.2	Josephson junction coupled to a microwave cavity	63
5.3	Effective Hamiltonian description	65
5.4	Results for the average photon number	66
5.4.1	Semiclassical interpretation	68
5.5	Analysis of the charge transport	69
5.5.1	Average current and Cooper-pair tunneling rate	69
5.5.2	From incoherent to coherent double-Cooper-pair tunneling	70
5.6	Photon blockade and single-photon emission	71
5.7	Conclusions	72
6	Conclusions and outlook	73
A	Complements to the derivation of the master equation	75
A.1	Hermiticity of the interaction operators	75
A.2	Vanishing expectation values of single operator	75
B	Steady-state Fock distribution for the resonator in RWA	77
C	Full-counting statistics of charge transport	81
C.1	Basic concepts	81
C.2	Vector representation	83
C.3	Moments and cumulants	83
C.4	Expression for the average current and the current noise	85
C.5	Note on the numerical evaluation of the noise	85
D	Operators $\mathcal{G}(\Delta_0, n)$, $\mathcal{F}(\Delta_0, n)$ and matrix element $\langle 1 H_{\text{eff}} 2\rangle$	87
	Scientific contributions	89

Curriculum Vitae	91
References	93

Chapter 1

Introduction

1.1 Coupling light and matter: Cavity quantum electrodynamics

One of the most successful and ever-developing applications of the quantum theory is the investigation of the interaction between *light* and *matter*. Historically, the first experiments involved real atoms interacting with the quantized electromagnetic field of optical and microwave cavities, within the framework commonly referred to as cavity quantum electrodynamics (QED) [1–3].

The paradigmatic model for the light-matter interaction is represented by the Rabi Hamiltonian [4, 5], given by

$$H_{\text{Rabi}} = \frac{\Delta\epsilon}{2}\sigma_z + \omega_0 b^\dagger b + g(\sigma_+ + \sigma_-)(b + b^\dagger). \quad (1.1)$$

It describes the coherent interaction between a two-level system (the *matter*, e.g., two levels of an atom or a spin-1/2) and a quantum harmonic oscillator (the *light*, e.g., a single mode of a microwave or optical cavity), see Fig. 1.1. The Rabi Hamiltonian follows from the interaction between the dipole moment of an atom and the electric field of the cavity, in the dipole approximation [6]. In Eq. (1.1), $\Delta\epsilon$ is the energy difference between the two levels and ω_0 is the resonance frequency of the harmonic oscillator. The constant g quantifies the strength of the interaction between light and matter.

The two-level system is composed of an excited ($|e\rangle$) and a ground ($|g\rangle$) state, which can be represented by two column vectors $|e\rangle = (1, 0)^T$ and $|g\rangle = (0, 1)^T$. In the basis $\{|e\rangle, |g\rangle\}$, the qubit is described by the raising and lowering operators $\sigma_+ = |e\rangle\langle g|$ and $\sigma_- = |g\rangle\langle e|$, which generate the Pauli operators $\sigma_x = \sigma_+ + \sigma_-$, $\sigma_y = -i(\sigma_+ - \sigma_-)$ and $\sigma_z = [\sigma_+, \sigma_-]$, with matrix form

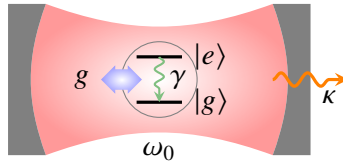


Figure 1.1: Sketch of a cavity QED setup. Two atomic levels of an atom, $|e\rangle$ and $|g\rangle$ with energy separation $\Delta\epsilon$ are coupled with strength g to a single mode of a cavity with resonance frequency ω_0 . The atom and the cavity are subject to decay at rates γ and κ , respectively, due to the interaction with the environment.

$$\sigma_x = \begin{pmatrix} 0 & 1 \\ 1 & 0 \end{pmatrix}, \quad \sigma_y = \begin{pmatrix} 0 & -i \\ i & 0 \end{pmatrix}, \quad \sigma_z = \begin{pmatrix} 1 & 0 \\ 0 & -1 \end{pmatrix}. \quad (1.2)$$

The harmonic oscillator is described by the bosonic field annihilation and creation operators, b and b^\dagger .

The exact eigenenergies of Hamiltonian (1.1) have been found only several decades after the first works of Rabi, and can only be written as the roots of a complex transcendental function [7]. The primary way of simplifying the Rabi Hamiltonian is to assume a *small* value of the coupling strength, $g \ll \{\omega_0; \Delta\epsilon\}$ and consider the two systems to be close to resonance, i.e., $\Delta\epsilon \approx \omega_0$. This permits to apply the rotating-wave approximation (RWA) to obtain the Jaynes-Cummings (JC) Hamiltonian [8]:

$$H_{\text{JC}} = \frac{\Delta\epsilon}{2} \sigma_z + \omega_0 b^\dagger b + g(\sigma_+ b + b^\dagger \sigma_-), \quad (1.3)$$

which can be exactly solved, see Ch. 3.

The Rabi model has been extended to two-photon interactions, where b and b^\dagger are replaced by b^2 and $(b^\dagger)^2$ [9], and to N -level atoms [10]. Similarly, extensions of the JC model with a single cavity mode coupled to many two-level systems (Dicke model [11] and Tavis-Cummings models [12, 13]) have been devised and implemented.

When dealing with a cavity QED experiment, an important role is played by the surroundings of the light-matter system: Atoms and cavities are coupled not only to each other—which is desired—but also to the measurement apparatus and to the thermal environment. This leads to inevitable relaxation and decoherence in the system, which in most cases can be captured by spontaneous emission rate γ for the atom and decay rate κ for the cavity (see Ch. 2). Based on the intensity of the coupling strength g compared to the decay rates and to the cavity and qubit frequencies, different regimes can be distinguished:

Weak-coupling regime, $g \lesssim \{\gamma; \kappa\}$: In this case g is not strong enough to observe coherence, because the energy is lost from the system before it can be exchanged between atom and cavity. Nevertheless, the coupling to the radiation field yields an enhancement of the spontaneous emission rate of the atom, a phenomenon known as Purcell effect [14].

Strong-coupling regime, $g \gg \{\gamma; \kappa\}$: When g is strong enough to overcome the losses, the coherent exchange of energy between light and matter can be observed. This corresponds to the regime of validity of the JC model. The development of resonators with larger quality factors $Q = \omega_0/\kappa$, associated with lower decay rates, led to the observation of vacuum Rabi oscillations in superconducting microwave cavities coupled to ensembles of Rydberg atoms [15] and later to a single atom [16–18], vacuum Rabi splitting [19], collapse and revival of oscillations in the atomic population [20], and sub-Poissonian photon statistics [21]. The achievement of strong coupling is crucial to control and manipulate quantum systems and for quantum information processing.

Ultrastrong-coupling regime, $g \sim \{\omega_0; \Delta\epsilon\}$: When g becomes comparable to the typical energy separation of atom and cavity, several nonperturbative effects come into play [22–24]. In contrast to the JC physics, states with different number of excitations starts to be hybridized. Ultrastrong

coupling has been first realized outside the cQED domain, in a superconducting flux qubit coupled to a coplanar-waveguide resonator [25].

Deep strong-coupling regime, $g > \{\omega_0; \Delta\epsilon\}$: In this extreme regime, the light-matter coupling exceeds the subsystems bare energy [26]. Also in this case, superconducting qubits allowed observation of unprecedentedly high values of g [27, 28]. Currently, the highest ratio of $g/\omega_0 \approx 1.43$ has been measured in metamaterials coupled to cyclotron resonances [29].

1.2 Light-matter coupling in hybrid systems: beyond the atomic QED architecture

In the last decades, the technological advance in fabrication and control of solid-state devices has paved the way for the realization of the QED protocol in several different platforms. In 1992, Weisbuch and co-workers first observed vacuum Rabi splitting in GaAlAs/AlAs quantum wells coupled to an optical microcavity [30]. More than a decade later, strong coupling was observed between a single quantum dot and a photonic crystal [31]. Gradually, the use of semiconducting artificial atoms in connection with microwave cavities and normal-metal or superconducting contacts became a well-established theoretical and experimental route to design mesoscopic QED systems [32–36]. The works pertaining to this Thesis fall primarily into this domain. Simultaneously to quantum-dot-based devices, the increasing importance of superconducting qubits resulted in the parallel development of the field of circuit QED [37–40]. Fostered by outstanding experimental outcomes, these two main classes of *hybrid* systems stimulated theorists to apply this idea in more exotic contexts involving, e.g., topological superconductors [41] and topological waveguides [42]. Finally, spin ensembles [43, 44] and magnons [45, 46] coupled to microwave cavities are building blocks in *cavity magnomechanics* [47] and *cavity optomagnonics* [48].

Each component of an hybrid system offers diverse intrinsic properties and features, which can then be combined in several ways in order to tailor the energy exchange mechanisms and let specific coherent interactions emerge. On the other hand, the same Hamiltonian can be implemented in radically different experimental contexts to explore broader regions of the parameter space. Finally, hybrid platforms allow to design, to some accuracy, the environmental surroundings of a system, uncovering novel phenomena arising from the complex open-system dynamics.

To better understand the working principles and the physics underlying a typical solid-state hybrid circuit, I quickly review below their main elements, and later discuss examples of how they can be coupled to realize light-matter coupling.

1.2.1 Quantum dots

Quantum dots (QDs) are artificial structures with sizes ranging from several nanometers to a few micrometers that can be realized on many platforms [49–52]. The goal is to trap a small integer number of electrons in a potential well, by controlling an electrostatic potential landscape using a set of gated electrodes. The confining potential gives rise to discrete and tunable electronic energy levels, thus realizing an artificial atom. By contacting the QDs with metallic electrodes made out of normal metals,

ferromagnets, or superconductors, it is possible to set up quantum transport experiments in a variety of configurations. Quantum dots can be fabricated in GaAs/AlGaAs heterostructures, in InSb, InAs, Si/SiGe semiconducting nanowires, carbon nanotubes [53], Si [54] and Ge [55], and graphene [56–60]. Furthermore, quantum-dot devices have received great attention lately because of their potential applications as quantum computers [49, 61].

1.2.2 Superconducting devices

Josephson junctions

The Josephson effect is arguably the most important consequence of superconductivity [62–64]. It predicts an equilibrium Cooper-pair current flowing between two superconductors when they are separated by a weak link, with no bias voltage applied (dc-Josephson effect). The current is related to the phase difference ϕ of the superconducting condensates, and is given by

$$I = I_c \sin \phi, \quad (1.4)$$

where the critical current I_c corresponds to the maximum current. A constant bias voltage V applied across the junction leads to the ac-Josephson effect: The phase difference will evolve in time according to

$$\dot{\phi} = -\frac{2eV}{\hbar}, \quad (1.5)$$

which leads to an ac-current of amplitude I_c and Josephson frequency $\omega_J = 2eV/\hbar$.

From Eqs. (1.4) and (1.5), the electrical work done by a current source to change the phase difference $\Delta\phi$ is given by $I(t)V = \frac{\hbar}{2e}I(t)(\Delta\dot{\phi})$. Integration in time yields the free energy

$$F = \text{const.} - \frac{\hbar I_c}{2e} \cos \phi, \quad (1.6)$$

which is minimum for $\Delta\phi = 0$. The Josephson effect can be formally derived using the Ginzburg-Landau (GL) theory, by considering two bulk superconductors separated by a short link of length $L \ll \xi$, where ξ is the coherence length in the superconductors [65]. Solving the GL equation leads to the system free energy

$$F = \frac{\hbar I_c}{2e} (1 - \cos \phi), \quad (1.7)$$

In agreement with Eq. (1.6). The critical current I_c is proportional to A/L , where A is the cross-section surface area of the junction.

To study the dynamics of a Josephson junction in presence of a bias current and finite voltage, it is useful to resort to RCSJ model, in which one considers a circuit made up by an ideal Josephson junction shunted in parallel by a resistance R and a capacitance C [66]. Given a bias current I , the phase difference across the junction obeys the differential equation

$$\frac{d^2\phi}{d\tau^2} + \frac{1}{Q} \frac{d\phi}{d\tau} + \sin \Delta\phi = \frac{I}{I_c}. \quad (1.8)$$

I have introduced the dimensionless variable $\tau = \omega_p t$, with the plasma frequency and quality factor of the junction defined, respectively, as

$$\omega_p = \sqrt{\frac{2eI_c}{\hbar C}}, \quad Q = \omega_p RC. \quad (1.9)$$

In full analogy with a mechanical system, Eq. (1.8) is equivalent to the equation of motion of a particle of mass $(\hbar/2e)^2 C$, moving along the coordinate ϕ , in a potential

$$U(\phi) = -E_J \cos \phi - \frac{\hbar I}{2e} \phi, \quad (1.10)$$

with a velocity-dependent *damping force* given by $(\hbar/2e)^2 (1/R) d\phi/d\tau$. The quantity $E_J = \hbar I_c/2e$ is known as *Josephson energy*. The potential (1.10) is usually referred to as *tilted washboard potential*.

While the above analysis assumes that the phase difference, ϕ , and the charge $Q = CV$ on the junction are classical variables, the variances $\Delta\phi$ and ΔN are related by the quantum uncertainty relation $\Delta\phi\Delta N \gtrsim 1$, where $N = Q/2e$ is the number of Cooper pairs transferred across the junction. This implies that ϕ and N cannot be known with arbitrary precision, giving rise to quantum fluctuations both in the phase and charge. By promoting ϕ and N to operators, one can write the Hamiltonian of an isolated Josephson junction at $T = 0$, without bias current, as

$$H = -E_J \cos \phi + \frac{Q^2}{2C} = -E_J \cos \phi - 4E_C \frac{\partial^2}{\partial \phi^2}, \quad (1.11)$$

where I have made the canonical replacement $N \rightarrow i\partial/\partial\phi$, and defined the charging energy of the junction, $E_C = e^2/2C$. The ratio $4E_C/E_J$ controls the interplay between charge and phase fluctuations. For a small junction, with $C \approx 1$ fF, the junction behaves as a particle with very small *mass*. This implies $E_C \gg E_J$, and that fluctuations in phase ϕ are large. The ground-state wavefunction $\psi(\phi)$ of the junction approaches a constant value. Conversely, for large junctions, $E_C \ll E_J$, meaning that the wavefunction is peaked around the minimum of the potential $\phi = 0$, similarly to a heavy particle in a potential well. In this case, charge fluctuations dominate. Notice that, in this regime, the junction behaves as a nonlinear (anharmonic) oscillator, with the nonlinearity given by the cosine form of the potential. The intrinsic nonlinearity of a Josephson junction is key for the implementation of superconducting qubits, which I briefly review below.

Superconducting qubits

Superconducting (SC) qubits are macroscopic circuit elements that behave quantum mechanically and exhibit observable coherence [67–69]. Typically, SC qubits are anharmonic oscillators, where the separation of energy levels is made nonuniform by introducing a nonlinearity through Josephson junctions. The anharmonicity is crucial to encode a qubit and perform gate operations involving only two states.

A central parameter in the design of a SC qubit is the ratio between the charging energy E_C and the Josephson energy E_J . According to this ratio and to the circuit topology, SC qubits are usually divided in three main classes: charge, flux (or persistent-current), and phase qubits.

The charge qubit, or Cooper-pair box, was the first superconducting circuit in which temporal coherence was first observed [70]. It consists of a small superconducting island connected to a large superconducting reservoir via a Josephson junction, and it is characterized by $E_C/E_J \geq 1$, such that the charge on the island is a good quantum number. They can have large anharmonicity, but are generally affected by strong charge noise, which limits their coherence time. To circumvent this problem, a large shunt capacitor can be added to the circuit, realizing the *transmon* [71], which is characterized by $E_J/E_C \gtrsim 50$ and is insensitive to charge noise. Transmons are currently the most widely used qubits for high-fidelity quantum gates, and have been employed in the first experimental demonstration of quantum supremacy [72].

In flux qubits [73–76], a superconducting loop threaded by an external magnetic flux Φ_{ext} is interrupted by one, three or more Josephson junctions. They are characterized by $E_J/E_C \sim 50$ and are generally affected by flux noise, since they need a large self-inductance. Flux qubits are the predominant elements in quantum annealing setups, such as the commercial system D-Wave [77].

Phase-qubit circuits consists of large Josephson junctions in the regime $E_J/E_C \sim 10^6$ [78–81]. These circuits can be described by the tilted-washboard potential (1.10), which is controlled by an applied bias current I very close to the critical current I_c of the junction. Phase qubits have small anharmonicity, but are insensitive to offset-charge noise because of the large E_J/E_C ratio.

Many extensions and optimizations of the above qubits have been devised in order to mitigate detrimental effects. The first improvement to the original Cooper-pair box design led to the *quantrionium* [82] with $E_J/E_C \sim 1$ (also called *charge-flux qubit*). To reduce the flux sensitivity in flux qubits, the loop size can be reduced, introducing however charge noise. For this reason, the small junction of a three-junction flux qubit can be shunted by a large capacitance [83]. The shunt-capacitor design has been implemented also for the phase qubit [84]. Other variations of the three basis SC qubits include *four-junction flux qubit* [85], *tunable-gap flux qubit* [86], *fluxonium* [87], *xmon*, *gmon* and *gatemon* qubits [88–90]. Finally, a recent realization of a $0 - \pi$ qubit holds the promise for the implementation of fault-tolerant quantum processors [91].

1.2.3 Electromagnetic cavities and mechanical resonators

The other basic ingredient of a mesoscopic QED device is the cavity, which is described by a quantized bosonic field that can exchange energy with the artificial atoms. Typically, a single resonant mode of given frequency is considered for each cavity. Any real cavity has a finite quality factor Q , which is connected to its energy decay rate κ through $Q = \omega/\kappa$ (ω is the resonance frequency of the mode).

Optical cavities have first been used in QED experiments and consist of conventional Fabry-Perot cavities with large Q up to 10^8 [92]. They provide ideal coupling to atoms and spins, through dipole and magnetic interaction, respectively. Beside the Fabry-Perot cavities, other resonators working in the optical regime have been envisaged, such as microsphere [93], microtoroidal [94], and photonic band-gap cavities [95].

In the microwave regime, cavities are usually fabricated on-chip in superconducting circuits. In the coplanar waveguide (transmission line) geometry, the resonator is built out of two ground conductors on the side of a central superconducting wire, with two capacitors on the ends playing the role of the mirrors of a conventional Fabry-Perot cavity [38, 96–98]. To achieve microwave frequencies, the size of a waveguide is in the millimeter range, with quality factors of order $Q \approx 10^3 - 10^4$. Another example of microwave resonator is offered by LC resonators, composed by an inductor and a capacitor, with resonance frequency $\omega = 1/\sqrt{LC}$.

Nanomechanical resonators have attracted considerable interest in the last decade, because their ability to respond to electrical and magnetic fields can lead to ultrasensitive force detectors [99, 100]. On the other hand, they can be coupled to two- or few-level systems to investigate, prepare and detect quantum states of mechanical vibration, or serve as a hybrid quantum information processing platform. Mechanical resonators can vibrate at frequencies ranging from tens of MHz to a few GHz [101] with ultrahigh quality factors [102]. Because of the low frequency, the thermal energy $k_B T$ is usually larger than the vibrational energy $\hbar\omega$. Hence, resonators need to be actively cooled in order to exhibit quantum behavior. To this end, great theoretical [103–108] and experimental [109–114] effort has been devoted to the development of cooling setups. Diverse types of mechanical resonators include cantilevers, doubly-clamped beams, carbon nanotubes, nanodrums and membranes [101].

1.2.4 Engineering the interaction

The building blocks described above can be coupled together in order to realize hybrid systems that enhance the properties and the advantages of its constituents. Utilizing the charge degree of freedom, quantum dots can be dipole-coupled to microwave cavities [115, 116] achieving strong coupling of single electrons to photons [117–120]. The coupling can also be realized using mechanical resonators such as carbon nanotubes [121, 122].

Other efforts have been focused on coupling electronic *spin* to mechanical resonators [99, 107, 123], or to realize an effective spin-photon coupling based on spin-charge and charge-photon coupling with quantum dots and microwave cavities [124–129].

Beyond the typical *light-matter* paradigm, other hybrid implementations have been oriented to couple different oscillators: The optomechanical setup aims at achieving strong coupling between mechanical and optical or microwave resonators exploiting the radiation pressure mechanism [130, 131], while recently, indirect coupling of macroscopic mechanical resonators has been demonstrated [132–134].

The mesoscopic QED architecture with quantum dots is not simply an alternative tool to reproduce atomic or circuit QED experiments. First, quantum transport is an important ingredient as it can drive the system out of equilibrium. Hence, microwave photons can help to probe and detect these nonequilibrium states [135–137]; on the other hand, microwave or mechanical cavities can themselves exploit the out-of-equilibrium charge dynamics and become highly excited [138–144]. The present Thesis will predominantly focus on this aspect. Secondly, the interface between the conductors and the quantum dots can be made highly transparent, therefore increasing the tunnel coupling strength. For superconducting contacts, this can lead to coherent splitting and recombination of Cooper pairs [145,

146]. In other setups, strong induced correlation can enable detection of exotic states of matter, such as Kondo resonances [147, 148] or Majorana bound states [149, 150].

1.3 Structure of this Thesis and goals

The main goal of this Thesis is to discuss and investigate a family of hybrid setups where quantum dots (or Josephson junctions) are coupled to bosonic cavities (nanomechanical resonators or superconducting microwave cavities), and drive the latter into highly nonequilibrium states through electron tunneling events. I outline below the content of each Chapter:

- In Ch. 2 I introduce the theoretical and numerical framework upon which the main results are obtained, i.e., the Markovian quantum master equation to study the evolution of typical mesoscopic QED architectures.
- In Ch. 3 I discuss a solid-state implementation of a single-atom maser, which is realized using a quantum dot in a spin-valve configuration between ferromagnetic contacts; I show how the systems exhibits unique features, such as the breakdown of the rotating-wave approximation, widely used in the light-matter interaction context, and a multistable lasing regime.
- In Ch. 4 I present a single-photon pump device based on a quantum-dot implementation of a Cooper-pair splitter, where an effective coupling between two distant harmonic resonators can be activated through Cooper-pair transport from a superconducting contact. This enables an efficient photon transfer mechanism, as well as cavity ground-state cooling.
- In Ch. 5 I examine the theory of double-Cooper-pair tunneling in a voltage-biased Josephson junction coupled to a microwave resonator. I analyze the transition regime between coherent and incoherent double-Cooper-pair tunneling, and further show how the system can be used as a single-photon source.
- In Ch. 6 I draw the conclusions and give an outlook on the work presented.

Chapter 2

Theory of the quantum master equation

2.1 Introduction

Any realistic investigation of a quantum system requires taking into account its coupling to the rest of the world. Therefore, the derivation of a suitable equation describing the dynamics of the density matrix of a system is the primary ingredient both in the theoretical analysis and in the validation of experimental data. In this Chapter, I will focus on a class of master equations that can describe faithfully the solid-state devices presented in the following Chapters of the Thesis. Typically, these systems follow a Markovian dynamics, since they are weakly coupled to an environment with many degrees of freedom, and system-environment correlations are lost quickly when compared to the timescale on which the state of the system varies appreciably.

The most general form of a Markovian master equation can be rigorously formulated in terms of the generator of a quantum dynamical semigroup, giving rise to the standard Gorini-Kossakowski-Sudarshan-Lindblad (GKLS or, more commonly, Lindblad) equation [151, 152]. Here, I will instead focus on a derivation of the master equation which follows a well-developed microscopic approach and leads to the Bloch-Redfield equation [153–155]. I will discuss critically the validity regime of the Bloch-Redfield equation, showing the condition under which it has a Lindblad form. After presenting the master equation, I will briefly summarize a few commonly used methods (analytical and numerical) to solve it.

2.2 Microscopic derivation of the quantum master equation

The general recipe to treat an open quantum system is to identify a *system*, representing the portion of the universe that one wants to closely investigate, which lives in an Hilbert space \mathcal{H}_S and is described by a Hamiltonian H_S and a density matrix ρ_S . The system is coupled to an *environment*, described by a state ρ_E in an Hilbert space \mathcal{H}_E , and Hamiltonian H_E . The coupling, realized through an interaction Hamiltonian H_I , induces system-environment correlations, such that the *reduced* dynamics of ρ_S can no longer be regarded as unitary (see Fig. 2.1). The total Hamiltonian of the universe may be written as

$$H(t) = H_S \otimes \mathbb{1}_E + \mathbb{1}_S \otimes H_E + H_I(t), \quad (2.1)$$

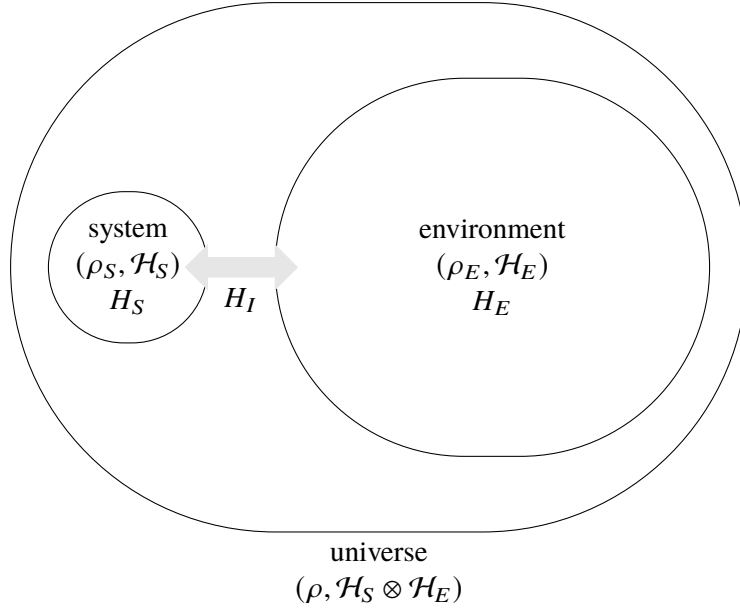


Figure 2.1: Schematic picture of an open quantum system. The universe may be subdivided into a system weakly coupled to an environment through the interaction Hamiltonian H_I .

where $\mathbb{1}_{\{E,S\}}$ are identity operators acting on the corresponding Hilbert space. The total Hamiltonian can be, in principle, time-dependent.

In order to make the problem tractable, many assumptions and approximations must be in order: One needs to isolate the relevant parts to be comprised in the model, discarding effects and interactions which can be safely neglected, and the system-environment coupling must be considered weak in a sense that will be later clarified. In a typical solid-state or QED device, the system is composed of a few-level atom, an artificial atom (a quantum dot or a superconducting qubit), a mechanical or electromagnetic resonator, as well as any coupled arrangement of the above. The environment usually consists of metallic contacts (fermionic baths of quasicontinuous states) or a bath of harmonic oscillators (substrate phonons, thermal excitations, quasiparticles) in thermal equilibrium, to which the system is naturally coupled, giving rise to relaxation and decoherence.

2.2.1 Liouville-von Neumann equation

The unitary evolution of the closed, isolated universe under Hamiltonian (2.1) is given by the Liouville-von Neumann equation for ρ [156],

$$\dot{\rho}(t) = -i[H(t), \rho(t)] \equiv \mathcal{L}(t)\rho(t). \quad (2.2)$$

We have introduced the Liouvillian superoperator \mathcal{L} , which will be of central importance throughout this work. The general solution to Eq. (2.2) is given by

$$\rho(t) = \mathcal{T} \exp \left[\int_0^t d\tau \mathcal{L}(\tau) \right] \rho(0), \quad (2.3)$$

where \mathcal{T} is the time-ordering operator and $\rho(0)$ denotes the state at the initial time. For a time-independent Liouvillian, Eq. (2.3) reduces to

$$\dot{\rho}(t) = \exp[\mathcal{L}t] \rho(0). \quad (2.4)$$

Equation (2.3) is equivalent to

$$\dot{\rho}(t) = U(t, 0) \rho(0) U^\dagger(t, 0), \quad (2.5)$$

with the time-evolution operator

$$U(t, 0) = \mathcal{T} \exp \left[-i \int_0^t d\tau H(\tau) \right], \quad (2.6)$$

which is unitary, $U(t, 0) U^\dagger(t, 0) = U^\dagger(t, 0) U(t, 0) = \mathbb{1}$, and satisfies

$$i \frac{\partial}{\partial t} U(t, 0) = H(t) U(t, 0). \quad (2.7)$$

2.2.2 Interaction picture

Equations (2.2)-(2.5) are written in the Schrödinger picture, where the time evolution of the system falls entirely on the state. The first step to obtain an equation for the reduced system density matrix ρ_S is move to the interaction picture with the respect to the coupling Hamiltonian H_I . Let us write the total Hamiltonian as $H(t) = H_0 + H_I(t)$, where the evolution (i.e., the spectrum) of $H_0 = H_S + H_E$ is known and given by

$$U_0(t, 0) = \exp[-iH_0t]. \quad (2.8)$$

The goal of the interaction picture is to split the global evolution as

$$U(t, 0) = U_0(t, 0) U_I(t, 0), \quad (2.9)$$

where the subscript $(\cdot)_I$ stands for “interaction picture”. For an operator O , the evolution of the expectation value on the full state ρ can be written as

$$\begin{aligned} \langle O(t) \rangle &= \text{Tr}[O \rho(t)] = \text{Tr}[O U(t, 0) \rho(0) U^\dagger(t, 0)] = \text{Tr}[O U_0(t, 0) U_I(t, 0) \rho(0) U_I^\dagger(t, 0) U_0^\dagger(t, 0)] \\ &= \text{Tr}[O_I(t) \rho_I(t)]. \end{aligned} \quad (2.10)$$

In the last line, we have used the cyclic property of the trace and defined

$$O_I(t) = U_0^\dagger(t, 0) O U_0(t, 0), \quad (2.11)$$

$$\rho_I(t) = U_I^\dagger(t, 0) \rho(0) U_I(t, 0) = U_0^\dagger(t, 0) \rho(t) U_0(t, 0). \quad (2.12)$$

Differentiating Eq. (2.12) with respect to time and using Eq. (2.9) leads to the Liouville-von Neumann equation in the interaction picture:

$$\dot{\rho}_I(t) = -i[H_I(t), \rho_I(t)]. \quad (2.13)$$

Notice that $H_I(t)$ is the interaction Hamiltonian transformed to the interaction picture according to Eq. (2.11).

To start the formal derivation of the master equation, it will be necessary to perform a partial trace over the degrees of freedom of the environment, in order to get an equation for the reduced density matrix of the system, $\rho_S = \text{Tr}_E[\rho]$. To this end, we will consider a specific form of the interaction Hamiltonian H_I , given by

$$H_I = \sum_{\alpha} A_{\alpha} \otimes B_{\alpha}, \quad (2.14)$$

where A_{α} are system operators and B_{α} are bath operators. In the interaction picture, Eq. (2.14) transforms into

$$H_I(t) = \sum_{\alpha} A_{\alpha,I}(t) \otimes B_{\alpha,I}(t), \quad (2.15)$$

using Eq. (2.11). We will assume throughout for simplicity hermitian operators $A_{\alpha} = A_{\alpha}^\dagger$ and $B_{\alpha} = B_{\alpha}^\dagger$, although this is not a strict requirement, as long as H_I is hermitian as a whole (see Appendix A.1).

The standard derivation of the master equation stems from perturbation theory applied to Eq. (2.13), under the assumption of *weak coupling* between the system and the environment, followed by the subsequent application of the Born, Markov and secular approximations [155]. Let us first integrate formally Eq. (2.13) and then insert the solution back on its right-hand side. After tracing over the environment, we obtain

$$\dot{\rho}_S = -i\text{Tr}_E\{[H_I(t), \rho(0)]\} - \int_0^t \text{Tr}_E\{[H_I(t), [H_I(t'), \rho(t')]]\} dt'. \quad (2.16)$$

Equation (2.16) is exact, but depends on the full density matrix ρ at all previous times.

2.2.3 Born approximation

The Born approximation relies on the fact that the environment is large, such that it is barely perturbed by the system, and the system-environment coupling is small: We assume that $H_I(t) \sim \mathcal{O}(\varepsilon)$, where ε is

a small perturbative dimensionless parameter. The density matrix at all times is then assumed to be of the form

$$\rho(t) = \rho_S(t) \otimes \rho_E + O(\varepsilon), \quad (2.17)$$

with the factorized initial density matrix $\rho(0) = \rho_S(0) \otimes \rho_E$. Notice that the presence of the $O(\varepsilon)$ term is crucial to induce correlations between the system and the environment, which allow the state of the system to evolve. After the Born approximation we obtain a perturbative expansion of Eq. (2.16) which is valid to second order in ε :

$$\dot{\rho}_S = -i\text{Tr}_E\{[H_I(t), \rho_S(0) \otimes \rho_E]\} - \int_0^t \text{Tr}_E\{[H_I(t), [H_I(t'), \rho_S(t') \otimes \rho_E]]\} dt' + O(\varepsilon^3). \quad (2.18)$$

We now make the assumption

$$\text{Tr}\{B_\alpha(t)\rho_E\} = 0. \quad (2.19)$$

This is not a restrictive condition, as it is always possible to modify the system Hamiltonian and the bath operators B_α to let the trace vanish (see Appendix A.2). Using the interaction Hamiltonian decomposition (2.14) and condition (2.19), Eq. (2.18) becomes

$$\dot{\rho}_S = - \sum_{\alpha\beta} \int_0^t dt' \{C_{\alpha\beta}(t, t') [A_\alpha(t), A_\beta(t') \rho_S(t')] + C_{\beta\alpha}(t', t) [\rho_S(t') A_\beta(t'), A_\alpha(t)]\}, \quad (2.20)$$

where we have defined the environmental correlation functions

$$C_{\alpha\beta}(t, t') = \text{Tr}\{B_\alpha(t) B_\beta(t') \rho_E\}. \quad (2.21)$$

2.2.4 Markov approximation

Equation (2.20) is closed (depends only on ρ_S), but it is non-Markovian, as ρ_S must be known at all previous times. However, under the weak-coupling and large-reservoir approximations, it is possible to obtain a Markovian expression.

The next assumption in our treatment consists in assuming that the state of the environment is stationary, i.e., it is in thermal equilibrium,

$$\rho_E = \frac{e^{-\beta H_E}}{\text{Tr}\{e^{-\beta H_E}\}}, \quad (2.22)$$

where β is the environmental inverse temperature. As a consequence, the environment Hamiltonian commutes with the bath density operator, $[H_E, \rho_E] = 0$. The correlation functions for a stationary bath

satisfy the property

$$C_{\alpha\beta}(t, t') = C_{\alpha\beta}(\tau \equiv t - t'), \quad (2.23)$$

with

$$C_{\alpha\beta}(\tau) = \text{Tr}\{e^{iH_E\tau} B_\alpha e^{-iH_E\tau} B_\beta \rho_E\}. \quad (2.24)$$

Assuming hermitian bath operators B_α , we will have additionally $C_{\alpha\beta}(\tau) = C_{\beta\alpha}^*(-\tau)$. The central idea behind the Markov approximation is that, when the environment is large and its spectrum becomes quasi-dense, the correlation functions $C_{\alpha\beta}(\tau)$ will be strongly peaked around $\tau = 0$ and will decay to zero *much faster* than the rate of variation of ρ_S . The consequence of this is twofold: first, we are allowed to replace $\rho_S(t')$ with $\rho_S(t)$ in Eq. (2.20); second, we can push the integration limits to $t \rightarrow \infty$. In order to do this, we just make the change of variable $\tau = t - t'$ in Eq. (2.20), obtaining

$$\dot{\rho}_S = - \sum_{\alpha\beta} \int_0^\infty d\tau \{C_{\alpha\beta}(\tau) [A_\alpha(t), A_\beta(t-\tau) \rho_S(t)] + C_{\beta\alpha}(-\tau) [\rho_S(t) A_\beta(t-\tau), A_\alpha(t)]\}. \quad (2.25)$$

After transforming back to the Schrödinger picture, we obtain

$$\begin{aligned} \dot{\rho}_S = & -i[H_S, \rho_S(t)] \\ & - \sum_{\alpha\beta} \int_0^\infty d\tau \{C_{\alpha\beta} [A_\alpha, e^{-iH_S\tau} A_\beta e^{iH_S\tau} \rho_S(t)] + C_{\beta\alpha}(-\tau) [\rho_S(t) e^{-iH_S\tau} A_\beta e^{iH_S\tau}, A_\alpha]\}. \end{aligned} \quad (2.26)$$

Equation (2.26) is known as the Bloch-Redfield master equation [153–155]; it is local in time and trace-preserving, but it is not guaranteed to preserve the positivity of the density matrix, because it cannot be generally put in a Lindblad form. To deal with this, the secular approximation must be employed.

2.2.5 Secular approximation

To apply the secular approximation, it is crucial to start with the *interaction picture* master equation (2.25). Let us define the energy eigenbasis of the system Hamiltonian

$$H_S |n\rangle = E_n |n\rangle, \quad (2.27)$$

allowing the possibility of degeneration ($E_n = E_m$ for $n \neq m$). We introduce the *spectral decomposition* of the system operators A_α through the relations

$$A_\alpha(\omega) = \sum_{nm} \delta(\omega_{mn} - \omega) |n\rangle \langle n| A_\alpha |m\rangle \langle m|, \quad (2.28)$$

$$A_\alpha^\dagger(\omega) = \sum_{nm} \delta(\omega_{nm} - \omega) |n\rangle \langle n| A_\alpha^\dagger |m\rangle \langle m|, \quad (2.29)$$

with the Bohr frequencies $\omega_{mn} = E_m - E_n$. The $A_\alpha(\omega)$ satisfy $\sum_\omega A_\alpha(\omega) = A_\alpha$, and in the interaction picture they become

$$e^{iH_S t} A_\alpha(\omega) e^{-iH_S t} = e^{-i\omega t} A_\alpha(\omega). \quad (2.30)$$

Introducing Eq. (2.30) into Eq. (2.25) we arrive at

$$\dot{\rho}_S = \sum_{\alpha\beta} \sum_{\omega\omega'} e^{i(\omega' - \omega)t} \Gamma_{\alpha\beta}(\omega) [A_\beta(\omega) \rho_S(t) A_\alpha^\dagger(\omega') - A_\alpha^\dagger(\omega') A_\beta(\omega) \rho_S(t)] + \text{H.c.}, \quad (2.31)$$

with the one-sided Fourier transforms of the bath correlation functions

$$\Gamma_{\alpha\beta}(\omega) = \int_0^\infty C_{\alpha\beta}(\tau) e^{i\omega\tau} d\tau. \quad (2.32)$$

The secular approximation consists in neglecting the terms with $\omega' \neq \omega$ in Eq. (2.31). For this to make sense, one must assume that the timescale on which ρ_S varies appreciably is *much larger* than the typical values of $|\omega' - \omega|^{-1}$, such that the fast oscillating exponential terms in Eq. (2.31) can be averaged out to zero if $\omega' \neq \omega$. Upon the secular approximation, we obtain

$$\dot{\rho}_S = \sum_{\alpha\beta} \sum_{\omega} \Gamma_{\alpha\beta}(\omega) [A_\beta(\omega) \rho_S(t) A_\alpha^\dagger(\omega) - A_\alpha^\dagger(\omega) A_\beta(\omega) \rho_S(t)] + \text{H.c.} \quad (2.33)$$

Now, we split the function $\Gamma_{\alpha\beta}(\omega)$ into

$$\begin{aligned} \Gamma_{\alpha\beta}(\omega) &= \frac{1}{2} \gamma_{\alpha\beta}(\omega) + \frac{1}{2} \sigma_{\alpha\beta}(\omega), \\ \Gamma_{\beta\alpha}^*(\omega) &= \frac{1}{2} \gamma_{\alpha\beta}(\omega) - \frac{1}{2} \sigma_{\alpha\beta}(\omega), \end{aligned} \quad (2.34)$$

where

$$\begin{aligned} \gamma_{\alpha\beta}(\omega) &= \Gamma_{\alpha\beta}(\omega) + \Gamma_{\beta\alpha}^*(\omega) = \int_{-\infty}^{+\infty} C_{\alpha\beta}(\tau) e^{+i\omega\tau} d\tau, \\ \sigma_{\alpha\beta}(\omega) &= \Gamma_{\alpha\beta}(\omega) - \Gamma_{\beta\alpha}^*(\omega) = \int_{-\infty}^{+\infty} C_{\alpha\beta}(\tau) \text{sgn}(\tau) e^{+i\omega\tau} d\tau. \end{aligned} \quad (2.35)$$

With the help of Eq. (2.34), rearranging the terms in Eq. (2.33) yields the Lindblad form

$$\dot{\rho}_S = -i[H_{LS}, \rho_S(t)] + \sum_{\omega} \sum_{\alpha,\beta} \gamma_{\alpha\beta}(\omega) \left[A_\beta(\omega) \rho_S(t) A_\alpha^\dagger(\omega) - \frac{1}{2} \{A_\alpha^\dagger(\omega) A_\beta(\omega), \rho_S(t)\} \right]. \quad (2.36)$$

The notation $\{\cdot, \cdot\}$ refers to the anticommutator. The operator

$$H_{LS} = \sum_{\omega} \sum_{\alpha\beta} \frac{1}{2i} \sigma_{\alpha\beta}(\omega) A_{\alpha}^{\dagger}(\omega) A_{\beta}(\omega) \quad (2.37)$$

is called Lamb-shift Hamiltonian, and its effect is a renormalization of the unperturbed energy levels of the system, arising from the system-environment coupling. In most practical applications (including the ones presented in this work) the Lamb shift is usually neglected. It can be shown that the matrix $\gamma_{\alpha\beta}(\omega)$ is hermitian and positive [155], hence it is diagonalizable with positive damping coefficients yielding a diagonal form of the master equation. In the special case where the energy dependence of the damping coefficients can be neglected, the Lindblad form is particularly simple and given by

$$\dot{\rho}_S = -i[H_{LS}, \rho_S(t)] - \sum_{\alpha} \gamma_{\alpha} \mathcal{D}(A_{\alpha}) \rho_S(t), \quad (2.38)$$

where I have introduced the *Lindblad dissipator* with operator A acting on the state ρ ,

$$\mathcal{D}(A)\rho = A\rho A^{\dagger} - \frac{1}{2}\{A^{\dagger}A, \rho\}. \quad (2.39)$$

2.2.6 Master equation in the energy representation

A sometimes useful representation of the master equation (without employing the spectral decomposition) is found by projecting Eq. (2.25) in the energy eigenbasis $|n\rangle$, which yields

$$\dot{\rho}_S = \sum_{\alpha\beta} \sum_{nmpq} \Gamma_{\alpha\beta}(\omega_{mn}) e^{i[\omega_{mn} - \omega_{qp}]t} (A_{\beta})_{nm} (A_{\alpha})_{pq}^* \{L_{nm}\rho_S(t)L_{pq}^{\dagger} - L_{pq}^{\dagger}L_{nm}\rho_S(t)\} + \text{H.c.} \quad (2.40)$$

We have introduced the shorthands $(A_{\alpha})_{nm} = \langle n|A_{\alpha}|m\rangle$ and $L_{nm} = |n\rangle\langle m|$ (the latter is the Lindblad jump operator in the energy representation). The secular approximation amounts here to neglecting all terms where $\omega_{nm} \neq \omega_{qp}$. The Lindblad form of the master equation in the Schrödinger picture reads

$$\dot{\rho}_S = -i[H_S + H_{LS}, \rho_S(t)] + \sum_{nmpq} \gamma_{nm,pq} \left[L_{nm}\rho_S(t)L_{pq}^{\dagger} - \frac{1}{2}\{L_{pq}^{\dagger}L_{nm}, \rho_S(t)\} \right]. \quad (2.41)$$

The Lamb-shift Hamiltonian is $H_{LS} = \sum_{nm} \sigma_{nm} L_{nm}$, with matrix elements

$$\sigma_{nm} = -\frac{i}{2} \delta_{\omega_{mn}} \sum_{\alpha\beta} \sum_p \sigma_{\alpha\beta}(\omega_{mp}) (A_{\beta})_{pm} (A_{\alpha})_{pn}^*, \quad (2.42)$$

and the damping coefficients in the dissipative part read explicitly

$$\gamma_{nm,pq} = \delta_{\omega_{mn}, \omega_{qp}} \sum_{\alpha\beta} \gamma_{\alpha\beta}(\omega_{mn}) (A_{\beta})_{nm} (A_{\alpha})_{pq}^*. \quad (2.43)$$

2.2.7 Equivalence to rate equations

A further, relevant simplification of the master equation can be made if the spectrum of the system Hamiltonian H_S is nondegenerate. In this case, the Kronecker delta functions appearing in the definitions of the damping coefficients simplify into $\delta_{\omega_{mn}} \rightarrow \delta_{mn}$. By looking at the equation for the populations of the density matrix, $\rho_{nn} = \langle n | \rho_S | n \rangle$, we obtain

$$\dot{\rho}_{nn} = \sum_m \gamma_{nm,nm} \rho_{mm} - \left[\sum_m \gamma_{mn,mn} \right] \rho_{nn}, \quad (2.44)$$

i.e., populations only couple to the populations, while the coherences (ρ_{nm} with $n \neq m$) decay to zero. The coefficients $\gamma_{nm,nm}$ correspond to the transition rates from state m to n , and are equivalent to those obtained by Fermi's golden rule:

$$\gamma_{nm,nm} = w_{n \leftarrow m} = \sum_{\alpha\beta} \gamma_{\alpha\beta}(\omega_{mn}) (A_\beta)_{nm} (A_\alpha)_{nm}^*. \quad (2.45)$$

Equation (2.44) is known as Pauli master equation. It allows to compute the evolution of an open system by taking into account only the populations of the eigenstates (which are N for a N -dimensional Hilbert space of the system) and not the full density matrix (composed of N^2 elements). Therefore, whenever the conditions to use it apply, it is of great numerical advantage for a large system.

2.3 Solution of the master equation

I briefly present here a number of analytical and numerical tools than can be used to solve the master equation, some of which are employed in the following Chapters of the Thesis. For simplicity, I will restrict to the case of a master equation with time-independent Liouvillian, $\dot{\rho}(t) = \mathcal{L}\rho(t)$, which can be put in the diagonal form of Eq. (2.38). I will drop the subscript S and reference to the system density matrix as ρ .

2.3.1 Analytical techniques

2.3.1.1 Equation of motion

The master equation for the density matrix can directly used to compute the dynamical evolution of the relevant expectation values of the system, by simply exploiting the relation $\langle O_i \rangle = \text{Tr}[O_i \rho]$, where $\{O_i\}$ is a family of system observables. Usually, this leads to a system of first-order linear differential equations involving the observables. If the system cannot be closed, further approximations may be required. It is worth stressing that for infinitely-dimensional Hilbert spaces (e.g., systems involving harmonic oscillators), this method is extremely useful. We write

$$\begin{aligned}
\langle \dot{O}_i \rangle &= \text{Tr}[O_i \dot{\rho}] = \text{Tr}[O_i \mathcal{L}\rho] \\
&= -i\langle [O_i, H + H_{LS}] \rangle + \sum_{\alpha} \gamma_{\alpha} \left[\langle A_{\alpha}^{\dagger} O_i A_{\alpha} \rangle - \frac{1}{2} \langle \{O_i, A_{\alpha}^{\dagger} A_{\alpha}\} \rangle \right].
\end{aligned} \tag{2.46}$$

For a finite-dimensional system, there exists a finite number of linearly independent observables $\{O_i\}$, hence one will end up with a linear system of the form

$$\langle \dot{O}_i \rangle = \sum_j M_{ij} \langle O_j \rangle, \tag{2.47}$$

where M_{ij} are the entries of a matrix \mathbf{M} .

2.3.1.2 Adjoint master equation and quantum regression theorem

Similarly to the Heisenberg evolution of closed systems, it is possible to derive a master equation in which the state is kept constant while the system operators are left to evolve. This might be simply implied from Eq. (2.47), yielding

$$\begin{aligned}
\dot{O}_i(t) &= -i[O_i(t), H + H_{LS}] + \sum_{\alpha} \gamma_{\alpha} \left[A_{\alpha}^{\dagger} O_i(t) A_{\alpha} - \frac{1}{2} \{O_i(t), A_{\alpha}^{\dagger} A_{\alpha}\} \right] \equiv \mathcal{L}^{\dagger} O_i(t) \\
&= \sum_j M_{ij} O_j(t)
\end{aligned} \tag{2.48}$$

which is known as adjoint master equation with the hermitian conjugate of the Liouvillian, \mathcal{L}^{\dagger} [155]. The time dependence in the operators implies we are working in the Heisenberg picture. Formally, this follows from the relation

$$\langle O_i \rangle(t) = \text{Tr}_S[O_i \rho(t)] = \text{Tr}_S[O_i e^{\mathcal{L}t} \rho] = \text{Tr}_S[(e^{\mathcal{L}^{\dagger}t} O_i) \rho], \tag{2.49}$$

from which we define $O_i(t) = e^{\mathcal{L}^{\dagger}t} O_i$. Differentiating with respect to time yields Eq. (2.48). The adjoint master equation becomes useful to calculate two-point correlation functions at different times, by knowing only single-point correlation functions (expectation values), a result known as quantum regression theorem [157, 158]. From

$$\frac{d}{d\tau} O_i(t + \tau) = \frac{d}{d\tau} e^{\mathcal{L}^{\dagger}(t+\tau)} O_i = \mathcal{L}^{\dagger} O_i(t + \tau) = \sum_j M_{ij} O_j(t + \tau), \tag{2.50}$$

it follows

$$\frac{d}{d\tau} \langle O_i(t + \tau) O_j(t) \rangle = \sum_j M_{ij} \langle O_i(t + \tau) O_j(t) \rangle, \tag{2.51}$$

i.e., the same matrix coefficients stemming from the dynamical equations of single operators can be used. Two-time correlation functions are extremely useful when working with open systems, as they

provide more statistical information than the expectation values. For example, the frequency spectrum of photons emitted from a cavity is given by the Fourier transform of the correlation function

$$g^{(1)}(\tau) = \langle a^\dagger(t + \tau)a(t) \rangle, \quad (2.52)$$

where a is the bosonic mode of the cavity.

2.3.1.3 Laplace transform

The Laplace transform method [159] is especially useful if one wants to compute the stationary state of a system, satisfying $\dot{\rho} = 0$. The Laplace transform is defined as

$$\tilde{\rho}(z) = \int_0^\infty dt e^{-zt} \rho(t), \quad (2.53)$$

from which one deduces

$$\tilde{\rho}(z) = \frac{1}{z\mathbb{1} - \mathcal{L}} \rho(0). \quad (2.54)$$

with the identity matrix in Liouville space, $\mathbb{1}$. The calculation of the inverse of the matrix $z\mathbb{1} - \mathcal{L}$ is much simpler than exponentiating $\mathcal{L}t$, but one is then left with the problem of inverting the Laplace-transformed $\tilde{\rho}(z)$ back to real time, which is usually achieved through contour integration in complex space after identification of the poles of $(z\mathbb{1} - \mathcal{L})^{-1}$. The stationary state of the system is formally obtained by taking the limit

$$\rho_{\text{st}} = \lim_{t \rightarrow \infty} \rho(t) = \lim_{z \rightarrow 0} z \tilde{\rho}(z). \quad (2.55)$$

2.3.2 Numerical techniques

2.3.2.1 Numerical integration

To propagate numerically a master equation $\dot{\rho} = \mathcal{L}\rho$ the general idea is time discretization into small time steps Δt . Explicit schemes rely on the recipe

$$\frac{\rho(t + \Delta t) - \rho(t)}{\Delta t} = \mathcal{L}\rho(t), \quad (2.56)$$

where \mathcal{L} is applied to the “known” $\rho(t)$, while implicit methods are, e.g.,

$$\frac{\rho(t + \Delta t) - \rho(t)}{\Delta t} = \mathcal{L} \frac{1}{2} [\rho(t) + \rho(t + \Delta t)]. \quad (2.57)$$

Other solution schemes exist, such as semi-implicit methods and splitting strategies. As an example of an explicit method widely used for its stability, I briefly outline the fourth-order Runge-Kutta method

[160]. For a choice of step size Δt , the density matrix at time $t + \Delta t$ (ρ_{n+1}) is calculated from the density matrix at time t (ρ_n) according to

$$\rho_{n+1} = \rho_n + \frac{1}{6}\Delta t(k_1 + 2k_2 + 2k_3 + k_4), \quad (2.58)$$

with

$$\begin{aligned} k_1 &= \mathcal{L}\rho_n, \\ k_2 &= \mathcal{L}\left(\rho_n + \frac{1}{2}\Delta t k_1\right), \\ k_3 &= \mathcal{L}\left(\rho_n + \frac{1}{2}\Delta t k_2\right), \\ k_4 &= \mathcal{L}(\rho_n + \Delta t k_3). \end{aligned} \quad (2.59)$$

The method applies the Liouvillian four times for each time step, and is indeed equivalent to the fourth-order expansion

$$\rho_{n+1} = \left[\mathbb{1} + \Delta t \mathcal{L} + \frac{1}{2!}(\Delta t)^2 \mathcal{L}^2 + \frac{1}{3!}(\Delta t)^3 \mathcal{L}^3 + \frac{1}{4!}(\Delta t)^4 \mathcal{L}^4 \right] \rho_n + O\{(\Delta t)^5\}. \quad (2.60)$$

2.3.2.2 Quantum trajectories (piecewise deterministic processes)

The basic idea underlying the quantum trajectories theory consists of rewriting the master equation as an ensemble average over the individual stochastic trajectories of an initial pure state of the system [161–163]. Specifically, an effective *deterministic* evolution is interrupted by stochastic jumps of the system, due to the interaction with the environment. This means that the master equation can be represented by a piecewise deterministic process (PDP) [155]. It is possible to achieve this result in several ways, which correspond to different stochastic *unravelings* of the master equation. The choice of the unraveling corresponds to a set of probabilistic decisions over time, which defines the evolution of the system (the “trajectory”) and is inevitably lost in the ensemble-average representation of the density matrix. The numerical advantage of the quantum trajectories method is great when dealing with large systems: For a N -dimensional Hilbert space, solving numerically the full master equation requires the storage of $O\{N^4\}$ elements of the Liouvillian. The PDP method involves only $O\{N^2\}$ elements instead. One must anyway realize a large number $M \gg 1$ of trajectories starting from a pure state to guarantee a good ensemble statistics, but typically $M \ll N^2$ is sufficient.

A possible formulation of the quantum trajectories method can be devised in terms of photon counting from a cavity using a detector. This corresponds to the “quantum jump” approach to damping, which I will consider here. An equivalent derivation of a quantum trajectory follows from the description of the conditional evolution of a system under a continuous measurement, conditioned on a stochastic record of measurements, and is generally referred to as the “diffusive limit” of the master equation unraveling [164, 165]. A common application of this limit is the homodyne or heterodyne detection of the field leaving the cavity.

The idea behind the quantum jump approach is to consider the following nonlinear equation for a state $|\psi(t)\rangle$ of the system:

$$|\dot{\psi}\rangle = -i \left(H - \frac{i}{2} \sum_{\alpha} \gamma_{\alpha} A_{\alpha}^{\dagger} A_{\alpha} \right) |\psi\rangle + \frac{1}{2} \left(\sum_{\alpha} \gamma_{\alpha} \langle \psi | A_{\alpha}^{\dagger} A_{\alpha} | \psi \rangle \right) |\psi\rangle. \quad (2.61)$$

Its solution is given by [164]

$$|\psi(t)\rangle = \frac{e^{-iH_{\text{eff}}t}}{\sqrt{\langle \psi(0) | e^{iH_{\text{eff}}^{\dagger}t} e^{-iH_{\text{eff}}t} | \psi(0) \rangle}} |\psi(0)\rangle, \quad (2.62)$$

where I have introduced the nonhermitian Hamiltonian:

$$H_{\text{eff}} = H - \frac{i}{2} \sum_{\alpha} \gamma_{\alpha} A_{\alpha}^{\dagger} A_{\alpha}. \quad (2.63)$$

Clearly, Eq. (2.62) gives a deterministic evolution. To reproduce the correct Lindblad dynamics, it is necessary to interrupt the deterministic dynamics with stochastic events (jumps). Defining the total probability of a jump to occur within the time interval δt ,

$$p_{\text{jump}} = \delta t \sum_{\alpha} \gamma_{\alpha} \langle \psi | A_{\alpha}^{\dagger} A_{\alpha} | \psi \rangle \quad (2.64)$$

one needs to decide randomly which jump has occurred by updating the state according to

$$|\tilde{\psi}(t + \delta t)\rangle = A_{\alpha} |\psi(t)\rangle, \quad (2.65)$$

to be normalized. The probability for the α -jump to occur is given by

$$p_{\alpha} = \frac{\gamma_{\alpha} \langle \psi(t) | A_{\alpha}^{\dagger} A_{\alpha} | \psi(t) \rangle}{p_{\text{jump}} / \delta t}. \quad (2.66)$$

If the jump has not occurred, the state is propagated according to Eq. (2.62). The numerical scheme is summarized in Fig. 2.2, for the simplified case of a single jump operator a . At time t , p_{jump} is computed. Then, a random number r is generated. If $p_{\text{jump}} < r$, a jump is assumed to have taken place. The jump operator a is applied to the state, and it is then normalized, giving $|\psi(t + \delta t)\rangle$. Conversely, if $p_{\text{jump}} \geq 1$, no jump has occurred and the nonunitary effective evolution with H_{eff} is assumed.

Formally, the procedure described above is described by a stochastic Schrödinger equation, given by [165]

$$|d\psi\rangle = \left(-iH_{\text{eff}} + \frac{1}{2} \sum_{\alpha} \gamma_{\alpha} \langle \psi | A_{\alpha}^{\dagger} A_{\alpha} | \psi \rangle \right) |\psi\rangle dt + \sum_{\alpha} \left(\frac{A_{\alpha} |\psi\rangle}{\sqrt{\langle \psi | A_{\alpha}^{\dagger} A_{\alpha} | \psi \rangle}} - |\psi\rangle \right) dN_{\alpha}. \quad (2.67)$$

The dN_{α} are Poisson increments, satisfying

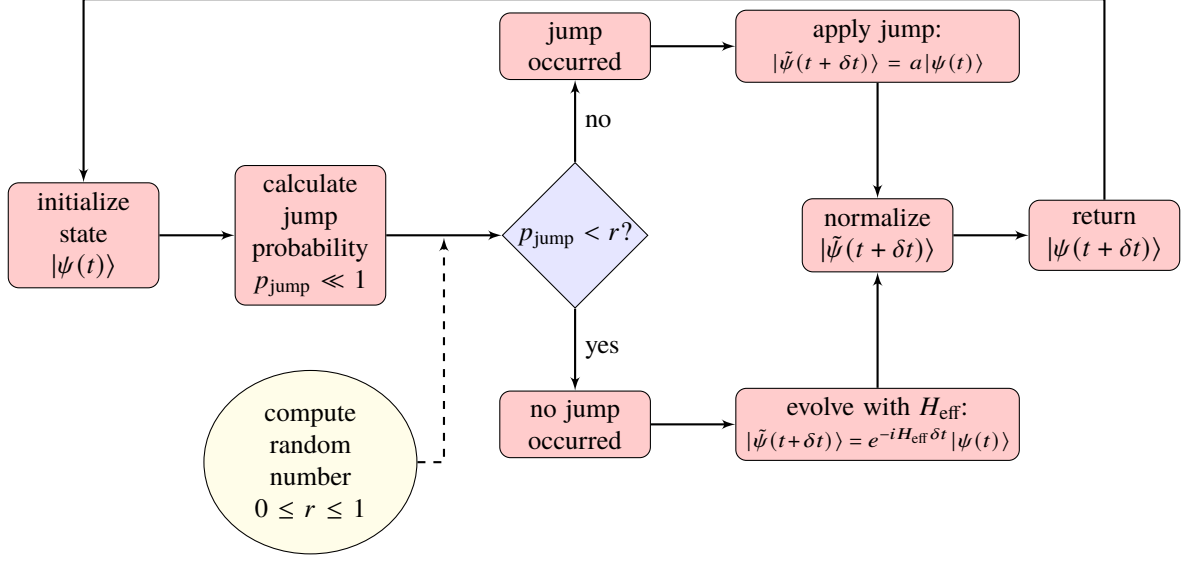


Figure 2.2: Numerical scheme for the propagation of one time step in the quantum trajectories (PDP) method.

$$dN_\alpha dN_\beta = \delta_{\alpha\beta} dN_\alpha, \quad E[dN_\alpha] = \delta t \gamma_\alpha \langle \psi | A_\alpha^\dagger A_\alpha | \psi \rangle, \quad (2.68)$$

where $E[\cdot]$ corresponds to the classical expectation value. It is possible to show that the ensemble average $E[|\psi\rangle\langle\psi|]$ evolved with Eq. (2.67) satisfies the Lindblad master equation (2.38) [155, 165].

2.3.2.3 Steady-state solution

Of particular interest for this work is a method to look for the stationary state of the system ρ_{st} , i.e., the state reached for $t \rightarrow \infty$. Instead of integrating numerically the master equation up to long times, one may focus on the steady equation

$$\dot{\rho} = \mathcal{L}\rho \stackrel{!}{=} 0. \quad (2.69)$$

In this way, we modify the problem into a linear algebra one, which consists in finding the null space (or kernel) of the Liouvillian operator \mathcal{L} , i.e., the right eigenvector associated to the zero eigenvalue of the matrix \mathcal{L} . Being a standard problem, many methods exist to solve it [166]. The direct method, consisting in simply computing the inverse \mathcal{L}^{-1} , cannot be used as \mathcal{L} is singular, and it would be a formidable numerical problem for a large system. An alternative is given by the Arnoldi iteration scheme to compute the zero-eigenvector of \mathcal{L} by finding an orthonormal basis for the Krylov subspace from some initial guess state ρ_0 . The Arnoldi scheme is the basis for the GMRES (generalized minimal residual) method, which is an efficient iterative procedure to compute ρ_{st} [167].

Note that these methods are valid to solve in general the linear system $Ax = b$, and can thus be used also to find the vector of steady populations which satisfies the stationary Pauli rate equations presented in Sec. 2.2.7. In this case, one needs to find the vector ρ_{st} satisfying

$$\sum_m w_{n \leftarrow m} \rho_{mm} - \sum_m w_{m \leftarrow n} \rho_{nn} = 0, \quad (2.70)$$

i.e., the kernel of the reduced Liouvillian \mathcal{W} with entries

$$W_{nm} = w_{n \leftarrow m} - \delta_{nm} \sum_p w_{p \leftarrow m}. \quad (2.71)$$

Chapter 3

Dynamical multistability in a quantum-dot laser

The results presented in this Chapter are published in Ref. 168.

3.1 Introduction

One of the most remarkable paradigms of light-matter interaction is the laser [6, 169, 170], or maser, when the emitted radiation wavelength falls in the microwave regime. The lasing mechanism is generally based on a population inversion established in a gaining medium, which interacts with the electromagnetic field inside a cavity. The full quantum theory of the laser has been proposed in the pioneering works of Scully and Lamb [171–173]. The gaining medium can be scaled down to a single emitter, realizing a single-atom laser [174]. Later on, single-atom lasing action has been first observed experimentally in the regime of strong atom-field coupling with a single caesium atom in a high-finesse optical cavity [175]. Unlike conventional lasers, one-atom amplifiers exhibit unique features such as thresholdless behaviour (due to strong coupling), self-quenching, and a sub-Poissonian photon statistics reflecting the quantum nature of both field and atoms [176]. Within the context of cavity QED, a related setup is the micromaser [2, 16, 177, 178], where a stream of excited atoms is injected into a cavity at a low rate, such that at most one atom at a time resides in the cavity. The micromaser can display a succession of sharp transitions in the cavity photon number and multistability, whereby two or more stable amplitudes of oscillation coexist.

The study of single-emitter lasers and micromasers has been later extended to hybrid condensed matter systems, where a number of theoretical models have been proposed and realized experimentally on a variety of platforms, such as superconducting qubits [179–181], quantum dots embedded in optical photonic crystals [182], devices based on Josephson junctions [183–186], and especially single or double quantum dots [138–141, 187–194]. Recent experiments on self-sustained oscillations in carbon nanotubes with ultra-high quality factors [142–144] are a key step towards the implementation of single-atom *phonon* lasers utilizing mechanical resonators [195, 196]. Furthermore, the engineerization of effective interactions between *spins* and oscillation (mechanical or electromagnetic) has attracted a lot of

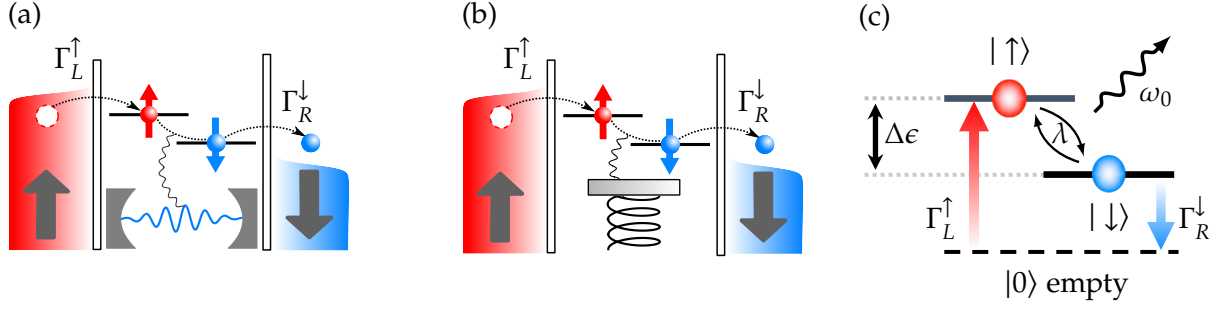


Figure 3.1: Spin-valve-based quantum dot laser. (a) A microwave photon cavity or (b) a nanomechanical resonator mode are coupled to the spin of an electron in a quantum dot, in contact with ferromagnetic leads carrying spin-polarized current. (c) The system can be mapped onto a three-level single-atom laser, where electrons are pumped into the up-spin level, interact coherently emitting photons into the cavity, and decay into the empty-dot state by tunneling into the right lead.

theoretical and experimental attention over the past few years [107, 117, 123–125, 127, 128, 197–200] (see Ch. 1).

In this Chapter, I present an implementation of a single-atom laser based on the interaction between the electron spin in a quantum dot and a resonant cavity [168]. The quantum dot is in a spin-valve configuration: It is tunnel coupled to ferromagnetic conductors having noncollinear magnetizations [201–203]. As a result, the electron transport is highly spin-dependent and influenced by the spin-flip processes due to the coupling with the resonator. Within this approach, a phonon laser based on the spin-valve mechanism has been proposed [204]. Here, I show that our setup represents not only a simple mapping of a widely-studied theoretical model—the one-atom laser—on a solid-state platform. By contrast, it allows access to a novel and rich regime of multistable laser dynamics. This phenomenon arises from the breakdown of the rotating-wave approximation (RWA), which is believed to hold when the effective coupling between light and matter g remains small, when compared to the typical energy separation in the uncoupled subsystems (namely, the energy splitting $\Delta\epsilon$ of the two-level system and the cavity frequency ω_0).

After introducing the system and the model, I provide a semiclassical analysis to explain the multistable behavior, which agrees beautifully with the numerical simulations performed within a full quantum treatment of the resonator. While the multistable regime of a mechanical oscillator or of a microwave resonator may be in principle detected through optical detection or quantum state tomography of a cavity, we show instead that it maps directly on the electron transport through the quantum dot: The current displays a telegraph-like noise, associated with current jumps between different state of stability of the resonator.

3.2 Quantum-dot laser in the spin-valve setup

The system I am considering is depicted in Fig. 3.1. It consists of a quantum dot in the single-electron regime, with two nondegenerate spin levels ($|\uparrow\rangle$, $|\downarrow\rangle$), of energy difference $\Delta\epsilon$. The dot is embedded between two ferromagnetic contacts, which carry a spin-polarized current of opposite polarization. The magnetization axis of the leads is chosen parallel to the quantization axis of the electronic spin in the dot. The spin interacts with a single mode of a local resonator of frequency ω_0 , which can be either a

microwave cavity or a nanomechanical resonator and is naturally damped through a thermal bath. The Hamiltonian of the total system is given by

$$H_{\text{tot}} = H + H_{\text{leads}} + H_{\text{tun}} + H_{\text{bath}} + H_{\text{osc-bath}}. \quad (3.1)$$

Here, H is the dot-resonator system Hamiltonian, H_{leads} describes the ferromagnetic contacts, H_{tun} provides the electron tunneling between dot and leads, H_{bath} describes a generic bosonic bath to which the resonator is damped through the coupling term $H_{\text{osc-bath}}$. The different contributions read:

$$H = \epsilon_0(n_{\uparrow} + n_{\downarrow}) + \frac{\Delta\epsilon}{2}(n_{\uparrow} - n_{\downarrow}) + Un_{\uparrow}n_{\downarrow} + \omega_0 b^{\dagger}b + g(b + b^{\dagger})(d_{\uparrow}^{\dagger}d_{\downarrow} + \text{H.c.}), \quad (3.2)$$

$$H_{\text{leads}} = \sum_{\nu=L,R} \sum_{k\sigma} (\epsilon_{\nu k\sigma} - \mu_{\nu}) c_{\nu k\sigma}^{\dagger} c_{\nu k\sigma}, \quad (3.3)$$

$$H_{\text{tun}} = \sum_{\nu=L,R} \sum_{k\sigma} V_{\nu\sigma} (c_{\nu k\sigma} d_{\sigma}^{\dagger} + \text{H.c.}), \quad (3.4)$$

$$H_{\text{osc-bath}} = bB + \text{H.c.} \quad (3.5)$$

Let us first describe in detail the system Hamiltonian H : I have labeled with ϵ_0 the average energy of the spin levels in the dot, with $\Delta\epsilon$ their energy separation, and with $U > 0$ the Coulomb repulsion strength for the doubly-occupied state. The cavity mode (of frequency ω_0) is coupled with strength g to the quantum dot through the spin-oscillator interaction term. d_{σ} is the fermionic operator annihilating an electron of spin σ on the dot ($\sigma = \{\uparrow, \downarrow\} = \{+, -\}$); n_{σ} is the corresponding number operator. The cavity mode is described by the bosonic annihilation operator b .

The ferromagnetic leads are described in H_{leads} by Fermi gas Hamiltonians, with $c_{\nu k\sigma}$ the annihilation operator for an excitation of momentum k and energy $\epsilon_{\nu k\sigma}$ on the lead ν kept at chemical potential μ_{ν} . $V_{\nu\sigma}$ is the electron tunneling amplitude. Finally, B describes a generic operator of the bosonic bath coupled linearly to the resonator. The three reservoirs are assumed to be at separate thermal equilibria at temperature T (but can be at different chemical potentials).

3.3 Quantum master equation

In this Section, I derive the Markovian master equation describing the dynamics of the system density matrix ρ , under the coherent evolution given by Eq. (3.2) and the dissipative mechanisms due to the electron tunneling and the resonator damping. The external environment is governed by the Hamiltonian $H_E = H_{\text{leads}} + H_{\text{bath}}$, and it interacts with the system through $H_{\text{int}} = H_{\text{tun}} + H_{\text{osc-bath}}$. Assuming that the weak-coupling and large reservoir limits, the Born-Markov approximation holds (see Ch. 2). The Wangsness-Bloch-Redfield master equation for the system (in the Schrödinger picture) reads [153, 205]:

$$\dot{\rho}(t) = -i[H, \rho(t)] - \int_0^{\infty} d\tau \text{Tr}_E \{ [H_{\text{int}}, [H_{\text{int}}(-\tau), \rho(t) \rho_{\text{leads}}(0) \rho_{\text{bath}}(0)]] \} \equiv \mathcal{L}\rho(t). \quad (3.6)$$

Here, $\rho_{\text{leads}}(0)$ and $\rho_{\text{bath}}(0)$ represent the states of the reservoirs at the initial time ($t = 0$); \mathcal{L} is the total Liouvillian superoperator. Its action on ρ can be decomposed into the sum of a coherent part ($\mathcal{L}_H \rho = -i[H, \rho]$) and a dissipative part $\mathcal{L}_{\text{leads}}\rho + \mathcal{L}_{\text{bath}}\rho$.

In order to simplify Eq. (3.6), I make three important assumptions:

- (i) A large bias voltage V is applied symmetrically to the leads, such that $\mu_L = eV/2$, $\mu_R = -eV/2$, with $V \gg \{k_B T; \omega_0; \Delta\epsilon\}$. The Fermi functions $f_\nu(x) = \{\exp[(x - \mu_\nu)/k_B T] + 1\}^{-1}$ are then $f_L \approx 1$ and $f_R \approx 0$, with no energy dependence. This means that electron transport is allowed from the left to the right lead, while it is completely suppressed in the opposite direction.
- (ii) The Coulomb repulsion strength U is the largest energy scale in the system, such that the doubly-occupied state in the quantum dot becomes energetically inaccessible, and it cannot be thermally populated. Thus, it can be projected out from the electronic Hilbert space. Formally, we have $U \gg eV \gg \{k_B T; \omega_0; \Delta\epsilon\}$. Consequently, the coherent dynamics given by Hamiltonian (3.2) only involves the two spin states ($|\uparrow\rangle, |\downarrow\rangle$). This allows us to map Eq. (3.2) into the Rabi Hamiltonian [4, 5]:

$$H = \frac{\Delta\epsilon}{2}\sigma_z + \omega_0 b^\dagger b + g(\sigma_+ + \sigma_-)(b + b^\dagger). \quad (3.7)$$

The Coulomb term in Eq. (3.2) has been removed, and we have mapped the dot operators to the Pauli algebra through $n_\uparrow - n_\downarrow \rightarrow \sigma_z$ and $d_\uparrow^\dagger d_\downarrow \rightarrow \sigma_+$, after projecting out the empty and the doubly-occupied states from the dot Hilbert space. Notice that, however, the empty state $|0\rangle$ must be taken into account in the open dynamics: In the single-electron regime, transport through the dot necessarily involves the third state $|0\rangle$.

- (iii) The spin-resonator coupling strength g is small compared to the typical bare energy scale of the two subsystems, i.e., $g \ll \{\Delta\epsilon; \omega_0\}$. This allows us to safely treat Eq. (3.6) in the local basis $|n, \sigma\rangle$ of the uncoupled system (n is the Fock number of the resonator), deriving a *local* master equation [206].

Under assumptions (i)-(iii), the time integrals in Eq. (3.6) can be performed and they lead to a quantum master equation in Lindblad form:

$$\dot{\rho} = -i[H, \rho] + \sum_{\sigma} [\Gamma_L^{\sigma} \mathcal{D}(F_{\sigma}^{\dagger})\rho + \Gamma_R^{\sigma} \mathcal{D}(F_{\sigma})\rho] + \kappa(1 + n_B)\mathcal{D}(b) + \kappa n_B \mathcal{D}(b^{\dagger}). \quad (3.8)$$

Within the wide-band approximation, whereby the spectral densities of the fermionic reservoirs are energy-independent, the electronic tunneling rates are given by $\Gamma_{\nu}^{\sigma} = 2\pi|V_{\nu\sigma}|^2\rho_{\nu\sigma}$, where $\rho_{\nu\sigma}$ is the spin- σ density of states at the Fermi level of lead ν . Since the leads are ferromagnetic, the spin dependence of the tunneling rates can be written in terms of the polarizations P_{ν} of the leads as $\Gamma_{\nu}^{\sigma} = \Gamma_{\nu}(1 + \sigma P_{\nu})/2$, with $0 \leq P_{\nu} \leq 1$. Although for standard ferromagnetic contacts (Co and PdNi alloys) P_{ν} does not exceed 0.5 [124, 128, 202], it can be equal to unity for half-metallic leads [207]. In the following, without losing generality in the results, I will assume a symmetric and opposite polarization of the leads, i.e., $P_L = -P_R = P$, allowing us to write the tunneling rates as

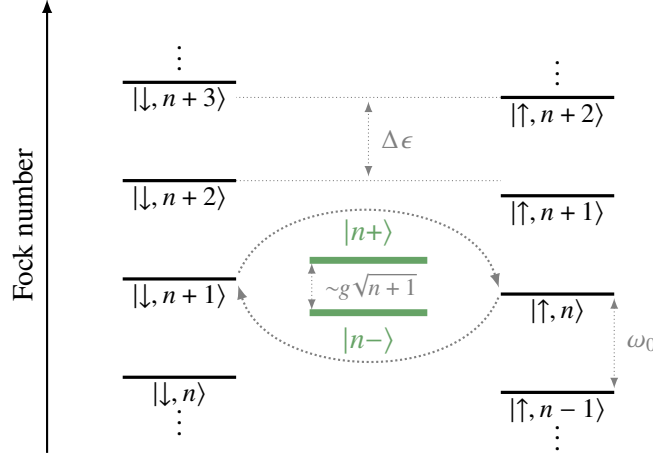


Figure 3.2: Energy ladder of the uncoupled dot-resonator system (black lines). When $\Delta\epsilon \approx \omega_0$, the RWA Hamiltonian (3.10) describes the hybridization of the pairs $\{| \uparrow, n \rangle, | \downarrow, n+1 \rangle\}$, giving rise to the Jaynes-Cummings doublet [green lines, Eq. (3.11)]. The energy separation of each doublet grows proportionally to $g\sqrt{n+1}$.

$$\begin{aligned}\Gamma_L^\uparrow &= \Gamma_L \left(\frac{1+P}{2} \right), & \Gamma_L^\downarrow &= \Gamma_L \left(\frac{1-P}{2} \right), \\ \Gamma_R^\uparrow &= \Gamma_R \left(\frac{1-P}{2} \right), & \Gamma_R^\downarrow &= \Gamma_R \left(\frac{1+P}{2} \right).\end{aligned}\tag{3.9}$$

In the electronic dissipators, we have replaced the fermionic operator d_σ with $F_\sigma = (1 - n_{-\sigma})d_\sigma$, such that the population and the coherences involving the doubly-occupied state are forced to vanish, as required by the large Coulomb repulsion limit.

For the cavity, $\kappa = \omega_0/Q$ is the decay rate (Q is the quality factor), and $n_B = [\exp(\omega_0/k_B T) - 1]^{-1}$ is the average number of excitations in the thermal bath at the resonator frequency.

The steady state ρ_{st} of Eq. (3.8), obtained by solving $\dot{\rho} = 0$, is the central object that I will employ to calculate the relevant stationary expectation values for the system, together with the cavity Fock distribution. The numerical steady solution of Eq. (3.8) has been found using QUTIP [208].

3.4 Single-atom laser within the rotating-wave approximation (RWA)

3.4.1 RWA Hamiltonian and Jaynes-Cummings model

The theoretical treatment of the single-atom laser usually relies upon the so-called rotating-wave approximation (RWA). It consists in replacing the Rabi model Hamiltonian with the Jaynes-Cummings (JC) one [8]:

$$H_{\text{RWA}} = \frac{\Delta\epsilon}{2}\sigma_z + \omega_0 b^\dagger b + g(\sigma_+ b + \sigma_- b^\dagger).\tag{3.10}$$

Equation (3.10) can be derived from the Rabi Hamiltonian (3.7) by moving to interaction picture and assuming a small detuning $\delta \ll \omega_0 + \Delta\epsilon$, with $\delta = |\omega_0 - \Delta\epsilon|$. Further, one must also ensure that $g\sqrt{n} \ll \{\omega_0; \Delta\epsilon\}$, where n is the cavity Fock number. In Fig. 3.2, I sketch the effective interaction

described by the JC model, close to resonance, i.e., $\delta \approx 0$. The interaction (3.10) mixes *only* the states $|\uparrow, n\rangle$ and $|\downarrow, n+1\rangle$. Diagonalizing the interaction in the subspace spanned by these two states yields the JC doublet

$$\begin{aligned} |n+\rangle &= \cos\left(\frac{\theta}{2}\right) |\uparrow, n\rangle + \sin\left(\frac{\theta}{2}\right) |\downarrow, n+1\rangle, \\ |n-\rangle &= -\sin\left(\frac{\theta}{2}\right) |\uparrow, n\rangle + \cos\left(\frac{\theta}{2}\right) |\downarrow, n+1\rangle, \end{aligned} \quad (3.11)$$

with eigenenergies $E_{n\pm} = \omega_0 \left(n + \frac{1}{2}\right) \pm \frac{1}{2} \sqrt{4g^2(n+1) + \delta^2}$ and mixing angle $\theta = \arctan\left(\frac{2g\sqrt{n+1}}{\delta}\right)$. Notice that the doublet splitting is proportional to $g\sqrt{n+1}$, i.e., the eigenvalue ladder of the JC Hamiltonian is anharmonic. If $g\sqrt{n+1}$ becomes comparable with the bare level separation of the uncoupled system, Eq. (3.10) is no longer valid, as doublets with different quantum number n become closer in energy, and their interaction (which is not captured by the RWA Hamiltonian) cannot be neglected anymore. For atom-field cavity systems, $g/\omega_0 \sim 10^{-7} - 10^{-6}$ [1], hence Eq. (3.10) remains valid also for photon numbers $n \gg 1$ characteristic of laser emission. However, as the technological development in solid-state devices pushes the ratio g/ω_0 order of magnitudes higher, a more careful consideration on the validity of the RWA is necessary when designing systems with large photon number.

3.4.2 Density matrix theory

Using Eq. (3.10) in Eq. (3.8), it is possible to obtain the approximate analytical expression for the steady-state Fock distribution of the cavity, p_n (details of the calculations for a simplified case are provided in Appendix B, following the works of Scully and Lamb [6, 172]). In particular, when close to the resonant condition $\Delta\epsilon = \omega_0$, the p_n is obtained through the following recursive equation:

$$\left[\frac{n\kappa \left(\frac{g}{g_{\text{thr}}}\right)^2}{1 + \frac{n}{A_s^2} \left(\frac{g}{g_{\text{thr}}}\right)^2} + \kappa n_B \right] p_{n-1} = \kappa(1 + n_B) p_n, \quad (3.12)$$

with the quantities

$$A_s^2 = \frac{\Gamma_L \Gamma_R P}{(2\Gamma_L + \Gamma_R)\kappa}, \quad g_{\text{thr}} = \sqrt{\frac{\Gamma_R \kappa}{4} \left[\frac{2\Gamma_L(1 + P^2) + \Gamma_R(1 - P^2)}{4\Gamma_L P} \right]}. \quad (3.13)$$

I will refer to A_s^2 as the *saturation number* and to g_{thr} as the *lasing threshold coupling*. The solution of Eq. (3.12) reads

$$p_n = p_0 \frac{\mathcal{N}_n}{\mathcal{D}_n} \left(\frac{n_B}{n_B + 1} \right)^n. \quad (3.14)$$

Here, I have introduced the Pochhammer symbol (or rising factorial) $a_n = a(a+1)(a+2) \cdots (a+n-1)$ and defined the quantities

$$\mathcal{N} = 1 + \frac{A_s^2}{n_B} + A_s^2 \frac{g_{\text{thr}}}{g}, \quad \mathcal{D} = 1 + A_s^2 \frac{g_{\text{thr}}}{g}. \quad (3.15)$$

The prefactor p_0 is the zero-Fock occupation number and is determined from the normalization condition $\sum_{n=0}^{\infty} p_n = 1$, leaving us with

$$p_0 = \frac{1}{{}_2F_1\left(1, \mathcal{N}; \mathcal{D}; \frac{n_B}{n_B+1}\right)}, \quad (3.16)$$

with the hypergeometric function ${}_2F_1(a, b; c; z)$. At zero temperature, one finds instead $p_0 = [{}_1F_1(1; A_s^2 g_{\text{thr}}^2 / g^2; n_B / (n_B + 1))]^{-1}$, with the confluent hypergeometric function ${}_1F_1(a; b; z)$. A more interesting quantity is represented by the average photon number, $\bar{n} = \sum_{n=0}^{\infty} n p_n$, which is found to be

$$\bar{n} = A_s^2 \left[1 - \left(\frac{g_{\text{thr}}}{g} \right)^2 \right] + n_B + n_B(n_B + 1) \left(\frac{g_{\text{thr}}}{g} \right)^2 p_0. \quad (3.17)$$

The analytical expression Eq. (3.14) allows also to calculate also the second moment of the distribution, $\overline{n^2}$, and from it the Fano factor [6, 209], defined as

$$\mathcal{F} = \frac{\overline{n^2} - \bar{n}^2}{\bar{n}}. \quad (3.18)$$

The Fano factor yields a measure of the dispersion of a probability distribution, compared to the variance of a Poissonian distribution (where it is equal to the mean). The Poissonian distribution has a Fano factor equal to 1, and is characteristic of a classical laser. A sub-Poissonian distribution ($\mathcal{F} < 1$) can be instead signature of quantum behavior in the resonator, as the distribution tends to be more narrow and different from a classical field. The resulting expression for the Fano factor is

$$\mathcal{F} = 1 + n_B + \frac{1}{\left(\frac{g}{g_{\text{thr}}} \right)^2 + \frac{n_B + A_s^2}{n_B + 1}} - \alpha p_0, \quad (3.19)$$

where I have gathered in α an unimportant factor multiplying p_0 . At zero temperature and far above threshold ($g \gg g_{\text{thr}}$), the above expression becomes

$$\mathcal{F} = 1 + \frac{1}{\left(\frac{g}{g_{\text{thr}}} \right)^2 + A_s^2 - 1}. \quad (3.20)$$

The Fano factor is peaked around the threshold coupling, where quantum fluctuations increase, witnessing a dramatic change in the Fock distribution, analogously to a phase transition. Above threshold, the analytical expression predicts that \mathcal{F} tends to the Poissonian value, $\mathcal{F} = 1$.

In Fig. 3.3(a)-(b), I have collected the analytical results for both \bar{n} and \mathcal{F} , together with their comparison to a numerical calculation using the full master equation and the RWA Hamiltonian and to the result

from a semiclassical analysis (see below).

3.4.3 Semiclassical theory

Equation (3.8) allows us to derive the equation of motion for the expectation value of a system operator O , defined as $\langle O \rangle = \text{Tr}(O\rho)$:

$$\begin{aligned} \langle \dot{O} \rangle = & -i\langle [O, H] \rangle + \sum_{\sigma} \left[\Gamma_L^{\sigma} \left(\langle F_{\sigma} O F_{\sigma}^{\dagger} \rangle - \frac{1}{2} \langle \{O, F_{\sigma} F_{\sigma}^{\dagger}\} \rangle \right) + \Gamma_R^{\sigma} \left(\langle F_{\sigma}^{\dagger} O F_{\sigma} \rangle - \frac{1}{2} \langle \{O, F_{\sigma}^{\dagger} F_{\sigma}\} \rangle \right) \right] + \\ & + \kappa(1 + n_B) \left(\langle b^{\dagger} O b \rangle - \frac{1}{2} \langle \{O, b^{\dagger} b\} \rangle \right) + \kappa n_B \left(\langle b O b^{\dagger} \rangle - \frac{1}{2} \langle \{O, b b^{\dagger}\} \rangle \right). \end{aligned} \quad (3.21)$$

Using the RWA Hamiltonian in Eq. (3.21), one is able to derive a nonlinear set of dynamical equations which govern the system. For simplicity, let us set $P = 1$ and $n_B = 0$. The equations read:

$$\langle \dot{n}_{\uparrow} \rangle = -\Gamma_L \langle n_{\uparrow} - n_{\downarrow} \rangle - ig \langle b \sigma_{+} - b^{\dagger} \sigma_{-} \rangle + \Gamma_L, \quad (3.22)$$

$$\langle \dot{n}_{\downarrow} \rangle = \Gamma_R \langle n_{\downarrow} \rangle + ig \langle b \sigma_{+} - b^{\dagger} \sigma_{-} \rangle, \quad (3.23)$$

$$\langle \dot{\sigma}_{-} \rangle = \left(-i\Delta\epsilon - \frac{\Gamma_R}{2} \right) \langle \sigma_{-} \rangle + ig \langle (b + b^{\dagger})(n_{\uparrow} - n_{\downarrow}) \rangle, \quad \text{and c.c.}, \quad (3.24)$$

$$\langle \dot{b} \rangle = \left(-i\omega_0 - \frac{\kappa}{2} \right) \langle b \rangle - ig \langle \sigma_{-} \rangle, \quad \text{and c.c.} \quad (3.25)$$

Equations (3.22)-(3.25) contain expectation values involving both spin and cavity operators: Writing equations of motions for these terms will involve higher order operators and lead to an infinite hierarchy of equations, which cannot be solved. To close the set of equations, the semiclassical approximation is needed. It consists in replacing the bosonic operator b by the complex number $\alpha = A e^{i\phi}$. A and ϕ correspond to the semiclassical amplitude and phase of the resonator, respectively. The semiclassical approximation basically amounts to neglecting the quantum fluctuations in the resonator. Let us now switch to a rotating frame with the replacements $\langle \sigma_{-} \rangle \rightarrow \langle \sigma_{-} \rangle e^{-i\Delta\epsilon t}$ and $\alpha \rightarrow \alpha e^{-i\omega_0 t}$. Further, I set the spin quantities $S_x = \langle \sigma_{+} + \sigma_{-} \rangle$, $S_y = -i\langle \sigma_{+} - \sigma_{-} \rangle$, $S_z = \langle n_{\uparrow} - n_{\downarrow} \rangle$, and the total dot occupation $p_1 = \langle n_{\uparrow} + n_{\downarrow} \rangle$. Finally, we consider the special case where $\Gamma_L = \Gamma_R/2 = \Gamma$ in Eq. (3.9): With this condition, the equation for p_1 decouples from the rest of the system and can thus be disregarded. However, it is worth remarking that this condition does not alter the physical results, but merely yields a simplification in the analytical calculations. At resonance ($\Delta\epsilon = \omega_0$) one obtains the set of equations

$$\dot{S}_x = -\Gamma S_x - 2gA \sin \phi S_z, \quad (3.26)$$

$$\dot{S}_y = -\Gamma S_y - 2gA \cos \phi S_z, \quad (3.27)$$

$$\dot{S}_z = \Gamma - \Gamma S_z + 2gA (\sin \phi S_x + \cos \phi S_y), \quad (3.28)$$

$$\dot{A} = -\frac{\kappa}{2}A + \frac{g}{2}(-\sin \phi S_x + \cos \phi S_y), \quad (3.29)$$

$$\dot{\phi} = -\frac{g}{2A}(\cos \phi S_x - \sin \phi S_y). \quad (3.30)$$

The equations for A and ϕ have been obtained by transforming the corresponding equations for α and α^* , using $\alpha = Ae^{i\phi}$. The system (3.26)-(3.26) is a nonlinear system describing lasing oscillations in the resonator, under the influence of the spin dynamics (driven by the single-electron tunneling at rate Γ). It is easy to study the stability of the resonator by setting the time derivatives to zero and looking for the stationary solution. The solution is independent on ϕ , which can be set to zero. For finite polarization $P < 1$, the dynamical equation for the resonator amplitude is

$$\dot{A} = -\frac{A}{2} \left[\kappa - \frac{\frac{2g^2P}{\Gamma}}{1 + \left(\frac{2gA}{\Gamma}\right)^2} \right] = -\frac{A}{2} [\kappa + \gamma_{\text{RWA}}(A)]. \quad (3.31)$$

In the latter equality, we have defined an effective, negative nonlinear damping $\gamma_{\text{RWA}}(A)$: It encompasses the driving effect of the electron dynamics, opposing the natural damping of the resonator at decay rate κ . By setting $\dot{A} = 0$, we obtain a nonlinear algebraic equation with two steady solutions for the occupation number $\bar{n} = A^2$, i.e.:

$$\bar{n} = 0 \quad \text{and} \quad \bar{n} = A_s^2 \left[1 - \left(\frac{g_{\text{thr}}}{g} \right)^2 \right]. \quad (3.32)$$

The saturation number and threshold coupling read

$$A_s^2 = \frac{\Gamma P}{2\kappa}, \quad g_{\text{thr}} = \sqrt{\frac{\Gamma \kappa}{2P}}, \quad (3.33)$$

respectively. Notice that they are in full agreement with Eq. (3.13), obtained with the full quantum approach. The stability analysis of Eq. (3.31) reveals a bifurcation point at $g = g_{\text{thr}}$: for $g \leq g_{\text{thr}}$, the only (stable) solution is $\bar{n} = 0$, corresponding to absence of lasing. For $g > g_{\text{thr}}$, $\bar{n} = 0$ is an unstable solution, while the other solution with large \bar{n} is the stable one. For a large coupling, $g \gg g_{\text{thr}}$, the nonlinear damping γ_{RWA} essentially loses its dependence on g . This causes the average occupation number to saturate to the value A_s^2 . Notice that the A -dependence of γ_{RWA} is crucial to obtain a finite steady value for \bar{n} . For completeness, I report here the more general expression of γ_{RWA} for arbitrary tunneling rates and $P = 1$ (obtained by including the equation for p_1 in the stationary solution of the system), which is given by

$$\gamma_{\text{RWA}}(A) = -\frac{g^2 \Gamma_{\text{eff}}}{g^2 A^2 + \Gamma_{\text{eff}} \Gamma_R / 4}, \quad (3.34)$$

where $\Gamma_{\text{eff}} = \Gamma_L \Gamma_R / (2\Gamma_L + \Gamma_R)$. Accordingly, the expressions for saturation number and threshold coupling become

$$g_{\text{thr}}^2 = \frac{\Gamma_R \kappa}{4}, \quad A_s = \sqrt{\frac{\Gamma_{\text{eff}}}{\kappa}} \quad (3.35)$$

The lasing threshold for fully polarized leads only depends on the right-tunneling rate Γ_R , as a consequence of the large Coulomb repulsion in the dot: Since only one electron can reside in the system at a given instant, a photon-emission event can only take place if the electron has tunneled out into the right contact. A large value of Γ_R pushes the threshold for lasing to appear to higher values of g .

In Fig. 3.3 I summarize the analytical results obtained with the semiclassical approximation and with the density matrix approach of Sec. 3.4.2, together with the numerical results. The analytical expression for \bar{n} agrees well with the numerics. However, the Fano factor is slightly overestimated by the density matrix approach. Indeed, the numerics predicts a sub-Poissonian Fock distribution for the resonator, with \mathcal{F} well below one. This can be observed more closely by inspecting the p_n distributions in Fig. 3.3(c)-(e) for below threshold, slightly above threshold, and far above threshold couplings g , respectively. The sub-Poissonian statistics is a typical signature of the single-atom laser [175, 176, 179]. In the Scully-Lamb approach, an ensemble average over many atoms is considered, which results in a decrease of total quantum fluctuations between atoms and resonator [172]. By contrast, as the size of the gaining medium is shrunk down to the limit of one atom, quantum fluctuations become important and are reflected in the emitted radiation: The photon stream tends to be “anti-bunched”, i.e., a delay exists between emission of two consecutive photons. The Fano factor below one also tells us that the number of photons emitted within a time is less random than the classical laser.

By looking at the average number of photons in Fig. 3.3(a), it is apparent that the value of $g\sqrt{\bar{n}}$ becomes of the same order of magnitude as ω_0 when above threshold: Despite a relatively low bare coupling strength $g \approx 0.05\omega_0$, one has $g\sqrt{\bar{n}} \approx 0.3\omega_0$ at saturation, which calls into question the validity of the RWA approach (see Sec. 3.4.1). Notice also that this is obtained with a resonator of modest quality factor $Q = 10^3$, proving a remarkable efficiency of the pumping mechanism provided by the spin-valve setup.

3.5 Beyond the rotating-wave approximation: Multistability

In the previous Section, I have analyzed the lasing behavior of the quantum-dot laser assuming the validity of the RWA Hamiltonian (3.10). However, the *a posteriori* analysis of the results reveals a peculiarity of our system with respect to similar (atomic and solid-state) implementations of the single-atom laser: The spin-dependent transport yields a very large photon emission efficiency (for the case of full polarization and negligible spin relaxation processes, each electron passing through the dot emits one photon), such that the quantity $g\sqrt{\bar{n}}$ becomes comparable to the bare resonator frequency ω_0 , even for relatively low values of the ratio g/ω_0 . Consequently, without the technologically challenging need

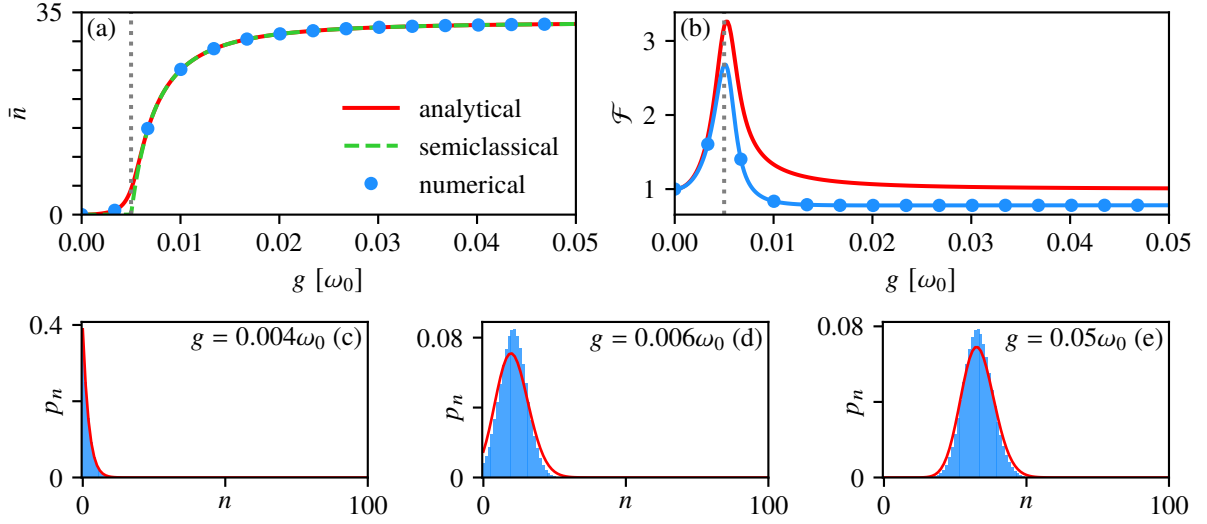


Figure 3.3: Single-atom laser within the RWA. (a) Average phonon occupation and (b) Fano factor for the Fock distribution, on resonance ($\Delta\epsilon = \omega_0$), as a function of the spin-resonator coupling g . The solid red line is computed from the analytical expression for p_n , Eq. (3.17), the filled blue circles represent the numerical calculation, and the green dashed line is the semiclassical result [Eq. (3.32)]. The vertical dotted grey lines correspond to the threshold coupling, $g_{\text{thr}} = 0.005\omega_0$. (c)-(e) Probability distributions for the oscillator Fock number at three different values of g , calculated numerically (bars) and analytically (solid red curves). Parameters: $\Gamma = 0.1\omega_0$, $Q = 10^3$, $T = 0$, $P = 1$.

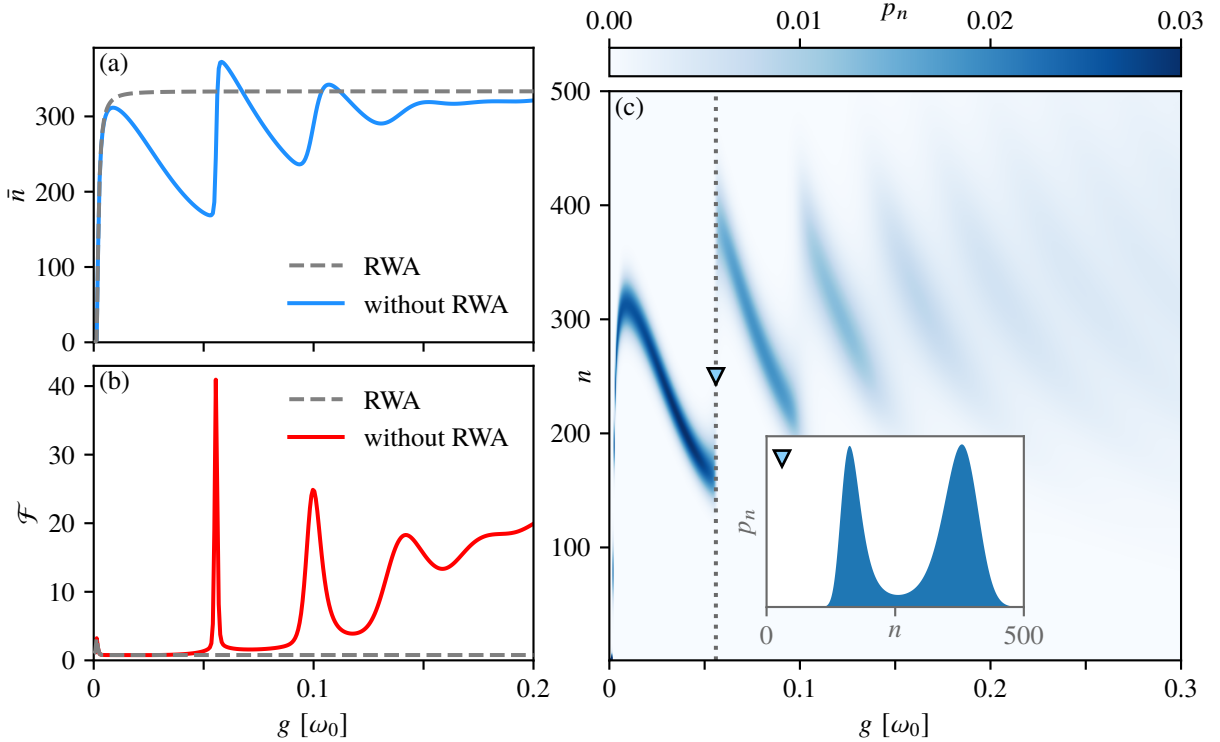


Figure 3.4: Single-atom laser beyond RWA. (a) Average Fock number and (b) Fano factor for the resonator, numerically calculated with the JC Hamiltonian (dashed lines) and with the Rabi Hamiltonian (solid lines) as a function of the spin-resonator coupling strength and on resonance ($\Delta\epsilon = \omega_0$). (c) Full Fock distributions as a function of g , showing regions of bi- and multistability. The inset shows the p_n at $g/\omega_0 \approx 0.056$ (dotted line), where bistability is more evident. Parameters: $\Gamma_L = \Gamma_R = 0.1\omega_0$, $Q = 10^4$, $T = 0$, $P = 1$.

to enter the *ultrastrong-coupling* regime (characterized by $g/\omega_0 \sim 1$, see Ch. 1), the system is expected to show a clear and unique deviation from the RWA physics.

A clear proof of this hypothesis is offered by simply comparing the computation of \bar{n} and \mathcal{F} obtained with the JC Hamiltonian and the full Hamiltonian, see Fig. 3.4 (on resonance). While the RWA predicts that the average number saturates to A_s^2 with increasing g , without any other changes developing, the full calculation shows a drop in \bar{n} even before reaching saturation, followed by a series of jumps. These jumps are associated to subsequent peaks in the Fano factor. By inspecting the Fock distribution obtained numerically close to the first jump in \bar{n} , one can see that it shows two peaks, suggesting a bistable behavior of the resonator, see inset of Fig. 3.4(c).

To understand the origin of this behavior, we resort below to a semiclassical approach similar to the one developed in the previous Section, in order to obtain a more accurate expression for the effective nonlinear damping, $\gamma_{\text{eff}}(A)$, to which the resonator is subject: The observation of an oscillatory behavior of \bar{n} must be linked to a nonmonotonic dependence of γ_{eff} on the semiclassical amplitude A , which, however, has to agree with the RWA expression Eq. (3.34) in the appropriate limit.

3.5.1 Semiclassical equations beyond RWA

The semiclassical approach utilized in Sec. 3.4.3 can be extended beyond the RWA by using the full Rabi Hamiltonian (3.7). First, Eqs. (3.22)-(3.25) are replaced by

$$\langle \dot{n}_\uparrow \rangle = -\Gamma_L \langle n_\uparrow \rangle - \Gamma_L \langle n_\downarrow \rangle - ig \langle (b + b^\dagger)(\sigma_+ - \sigma_-) \rangle + \Gamma_L, \quad (3.36)$$

$$\langle \dot{n}_\downarrow \rangle = -\Gamma_R \langle n_\downarrow \rangle + ig \langle (b + b^\dagger)(\sigma_+ - \sigma_-) \rangle, \quad (3.37)$$

$$\langle \dot{\sigma}_- \rangle = \left(-i\Delta\epsilon - \frac{\Gamma_R}{2} \right) \langle \sigma_- \rangle + ig \langle (b + b^\dagger)\sigma_z \rangle, \quad \text{and c.c.}, \quad (3.38)$$

$$\langle \dot{b} \rangle = \left(-i\omega_0 - \frac{\kappa}{2} \right) \langle b \rangle - ig \langle \sigma_+ + \sigma_- \rangle, \quad \text{and c.c.} \quad (3.39)$$

After the semiclassical approximation, setting again $\Gamma_L = \Gamma_R/2 = \Gamma$, $P = 1$ and $\Delta\epsilon = \omega_0$, and moving to the rotating frame as above, the system can be written as

$$\dot{S}_x = -\Gamma S_x - 2gA [\sin(2\omega_0 t - \phi) + \sin \phi] S_z, \quad (3.40)$$

$$\dot{S}_y = -\Gamma S_y - 2gA [\cos(2\omega_0 t - \phi) + \cos \phi] S_z, \quad (3.41)$$

$$\dot{S}_z = -\Gamma S_z + 2gA \{ [\sin(2\omega_0 t - \phi) + \sin \phi] S_x + [\cos(2\omega_0 t - \phi) + \cos \phi] S_y \} + \Gamma, \quad (3.42)$$

$$\dot{A} = -\frac{\kappa}{2} A + \frac{g}{2} \{ [\sin(2\omega_0 t - \phi) - \sin \phi] S_x + [\cos(2\omega_0 t - \phi) - \cos \phi] S_y \}, \quad (3.43)$$

$$\dot{\phi} = -\frac{g}{2A} \{ [\cos(2\omega_0 t - \phi) + \cos \phi] S_x - [\sin(2\omega_0 t - \phi) + \sin \phi] S_y \}. \quad (3.44)$$

Contrary to the RWA case, this nonlinear set of equations does not have a stationary solution in the rotating frame: The resonator will approach a limit-cycle oscillating solution. A more thorough analysis is then necessary to gain further quantitative information on the long-time limit behavior of the resonator

dynamics. The basic idea consists in studying Eqs. (3.40)-(3.44) in Fourier space, deriving an effective expression for the nonlinear damping of the resonator, γ_{eff} . To achieve this, it is crucial to exploit the fact that the dynamics of the resonator amplitude A is *slow* compared to the electronic driving and to the oscillations themselves, a condition satisfied when $\kappa \ll \{\Gamma; g; \omega_0\}$. I also assume that, eventually, the phase of the oscillator in the rotating frame is almost constant. As in the RWA case, the final result will be independent on ϕ and it can be set to 0. This can be checked empirically by solving numerically the time-dependent equations (3.40)-(3.44) and looking at the long-time behavior of $A(t)$. It is then possible to average the charge dynamics [determined by Eqs. (3.40)-(3.42)] over a resonator period $\mathcal{T} = 2\pi/\omega_0$, during which A can be considered constant. In this way, one can calculate the coarse-grained effect of the charge dynamics on the resonator amplitude. Averaging Eq. (3.43) over \mathcal{T} , we obtain

$$\dot{\bar{A}} = -\frac{\kappa}{2}\bar{A} + \frac{g}{2\mathcal{T}} \int_0^{\mathcal{T}} dt' \{ \sin(2\omega_0 t') S_x(t', \bar{A}) + [\cos(2\omega_0 t') - 1] S_y(t', \bar{A}) \}, \quad (3.45)$$

where $\bar{A} = 1/\mathcal{T} \int_0^{\mathcal{T}} dt' A(t')$. The cosine term in the integration acts as a Fourier filter, eliminating all Fourier components of S_x and S_y except for the ones oscillating at $\pm 2\omega_0 t$. The Fourier transforms of the spin quantities are defined as

$$\begin{aligned} S_k(t) &= \sum_{n=-\infty}^{+\infty} e^{-2i\omega_0 n t} S_k^{(n)}, \\ S_k^{(n)} &= \frac{1}{\mathcal{T}} \int_0^{\mathcal{T}} dt S_k(t) e^{2i\omega_0 n t}, \end{aligned} \quad (3.46)$$

with $k = x, y, z$. Because $S_k(t)$ is real, then $S_k^{(-n)} = S_k^{(n)*}$, and Eq. (3.45) becomes

$$\dot{\bar{A}} = -\frac{\kappa}{2}\bar{A} + \frac{g}{2} \{ -S_y^{(0)} + \text{Re}[S_y^{(1)}(\bar{A}) - \text{Im}[S_x^{(1)}(\bar{A})]] \} = -\frac{\bar{A}}{2} [\kappa + \gamma_{\text{eff}}(\bar{A})]. \quad (3.47)$$

The nonlinear damping is given by

$$\gamma_{\text{eff}}(\bar{A}) = -\frac{g}{\bar{A}} \left\{ \text{Re}[S_y^{(1)}(\bar{A})] - \text{Im}[S_x^{(1)}] - S_y^{(0)} \right\}. \quad (3.48)$$

Equation (3.48) can be recast to be dependent only on $S_z^{(0)}$ and $S_z^{(1)}$. First, we write the equations for the spin variables assuming constant A as the vector equation

$$\dot{\vec{S}}(t) = \Gamma \hat{u}_z - \Gamma \vec{S}(t) + \vec{S}(t) \times \vec{B}(t), \quad (3.49)$$

with \hat{u}_z the unit vector in z -direction and

$$\vec{B}(t) = \begin{pmatrix} B_x(t) \\ B_y(t) \end{pmatrix} = 2gA \begin{pmatrix} -1 - \cos(2\omega_0 t) \\ \sin(2\omega_0 t) \end{pmatrix}. \quad (3.50)$$

Equation (3.49) describes the motion of a spin under a varying effective magnetic field $\vec{B}(t)$. The behavior of its solutions is similar to that seen in previous studies on cQED and optomechanical systems [183,

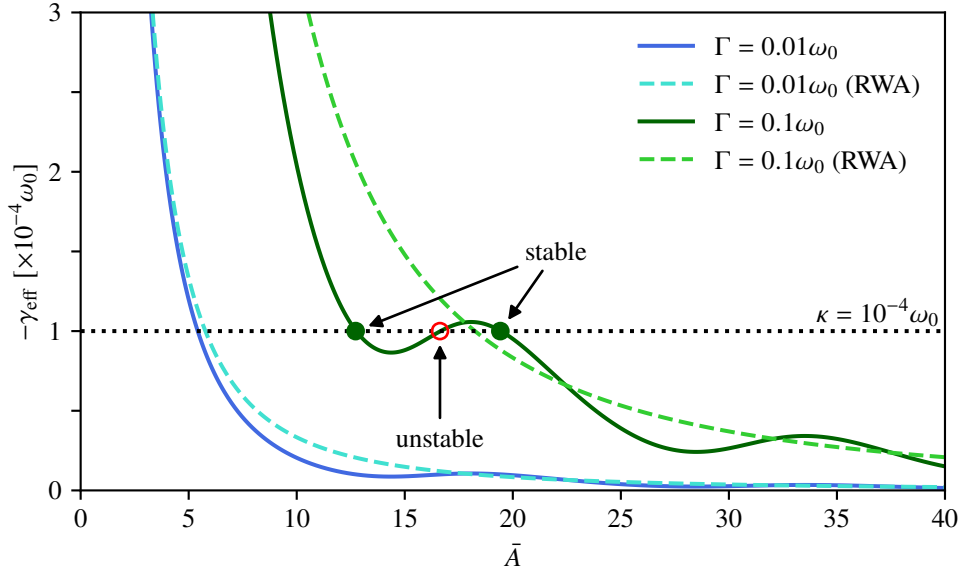


Figure 3.5: Effective negative nonlinear damping, γ_{eff} , acting on the resonator as a function of the time-averaged amplitude \bar{A} , on resonance ($\Delta\epsilon = \omega_0$), $g = 0.056\omega_0$ and $P = 1$, for two different values of $\Gamma_L = \Gamma_R/2 = \Gamma$ (solid lines). The dashed curves indicate the corresponding behavior of γ_{RWA} . The intersections with the horizontal dotted line at $\kappa = 10^{-4}\omega_0$ indicate limit cycles, which can be stable (filled green circles) or unstable (red open circle).

184, 210], although in this case a closed approximate analytical solution cannot be found. However, we can look at Eq. (3.49) in Fourier space using expansion (3.46), which yields a recursion relation for the Fourier coefficient $S_z^{(n)}$ in terms of $S_z^{(n\pm 1)}$. It reads:

$$\left[\chi_n^{-1} + \left(\frac{2gA}{\Gamma} \right)^2 \left(\chi_n + \frac{\chi_{n-1} + \chi_{n+1}}{2} \right) \right] S_z^{(n)} = \delta_{n,0} - \left(\frac{2gA}{\Gamma} \right)^2 \left(\frac{\chi_n + \chi_{n+1}}{2} S_z^{(n+1)} + \frac{\chi_{n-1} + \chi_n}{2} S_z^{(n-1)} \right). \quad (3.51)$$

We have introduced the generalized dimensionless susceptibility $\chi_n = \Gamma/(\Gamma + 2in\omega_0)$. Equation (3.51) is a matrix equation with an infinite band-diagonal matrix, having only three nonzero diagonals, and a constant vector. It can be solved numerically by truncating the resulting matrix, since the Fourier coefficients decay rapidly for increasing n . In practice, using $n \approx 15$ is sufficient to ensure convergence for the cases considered here. After solving numerically Eq. (3.51), one can find $S_x^{(n)}$ and $S_y^{(n)}$ in terms of $S_z^{(n)}$, and plug the solution into Eq. (3.48), obtaining

$$\gamma_{\text{eff}}(\bar{A}) = -\frac{2\lambda^2}{\Gamma} \left[\frac{4\omega_0^2}{\Gamma^2 + 4\omega_0^2} S_z^{(0)} - \text{Im} \left(\frac{2\omega_0}{\Gamma + 2i\omega_0} S_z^{(1)} \right) \right]. \quad (3.52)$$

The treatment can be readily generalized for $\Delta\epsilon \neq \omega_0$. In this case, the Fourier coefficients of S_z will satisfy

$$S_z^{(n)} = \frac{\delta_{n,0} - \left(\frac{2gA}{\Gamma}\right)^2 \left(\frac{\chi_n^+ \chi_n^-}{2} S_z^{(n+1)} + \frac{\chi_{n-1}^+ \chi_{n-1}^-}{2} S_z^{(n-1)} \right)}{\frac{(\chi_{n-1}^-)^{-1} + (\chi_n^+)^{-1}}{2} + \left(\frac{2gA}{\Gamma}\right)^2 \left(\frac{\chi_n^+ \chi_n^- + \chi_{n-1}^+ \chi_{n-1}^-}{2} \right)}, \quad (3.53)$$

with the generalized susceptibilities

$$\chi_n^- = \frac{\Gamma}{\Gamma + i[2\omega_0 n + (\omega_0 - \Delta\epsilon)]}, \quad \chi_n^+ = \frac{\Gamma}{\Gamma + i[2\omega_0 n + (\omega_0 + \Delta\epsilon)]}. \quad (3.54)$$

For $\Delta\epsilon = \omega_0$, we recover $\chi_n^- = \chi_n$ and $\chi_n^+ = \chi_{n+1}$. The expression for the nonlinear damping is then given by

$$\gamma_{\text{eff}}(\bar{A}) = -\frac{2g^2}{\Gamma} \left\{ \frac{4\omega_0 \Delta\epsilon}{\Gamma^2 \left(1 + \frac{\Delta\epsilon^2 - \omega_0^2}{\Gamma^2}\right)^2 + 4\omega_0^2} S_z^{(0)} - \text{Im} \left[\frac{2\Delta\epsilon}{\Gamma \left(1 + \frac{\Delta\epsilon^2 - \omega_0^2}{\Gamma^2}\right) + 2i\omega_0} S_z^{(1)} \right] \right\}. \quad (3.55)$$

3.5.2 Multistability analysis of the resonator

The behavior of the nonlinear damping as a function of the time-average amplitude \bar{A} is shown at resonance ($\Delta\epsilon = \omega_0$) in Fig. 3.5. At low amplitudes, and for low tunneling rates Γ , $\gamma_{\text{eff}} \approx \gamma_{\text{RWA}}$, i.e., the RWA is recovered. By contrast, if Γ is increased, the nonlinear damping shows a nonmonotonic and oscillatory behaviour, with maxima close to points $g\bar{A} \approx j\omega_0$, with j integer. Whenever the curve of $-\gamma_{\text{eff}}$ is equal to the intrinsic damping rate κ , a limit cycle for the resonator amplitude is found. As pictured in Fig. 3.5, the oscillatory behaviour of γ_{eff} permits the coexistence of multiple solutions. The stability of the limit cycles will depend on the gradient of $d\bar{A}/dt$ with respect to \bar{A} according to the standard analysis, i.e., a limit cycle is stable if the gradient is negative [184, 211].

Equation (3.55) allows us to compute the number of stable solutions also off-resonance ($\Delta\epsilon \neq \omega_0$), yielding the complex stability diagram pictured in Fig. 3.6(a). To test the validity of the results, it is straightforward to compare these results to the numerics, by computing the number of peaks in the steady-state Fock distribution [Fig. 3.6(b)]. Notice that the two predictions are almost equivalent, witnessing a good performance of the semiclassical approximation. In Fig. 3.6(c)-(f), I further show the average Fock occupation and the actual Fock distribution in three characteristic points of the $(\Delta\epsilon, g)$ parameter space, indicating one, two and three peaks.

To conclude this Section, I remark a strong advantage of the semiclassical approximation. Because its good agreement with the numerical calculation has been verified, it can be used to predict the onset of bi- and multistability at much lower coupling strengths, $g < 10^{-3}\omega_0$, and large quality factors, $Q > 10^5$, which are most likely to be reached in real experiments (see below, Sec. 3.7). Furthermore, the average number of photons in these cases will be generally much higher, and the semiclassical approximation is expected to work even better. In the results shown above, I was able to compare numerics and semiclassical models only for modest values of Q , yielding multistability only at large couplings $g \approx 0.1\omega_0$. For larger Q , the numerical solution of the master equation requires taking into

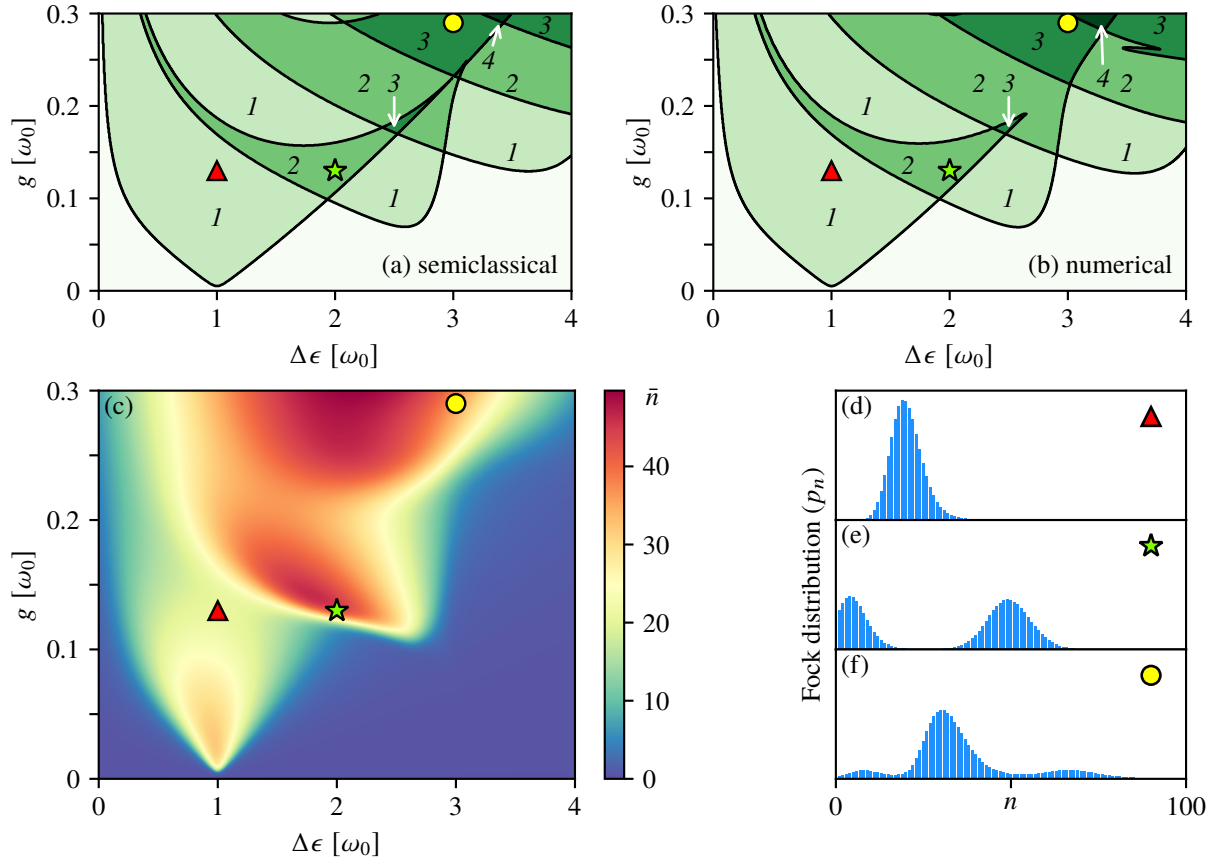


Figure 3.6: Multistability of the resonator. (a) Number of stable amplitudes of oscillations (italic numbers) obtained by semiclassical analysis. (b) Number of distinct peaks in the Fock distribution (indicated by italic numbers) obtained numerically. (c) Average photon occupation \bar{n} in the resonator as a function of spin energy splitting $\Delta\epsilon$ and spin-resonator coupling strength g . (d)-(f) Steady-state Fock distributions p_n at three different points (triangle, star, and circle). Parameters: $\Gamma_L = \Gamma_R = 0.1\omega_0$, $Q = 10^3$, $T = 0$, $P = 1$.

account many more Fock states for the resonator Hilbert space (up to $n \gtrsim 500$), making the search for the steady state prohibitively slow and memory-consuming.

3.6 Detecting lasing and multistability with transport measurements

In this Section, I describe a method to efficiently detect the lasing state in the resonator as well as the multistability. With a large bias voltage between the leads, transport is only allowed from left to right. The average stationary current through the right lead will simply be proportional to the populations of the spin levels, according to

$$I = e(\Gamma_R^\uparrow \rho_\uparrow + \Gamma_R^\downarrow \rho_\downarrow), \quad (3.56)$$

where $e > 0$ is the elementary charge. This result can also be rigorously derived using full-counting statistics (see Appendix C and Refs. 212–216). For fully polarized leads, Eq. (3.56) reduces to $I = e\Gamma_R \rho_\downarrow$, and offers a simple energy balance condition between the average number of photons in the cavity and the average current:

$$\kappa \bar{n} = \frac{I}{e}. \quad (3.57)$$

Equation (3.57) states that the outgoing flux of quanta of oscillation equals the ingoing flux of electrons in the system. When the resonator is deep into the lasing state, the small quantum fluctuations (sub-Poissonian photon statistics) reflect in the electron counting statistics through the right electrode, and the average current is much larger than its variance, ΔI . Therefore, a time-monitoring of the current provides an indirect measure of the oscillator amplitude, as sketched in Fig. 3.7(a).

3.6.1 Current jumps and two-state model

When the resonator is bistable, it is still possible to exploit current measurements to detect the bistability. For a well-developed bistability, the resonator exists in a mixed state containing two different limit cycles, which in the semiclassical pictures consist of well-separated amplitudes A_I and A_{II} , with probabilities \mathcal{P}_I and \mathcal{P}_{II} . Quantum mechanically, we have seen that the bistability appears as doubly-peaked Fock distribution, see inset of Fig. 3.4(c) and Fig. 3.6(e), with the area of the peaks roughly corresponding to \mathcal{P}_I and \mathcal{P}_{II} . If $\mathcal{P}_I \approx \mathcal{P}_{II}$, the resonator amplitude switches randomly between the two well-defined plateaus of values A_I and A_{II} . Since the current is closely connected with the resonator state, it is reasonable to assume that a time-monitoring of the current in the bistable scenario will display a *telegraph* dynamics: The current will randomly switch between plateaus of different average current, associated with different amplitudes of oscillation [217]. Figure 3.7(b) illustrates this situation with a qualitative diagram. The semiclassical treatment offers a natural interpretation of this behavior, since for each stable solution A_I , A_{II} , one has a different solution for the average current, I_I and I_{II} .

Without resorting to a time-dependent numerical simulation of the system dynamics, we can still predict whether the current will display a telegraph dynamics. Three conditions must be satisfied:

- (i) The two states interested by the bistability should have similar probabilities, $\mathcal{P}_I \approx \mathcal{P}_{II}$;
- (ii) The variance associated to each current plateau should be smaller than their distance, i.e.,

$$\Delta I_I, \Delta I_{II} \ll |I_{II} - I_I|; \quad (3.58)$$

- (iii) Each plateau should have a sufficiently long lifetime, such that separated jumps can be observable.

Under conditions (i)-(iii), the system can be approximated with a classical two-state model, with the transition rates $W_{I \rightarrow II}$ and $W_{II \rightarrow I}$. The probabilities are related to the rates through

$$\mathcal{P}_I = \frac{W_{II \rightarrow I}}{W_{I \rightarrow II} + W_{II \rightarrow I}}, \quad \mathcal{P}_{II} = \frac{W_{I \rightarrow II}}{W_{I \rightarrow II} + W_{II \rightarrow I}}, \quad (3.59)$$

and the average current will be given by the weighted average

$$I_{\text{tsm}} = \frac{W_{II \rightarrow I} I_I + W_{I \rightarrow II} I_{II}}{W_{I \rightarrow II} + W_{II \rightarrow I}}. \quad (3.60)$$

Another relevant quantity is the zero-frequency (shot) current noise, given by

$$S(0)_{\text{tsm}} = \frac{4\mathcal{P}_I\mathcal{P}_{II}(I_I - I_{II})^2}{W_{I \rightarrow II} + W_{II \rightarrow I}}, \quad (3.61)$$

where the numerator corresponds to the two-state current variance [218]. The idea is now the following: In order to prove conditions (ii) and (iii), I first take a steady resonator state satisfying (i), such as the one depicted in Fig. 3.6(e). Notice that the p_n between the two peaks is negligible, i.e., the two maxima of p_n are well separated. I identify \mathcal{P}_I and \mathcal{P}_{II} as the area of each peak, i.e., the sum of the p_n underlying each peak. Next, I set to zero the density matrix elements corresponding to one of the two states, obtaining two *truncated* density matrices which carry the information of each state separately. Using Eq. (3.56), I can calculate both I_I and I_{II} . To estimate the variance associated with each current state, we can use

$$\Delta I_{I,II} \approx \sqrt{\Gamma_R S(0)_{I,II}}, \quad (3.62)$$

where $S(0)_{I,II}$ is the zero-frequency shot noise. It can be calculated numerically using the full-counting statistics method, see Appendix C, using the truncated states. In this way, we can check condition (ii). Finally, we have access to the sum of the rates, $W_{I \rightarrow II} + W_{II \rightarrow I}$, by computing numerically the noise, $S(0)$, using the full density matrix, and then comparing it to the two-state relation Eq. (3.61). The individual rates follow through Eq. (3.59). One must then ensure *a posteriori* that both rates are much smaller than κ , which is the relaxation rate of the resonator, giving condition (iii).

In Fig. 3.7(c)-(d), I demonstrate the appropriateness of the two-state approximation for a parameter region where the oscillator develops a bistability. The solid blue line in Fig. 3.7(d) shows Eq. (3.56) calculated numerically, while the dotted lines are the single-state currents, with probabilities pictured in panel (c). The orange dashed line is the result of Eq. (3.60), which agrees well with the full numerics.

To further check the validity of the two-state model, it is possible to exploit the properties of the Liouvillian superoperator \mathcal{L} of the system. If the system is truly bistable, the current noise is dominated

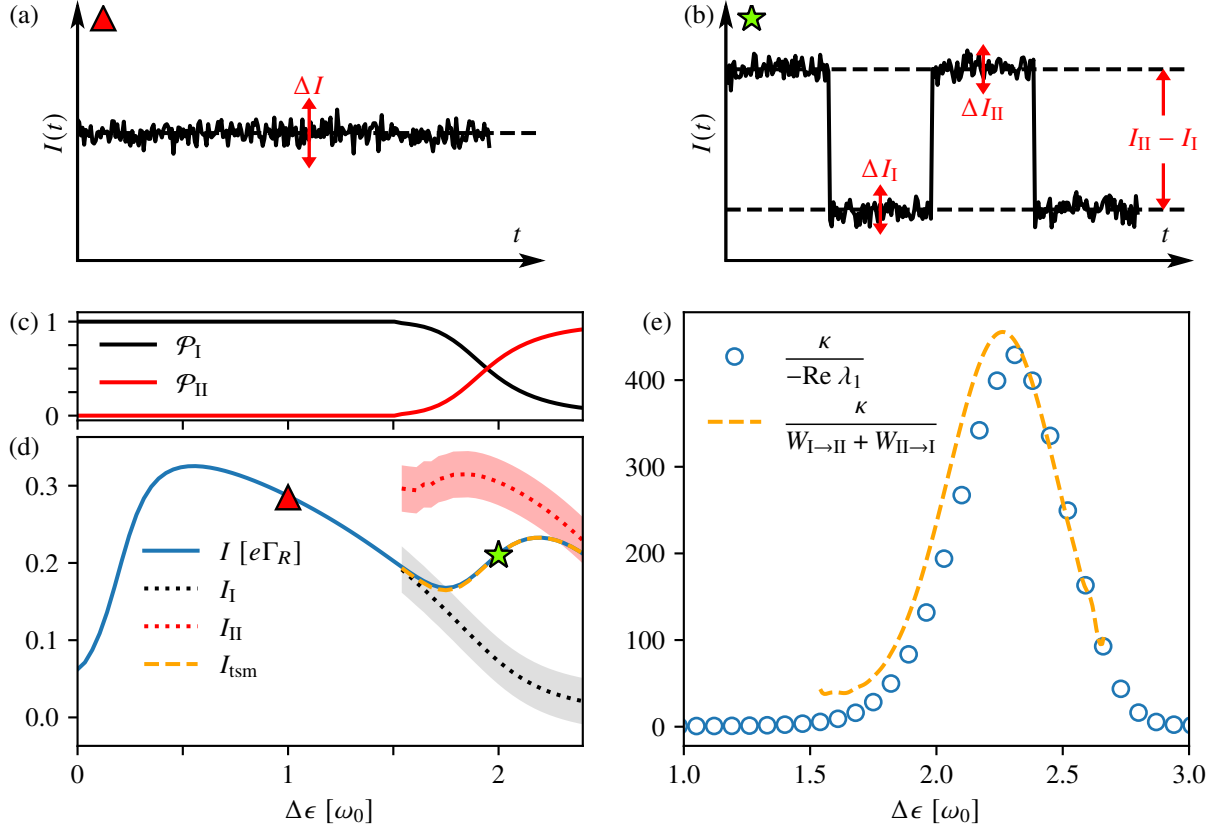


Figure 3.7: Detection of bistability through current measurements. (a) and (b): Sketch of the dc-current in real time for the case of single stable amplitude (a) and bistability (b). (c) Occupation probabilities \mathcal{P}_I and \mathcal{P}_{II} for the two states, computed numerically. (d) Average current computed numerically (solid blue line) and with the effective two-state model (orange dashed line). The upper (red) and lower (black) dotted lines show the two current states I_I and I_{II} along with their variance, represented by the shaded areas. (e) Comparison between the inverse smallest nonzero eigenvalue of the Liouvillian ($|\lambda_1|$, blue circles) and the inverse sum of the two rates, $(W_{I \rightarrow II} + W_{II \rightarrow I})^{-1}$, as obtained with the two-state model approximation (orange dashed line). The curves are rescaled to the typical relaxation time of the resonator, κ^{-1} . Parameters: $g = 0.13\omega_0$, $\Gamma_L = \Gamma_R = 0.1\omega_0$, $Q = 10^3$, $T = 0$, $P = 1$.

by a very slow timescale, which is the real part of the smallest nonzero eigenvalue, λ_1 , of \mathcal{L} . If λ_1 is small in magnitude and well-separated from the others (i.e., $|\lambda_1| \ll |\lambda_p|$ for $p > 1$), one can discard the other eigenvalues, and identify $-\text{Re } \lambda_1 = W_{\text{I} \rightarrow \text{II}} + W_{\text{II} \rightarrow \text{I}}$ by comparison with Eq. (3.61). In Fig. 3.7(e), I report the behavior of $-\text{Re } \lambda_1$ and the sum of rates obtained with the two-state model (in the bistable region of $\Delta\epsilon$, where the calculation makes sense). Despite a small difference, the agreement is quite good, showing that the dynamics of the system can truly be approximated by only two states.

The method presented above can be in principle generalized to detect more than two current plateaus, providing a simple way to detect multistability in the resonator, without the need to resort to optical detection of a mechanical motion or quantum state tomography techniques (for the case of microwave cavities).

3.7 Experimental feasibility: Multistability in nonideal cases

The scope of this Section is to provide a realizability study for the system, by considering a number of processes which can hinder the onset of lasing and multistability in the cavity. Specifically, I will consider: (a) The effect of finite polarization ($P < 1$) in the leads; (b) the effect of spin relaxation in the quantum dot; (c) for low-frequency mechanical oscillators, the effect of finite temperature and Duffing nonlinearity.

3.7.1 Effect of finite temperature and finite polarization

At finite polarization, a fraction of the total current passing through the quantum dot is elastic, i.e., no energy is exchanged with the resonator. This inevitably leads to a lower pumping efficiency, and it is natural to understand how sensitive lasing and multistability are to a decrease in ferromagnetic polarization. As a further detrimental effect, I consider here an environmental temperature which is large when compared to the resonator frequency, i.e., $T \gg \omega_0$. This condition is usually fulfilled for mechanical resonators such as carbon nanotubes (CNTs), which are a good candidate for an experimental realization of our system, see below. Indeed, their low mechanical frequency ($\omega_0/2\pi \approx 100$ MHz) requires taking into account thermal fluctuations. Conversely, for microwave cavities in the GHz regime, $n_B = 0$ is usually a good approximation at cryogenic temperatures. In Fig. 3.8, I report the numerical calculation of the average occupation of the oscillator in the steady state, together with the stability diagram for a nonideal case ($T = 10\omega_0$ and $P = 0.5$): The qualitative picture is not destroyed, as lasing and multistability are retained. More specifically, the lasing threshold is pushed to a larger coupling strength, according to Eq. (3.13), as well as the onset of bi- and multistability. The thermal noise smears out the transitions to the lasing state.

3.7.2 Effect of spin relaxation

The spin the quantum dot may be subject to spin relaxation processes due to interactions with bulk phonons in the substrate [219], or through spin-orbit coupling in CNTs [220, 221]. The overall effect of spin relaxation is to cause spin flip without photon emission into the cavity, as it does not come from

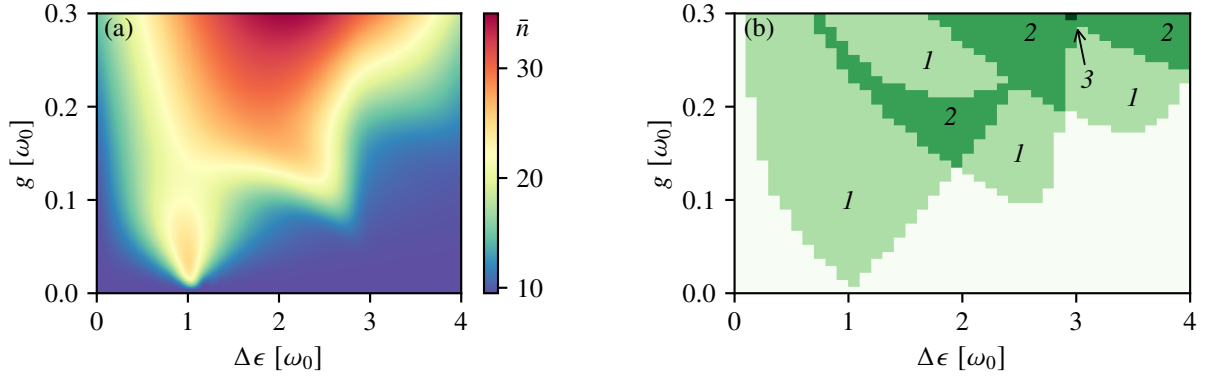


Figure 3.8: Effect of finite temperature and finite polarization. (a) Average occupation number in the oscillator at resonance as a function of the dot's energy splitting $\Delta\epsilon$ and of the spin-resonator coupling strength g . (b) Stability diagram of the resonator. Italic numbers indicate the number of distinct peaks in the Fock distribution. Parameters: $Q = 10^3$, $\Gamma = 0.1\omega_0$, $P = 0.5$, and $T = 10\omega_0$.

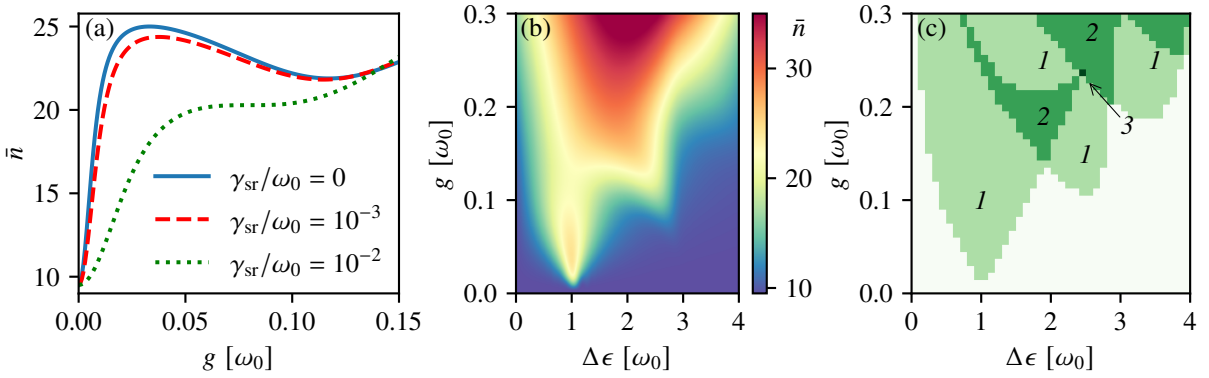


Figure 3.9: Effect of spin relaxation in the quantum dot. (a) Average phonon occupation on resonance as a function of g , for increasing values of spin relaxation rate γ_{sr} . (b) Average phonon occupation as a function of $\Delta\epsilon$ and g , for $\gamma_{\text{sr}} = 10^{-3}\omega_0$. (c) Stability diagram of the resonator for $\gamma_{\text{sr}} = 10^{-3}\omega_0$. The italic numbers indicate the number of distinct peaks in the Fock distribution. Parameters: $Q = 10^3$, $\Gamma = 0.1\omega_0$, $P = 0.5$, and $T = 10\omega_0$.

coherent energy exchange. Its role is therefore similar to the effect of finite polarization. To model the spin relaxation, I assume a typical energy relaxation time T_1 , but neglect a general inhomogeneous pure dephasing term of characteristic timescale T_ϕ . This is justified as this term generally arises in CNTs from hyperfine coupling of the electronic spin to the nuclear spin of ^{13}C atoms, whose natural abundance in carbon is less than 1% [220]. Taking the spin relaxation rate to be $\gamma_{\text{sr}} = T_1^{-1}$, I simply add a dissipator $\mathcal{L}_{\text{sr}}\rho = \gamma_{\text{sr}}\mathcal{D}(\sigma_-)[\rho]$ to the master equation (3.8) and search for the stationary state. It is reasonable to assume that if γ_{sr} is much smaller than the generalized Rabi frequency gA and of the tunneling rates Γ , the resonator dynamics is expected to be unperturbed. In Fig. 3.9(a), we observe how lasing mechanics is noticeably suppressed for $\gamma_{\text{sr}}/\omega_0 = 10^{-2}$. For the case of a CNTQD setup, the relaxation time in single-walled CNTs was reported to be $T_1 \approx 100\mu\text{s}$ at $T = 4\text{K}$ corresponding to a relaxation rate of 10 kHz. At low temperature ($T \approx 20\text{mK}$), one can expect a substantial decrease of this value. In Figs. 3.9(b)-(c) I report the average cavity occupation and the stability diagram for $\gamma_{\text{sr}} = 10^{-3}\omega_0$.

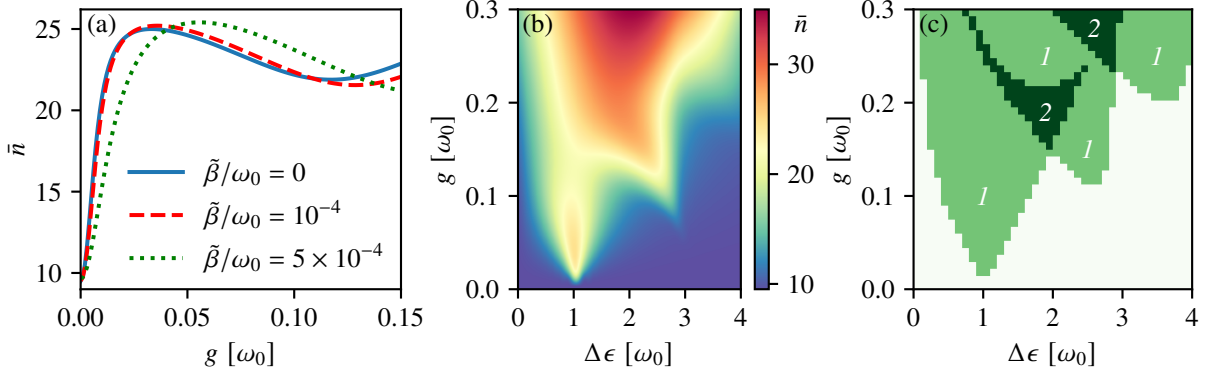


Figure 3.10: Effect of Duffing nonlinearity on the lasing, for the case of a nanomechanical resonator. (a) Average occupation for the oscillator as a function of g for three different values of the Duffing nonlinearity parameter $\tilde{\beta}$, without spin relaxation ($\gamma_{\text{sr}} = 0$). (b) Average occupation for the oscillator as a function g and $\Delta\epsilon$ for $\gamma_{\text{sr}} = 10^{-3}\omega_0$ and $\tilde{\beta} = 10^{-4}\omega_0$. (c) Stability diagram of the oscillator for $\gamma_{\text{sr}} = 10^{-3}\omega_0$ and $\tilde{\beta} = 10^{-4}\omega_0$: the italic numbers indicate the number of distinct peaks in the Fock distribution. The rest of the parameters read: $Q = 10^3$, $\Gamma = 0.1\omega_0$, $P = 0.5$, and $T = 10\omega_0$.

3.7.3 Effect of Duffing nonlinearity

Nanomechanical resonators such as suspended carbon nanotubes can be intrinsically weakly nonlinear, a property which is expected to play an important role when the amplitude of oscillations is amplified as described by our results. I include a nonlinear term of Duffing type [211] into Hamiltonian (3.2), which is modified into

$$H = \frac{\Delta\epsilon}{2}\sigma_z + \omega_0 b^\dagger b + \frac{\tilde{\beta}}{4}(b + b^\dagger)^4 + g(\sigma_+ + \sigma_-)(b + b^\dagger). \quad (3.63)$$

I have introduced $\tilde{\beta} = \beta x_{\text{ZPM}}^4$, where β is the Duffing nonlinearity parameter and $x_{\text{ZPM}} = \sqrt{\hbar/2m\omega_0}$ is the zero-point amplitude of the oscillator (\hbar has been temporarily restored for clarity). To realistically estimate $\tilde{\beta}$, let us consider a carbon nanotube with mass approximately given by $m = \pi L d / 1315$, where L and d are length and diameter in meters, respectively [222, 223]. A typical mass of $m \approx 10^{-21}$ kg gives zero-point fluctuations of order $x_{\text{ZPM}} \approx 10$ pm for a frequency $\omega_0/2\pi = 100$ MHz. Experimentally, the geometrical nonlinearity parameter for a nanotube is positive ($\beta > 0$) and of order $\beta/m = 10^{35} \text{ N kg}^{-1} \text{ m}^{-3}$ [121, 224]. It follows that $\tilde{\beta}/2\pi \approx 1$ kHz, i.e., $\tilde{\beta}/\omega_0 \approx 10^{-5}$. We neglect the electrostatic nonlinearity arising from strong coupling effects between the leads and the nanotube and from single-electron tunneling, which is in general orders of magnitude smaller and is proportional to $\Gamma \ll \omega_0$. By solving the master equation with Hamiltonian (3.63) for the steady state, I report the average cavity occupation as a function of g in Fig. 3.10(a). Finally, Figs. 3.10(b)-(c) show that the combined presence of finite temperature, finite polarization, spin relaxation and Duffing nonlinearity can still preserve the main features of the system (lasing and bistability), despite the largely nonideal case.

3.7.4 Implementations

The spin-resonator interaction lies at the heart of the physics described in this Chapter, and is the main ingredient to be sought after experimentally. Spin-valve-based carbon nanotube quantum dots

(CNTQDs) constitute a promising route to implement the model. Indeed, spin-valve effect in CNTs has been demonstrated with substantial spin polarization [124, 202], and CNTQDs have inherently small spin relaxation rate [220, 221] as well as huge quality factors [102]. Very recently, suspended CNTs have witnessed a revival interest because of their ability to support self-sustained oscillations with large amplitudes and even bistability, when driven by electron tunneling [142–144, 225]. The spin-resonator interaction in suspended CNTQDs has been the object of theoretical investigations [107, 123, 197], where an interaction strength $g_{\text{exp}} \approx 1$ MHz is predicted for a typical resonance frequency $\omega_0/2\pi = 100$ MHz. For $Q = 10^6$, $P = 0.5$, $\Gamma = 0.05\omega_0$, the threshold coupling can be as low as $g_{\text{thr}} \approx 1.6 \times 10^{-4}\omega_0$, well below g_{exp} .

Another relevant platform that can be used to realize this single-atom laser is based on spin valves coupled to microwave cavity photons. In the past few years, a great technological effort has been put into reaching an effective strong coupling between spin and photons, using, e.g., CNTQDs and superconducting microwave cavities [124, 128], silicon-based devices [125, 126, 226], and quantum dots in GaAs/AlGaAs heterostructures [127, 129, 200]. Hence, it is arguable that our device can stimulate further works in this direction.

3.8 Conclusions

To conclude, I have analyzed here a model for a single-atom laser using a quantum-dot spin valve. This single-atom laser relies on a spin-polarized current pump from ferromagnetic leads into a quantum dot, where the spin is coupled to the motion of a resonator. I have shown how the spin-resonator coupling yields a very efficient photon emission in the resonator, such that the conventional rotating-wave approximation (RWA) breaks down, despite the relative weak bare coupling achievable between spin and cavity. As a consequence of RWA-breakdown, the resonator can develop a multistable behavior, which is characterized by the presence of multiple peaks in its Fock distribution, and can be detected through simple current measurements: As each stable amplitude carries a definite current value, time-monitoring of the current shows telegraph switching between different current plateaus, as long as each stable state is sufficiently long-lived. I have analyzed the stability of the system using numerical simulations, supporting the results with a semiclassical explanation; similarly, the numerical experiments showing telegraph dynamics in the current have been confirmed by a simple two-state classical model, which assumes that the resonator state can be approximated by two well-distinct states with similar occupation probabilities. In view of an experimental realization, I have shown how the lasing and the multistability still survive when nonideal scenarios are considered, such as high environmental temperature, finite polarization of the leads, Duffing nonlinearities for the case of a mechanical resonators, and spin-relaxation processes in the quantum dots. From the above analysis, it is arguable that this system represents a unique platform for investigating the coherent dynamics of a spin coupled to a resonator *beyond* the RWA, but without the need to access ultrastrong couplings. Further, our work raises a range of interesting theoretical and experimental questions about the extent to which multistable lasing can be controlled and exploited, e.g., in nonlinear amplifiers or force sensing devices.

Chapter 4

Single-photon pump by Cooper-pair splitting

The results presented in this Chapter are published in Ref. 227.

4.1 Introduction

One of the most remarkable features of hybrid quantum-dot-based systems is the possibility of engineering correlations between distant subsystems and giving rise to nonlocal effects, which are inherently quantum mechanical. A relevant example is represented by the Cooper pairs in a superconductor, which are a natural source of entangled electrons. Cooper pairs can be split using a Cooper-pair splitter (CPS), a device widely studied both theoretically [228–242] and experimentally [145, 146, 243–251], while retaining their quantum correlations. It has been shown recently that these correlations can also give rise to peculiar thermoelectric effects [252–255]. On the other hand, I have shown in the previous Chapters how mesoscopic QED devices have proven to be excellent tools to couple electronic and bosonic degrees of freedom, enabling, in turn, the possibility to control heat exchange [256–260]. The purpose of this Chapter is to conceive and analyze a device that bridges the existing gap between the study of heat flows in quantum-dot-based [261–263] and circuit-QED devices.

I consider a CPS consisting of a superconducting lead, which is put in the proximity of two quantum dots. Each dot is further linearly coupled to a local harmonic resonator, constituted by a microwave cavity or a nanomechanical oscillator. The system is sketched in Fig. 4.1. As I show below, it is possible to obtain full control over heat and photon exchange between the two resonators by merely tuning the energy level of the quantum dots to match internal resonances of the coupled system. I will first present the model Hamiltonian and the master equation to describe the behavior of the system numerically. Next, I will develop an effective Hamiltonian formalism that explains with simplicity the induced nonlocal coupling between the cavities due to the superconductor, and the resulting heat exchange. Finally, I will quantify and discuss the efficiency of the heat transfer by computing an appropriate figure of merit.

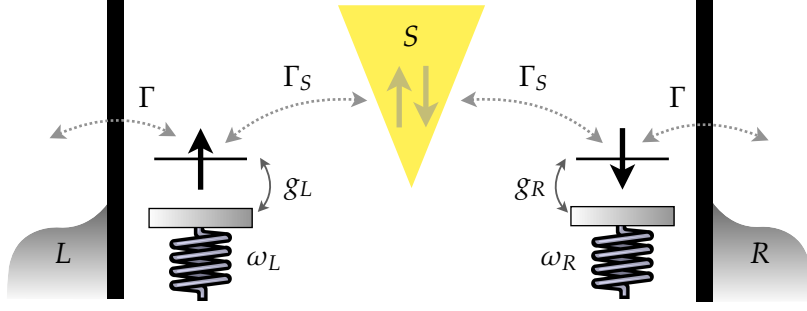


Figure 4.1: Schematics of a Cooper-pair splitter with two quantum dots coupled to local resonators.

4.2 Double-quantum-dot Cooper-pair splitter coupled to resonators

4.2.1 Cooper-pair splitter in quantum-dot setup

In order to write the full Hamiltonian of the system, I first briefly derive the effective Hamiltonian for a CPS in the limit of large superconducting gap Δ [264, 265]. A superconductor is tunnel-coupled to two quantum dots with spin-degenerate levels, each in contact with a metallic lead through a tunneling barrier (see Fig. 4.1). In principle, one can include finite intradot (U_α) and interdot (U) Coulomb repulsion strengths. The Hamiltonian for the dots thus reads:

$$H_{\text{DQD}} = \sum_{\alpha=L,R} \left[\epsilon_\alpha \sum_{\sigma} d_{\alpha\sigma}^\dagger d_{\alpha\sigma} + U_\alpha N_{\alpha\uparrow} N_{\alpha\downarrow} \right] + U \sum_{\sigma\sigma'} N_{L\sigma} N_{R\sigma'}. \quad (4.1)$$

The index $\alpha = L, R$ labels the left and right dot, respectively; $d_{\alpha\sigma}$ is the fermionic annihilation operator for an electron in the α -dot with spin σ , energy ϵ_α and corresponding number operator $N_{\alpha\sigma}$. The three leads are indexed by $\chi = L, R, S$ (left, right, and superconducting). We can write the Hamiltonian as follows:

$$H_\chi = \sum_{k\sigma} (\epsilon_{\chi k} - \mu_\chi) c_{\chi k\sigma}^\dagger c_{\chi k\sigma} - \delta_{\chi,S} \Delta \sum_k \left(c_{\chi-k\downarrow} c_{\chi k\uparrow} + \text{H.c.} \right). \quad (4.2)$$

The normal leads are described by Fermi liquids with fermionic annihilation operators $c_{\chi k\sigma}$. They are kept at a fixed chemical potential μ_χ . The superconductor is described by the BCS term with pairing potential Δ (assumed real and positive without loss of generality), and its chemical potential is taken as the reference point, $\mu_S = 0$. Next, we take into account the tunneling between the three leads and the quantum dots:

$$H_{\text{tun},N} = \sum_{k\sigma} \left[V_{NL} c_{Lk\sigma}^\dagger d_{L\sigma} + V_{NR} c_{Rk\sigma}^\dagger d_{R\sigma} + \text{H.c.} \right], \quad (4.3)$$

$$H_{\text{tun},S} = \sum_{k\sigma} \left[V_{SL} c_{Sk\sigma}^\dagger d_{L\sigma} + V_{SR} c_{Sk\sigma}^\dagger d_{R\sigma} + \text{H.c.} \right]. \quad (4.4)$$

The tunneling amplitudes $V_{N\alpha}$ and $V_{S\alpha}$ have been introduced. The CPS Hamiltonian is then given by

$$H_{\text{CPS}} = H_{\text{DQD}} + \sum_{\chi} H_{\chi} + H_{\text{tun},N} + H_{\text{tun},S}.$$

4.2.2 Large-gap and large-Coulomb-repulsion limit

Before introducing the master equation that governs the system dynamics, we consider the limits of large gap, $\Delta \rightarrow \infty$, and large intradot Coulomb repulsion, $U_{\alpha} \rightarrow \infty$.

The first approximation allows us to integrate out the superconducting degrees of freedom in the Hamiltonian, as the quasiparticles are inaccessible and no dissipation mechanism is introduced. We then obtain for the CPS:

$$H_{\text{CPS}}^{\text{eff}} = H_{\text{DQD}} - \sum_{\alpha=L,R} \frac{\Gamma_{S\alpha}}{2} \left(d_{\alpha\uparrow}^{\dagger} d_{\alpha\downarrow}^{\dagger} + \text{H.c.} \right) - \frac{\sqrt{\Gamma_{SL}\Gamma_{SR}}}{2} \left(d_{R\uparrow}^{\dagger} d_{L\downarrow}^{\dagger} - d_{R\downarrow}^{\dagger} d_{L\uparrow}^{\dagger} + \text{H.c.} \right). \quad (4.5)$$

In Eq. (4.5), we identify two contributions to the DQD Hamiltonian: The first term describes local-Andreev reflection [264, 266], whereby a Cooper pair can be transferred from the superconductor to a quantum dot (and vice-versa), with amplitude $\Gamma_{S\alpha} = 2\pi\rho_S|V_{S\alpha}|^2$ (ρ_S is the density of states at the Fermi level of the superconductor, assumed energy-independent). The second term describes cross-Andreev reflection: Cooper pairs can be split and recombined between the central superconductor and both quantum dots, building up nonlocal correlations between the two. The effective cross-Andreev coupling will be denoted by $\Gamma_S = \sqrt{\Gamma_{SL}\Gamma_{SR}}$.

The large- U_{α} approximation is usually fulfilled in experiments since the charging energy of the dots can reach several meV and is therefore larger than all other energy scales in the system [146]. Physically, this means that double occupation in the dots is energetically inaccessible, and the local-Andreev reflection contributions in Eq. (4.5) can be neglected. The CPS Hamiltonian becomes

$$H_{\text{CPS}}^{\text{eff}} = H_{\text{DQD}} - \frac{\Gamma_S}{2} \left(d_{R\uparrow}^{\dagger} d_{L\downarrow}^{\dagger} - d_{R\downarrow}^{\dagger} d_{L\uparrow}^{\dagger} + \text{H.c.} \right). \quad (4.6)$$

Notice that, for large U_{α} , the relevant Hilbert spaces for the double dot system is spanned by nine states: The empty state $|0\rangle$, four singly occupied states $|\alpha\sigma\rangle = d_{\alpha\sigma}^{\dagger}|0\rangle$, the singlet state $|S\rangle = \frac{1}{\sqrt{2}} \left(d_{R\uparrow}^{\dagger} d_{L\downarrow}^{\dagger} - d_{R\downarrow}^{\dagger} d_{L\uparrow}^{\dagger} \right) |0\rangle$, the unpolarized triplet state $|T0\rangle = \frac{1}{\sqrt{2}} \left(d_{R\uparrow}^{\dagger} d_{L\downarrow}^{\dagger} + d_{R\downarrow}^{\dagger} d_{L\uparrow}^{\dagger} \right) |0\rangle$ and two polarized triplet states $|T\sigma\rangle = d_{R\sigma}^{\dagger} d_{L\sigma}^{\dagger} |0\rangle$. In the subgap limit, the cross-Andreev reflection term hybridizes only the states $|0\rangle$ and $|S\rangle$ of the double dot: Only Cooper pairs in singlet states can be split and recombined with the coherent amplitude Γ_S . The hybridization gives rise to the Andreev bound states

$$\begin{aligned} |+\rangle &= \cos \frac{\theta}{2} |0\rangle + \sin \frac{\theta}{2} |S\rangle, \\ |-\rangle &= -\sin \frac{\theta}{2} |0\rangle + \cos \frac{\theta}{2} |S\rangle, \end{aligned} \quad (4.7)$$

with the mixing angle $\theta = \arctan \left(\frac{\sqrt{2}\Gamma_S}{\epsilon_L + \epsilon_R + U} \right)$. The energy splitting between the Andreev states is $\delta = \sqrt{(\epsilon_L + \epsilon_R + U)^2 + 2\Gamma_S^2}$.

4.2.3 Capacitive coupling to resonators

Finally, we include a capacitive charge coupling between each quantum dot and a local harmonic resonator of frequency ω_α and bosonic field operator b_α [117, 118, 122, 136, 267]. Assuming a negligible interdot Coulomb interaction U , the system Hamiltonian that I will consider is then

$$H = \sum_{\alpha\sigma} \epsilon_\alpha N_{\alpha\sigma} - \frac{\Gamma_S}{2} (d_{R\uparrow}^\dagger d_{L\downarrow}^\dagger - d_{R\downarrow}^\dagger d_{L\uparrow}^\dagger + \text{H.c.}) + \sum_\alpha \omega_\alpha b_\alpha^\dagger b_\alpha + \sum_{\alpha\sigma} g_\alpha (b_\alpha + b_\alpha^\dagger) N_{\alpha\sigma}. \quad (4.8)$$

The strength of the linear interaction between dot and resonator is labeled by g_α .

4.3 Master equation and stationary current

The electron tunneling into the normal leads and the dissipation processes in the resonators will be treated to lowest order in perturbation theory, such that the effective reduced dynamics for the coupled CPS-resonators system can be described by rate equations involving only the populations of the eigenstates of Hamiltonian (4.8) [238, 265, 268, 269]. From Eq. (4.3), we define the following dot-lead tunneling rates: $\Gamma_L = 2\pi\rho_L|V_{NL}|^2$ and $\Gamma_R = 2\pi\rho_R|V_{NR}|^2$, where ρ_L and ρ_R are the density of states in the leads at the Fermi level, assumed constant. The resonators have quality factors $Q_\alpha = \omega_\alpha/\kappa_\alpha$, where κ_α is the cavity decay rate. To fulfill the sequential-tunneling and the low-damping regime, one must ensure the conditions $\Gamma_\alpha \ll \{\Gamma_S; k_B T\}$ and $\kappa_\alpha \ll \{\omega_\alpha; k_B T\}$, where T is the environmental temperature of the fermionic and bosonic reservoirs. Labeling with $|i\rangle$ the eigenstates of Hamiltonian (4.8), the electronic and bosonic transition rates between two eigenstates are given by Fermi's golden rule [270]:

$$w_{\text{el},j\leftarrow i}^{\alpha,s} = \Gamma_\alpha f_\alpha^{(s)}(sE_{ji}) \sum_\sigma |\langle j|d_{\alpha\sigma}^{(s)}|i\rangle|^2, \quad (4.9)$$

$$w_{\text{ph},j\leftarrow i}^{\alpha,s} = s\kappa_\alpha n_B(E_{ji}) \sum_\sigma |\langle j|b_\alpha^{(s)}|i\rangle|^2. \quad (4.10)$$

We have introduced the generalized Fermi and Bose functions:

$$f_\alpha^{(s)}(x) = \frac{1}{\exp\left[\frac{s(x-\mu_\alpha)}{k_B T}\right] + 1}, \quad (4.11)$$

$$n_B(x) = \frac{1}{\exp\left[\frac{x}{k_B T}\right] - 1}, \quad (4.12)$$

with $s = \pm$. $E_{ji} = E_j - E_i$ denotes the energy difference between two eigenstates. Notice that it is reasonably implied that the spectrum of Hamiltonian (4.8) is nondegenerate. For the sake of compactness in Eqs. (4.11)-(4.12), I have provisionally used the notation $d_{\alpha\sigma}^{(-)}$ [$d_{\alpha\sigma}^{(+)}$] for the fermionic annihilation

(creation) operators. A similar shorthand holds for the bosonic operators. Let us define the total transition rates as

$$w_{j \leftarrow i} = \sum_{\alpha s} (w_{\text{el}, j \leftarrow i}^{\alpha, s} + w_{\text{ph}, j \leftarrow i}^{\alpha, s}). \quad (4.13)$$

The populations P_i of the system eigenstates will then obey the Pauli-type master equation

$$\dot{P}_i = \sum_j w_{i \leftarrow j} P_j - \sum_j w_{j \leftarrow i} P_i. \quad (4.14)$$

Equation (4.14) admits a stationary solution, represented by the vector the stationay populations P_i^{st} . It can be found by setting $\dot{P}_i = 0$ and consequently solving the resulting linear system. The stationary vector corresponds to the null space of the matrix \mathbf{W} with matrix elements $W_{ij} = w_{i \leftarrow j} - \delta_{ij} \sum_k w_{k \leftarrow j}$. It can be found numerically using standard linear algebra methods [271], and adding the normalization condition for the populations, $\sum_i P_i = 1$. The matrix elements of \mathbf{W} satisfy the sum rule $\sum_i W_{ij} = 0$, i.e., the sum of the elements in each column of \mathbf{W} vanishes.

The steady populations give us access to expression for particle and energy (or heat) currents [270]. For electrons, they read

$$I_\alpha = e \sum_{i,j,s} s w_{\text{el}, j \leftarrow i}^{\alpha, s} P_i^{\text{st}}, \quad (4.15)$$

$$\dot{Q}_\alpha = \sum_{i,j,s} E_{ij} w_{\text{el}, j \leftarrow i}^{\alpha, s} P_i^{\text{st}} - \frac{\mu_\alpha}{e} I_\alpha. \quad (4.16)$$

The corresponding expressions for photon particle and energy currents are similarly

$$I_\alpha^{\text{ph}} = \sum_{i,j,s} s w_{\text{ph}, j \leftarrow i}^{\alpha, s} P_i^{\text{st}}, \quad (4.17)$$

$$\dot{Q}_\alpha^{\text{ph}} = \sum_{i,j,s} E_{ij} w_{\text{ph}, j \leftarrow i}^{\alpha, s} P_i^{\text{st}}. \quad (4.18)$$

For electrons, I have multiplied the particle current in Eq. (4.15) by the electron's charge e to get an electric current. Notice that, in contrast to the metallic leads, the bosonic reservoirs are at zero chemical potential, so the heat current coincides with the energy current.

4.3.1 Large bias limit and stationary current in the absence of resonators

In the rest of the analysis, I will assume that the normal leads are negatively biased with respect to the Fermi level of the superconductor, such that $\mu_\alpha = -eV$, where $V > 0$ is the applied bias voltage. Furthermore, the bias voltage is assumed to be very large, such that $\{U; \Delta\} \gg eV \gg \{k_B T; \Gamma_S\}$. In this regime, electrons will flow unidirectionally from the superconductor via the quantum dots into the

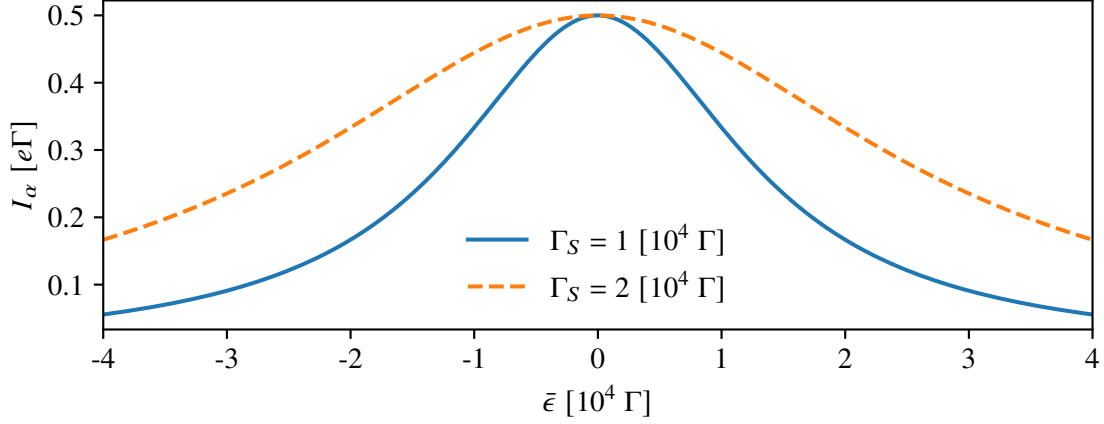


Figure 4.2: Andreev stationary current through a normal lead, in absence of resonators, as a function of the average dot level $\bar{\epsilon} = (\epsilon_L + \epsilon_R)/2$ for two values of Γ_S .

leads. Transport in the opposite direction will be blocked, as the rates $w_{\text{el},j \leftarrow i}^{\alpha,+}$ vanish. Furthermore, the temperature of the leads becomes irrelevant. The electric current flowing in the lead is simply given by $I_\alpha = e\Gamma_\alpha \sum_\sigma \langle N_{\alpha\sigma} \rangle$, with the average performed on the steady state. It is worth noticing that the negative bias also reduces the number of available states in the double dot: The triplet states $|T0\rangle$ and $|T\sigma\rangle$ can be excluded from the computation, as they can only appear due to the blocked lead-to-dot tunneling.

In absence of resonators, the stationary solution to master equation (4.14) can be found analytically. Hence, we can find a simple expression for the stationary current with largely negatively-biased leads, assuming $\Gamma_L = \Gamma_R = \Gamma$ without loss of generality:

$$I_L = I_R = e\Gamma \frac{\Gamma_S^2}{(\epsilon_L + \epsilon_R)^2 + 2\Gamma_S^2}. \quad (4.19)$$

The average current flows equally through both leads, and is pictured in Fig. 4.2 along the direction of the average dot level, $\bar{\epsilon} = (\epsilon_L + \epsilon_R)/2$. It is a lorentzian centered around $\bar{\epsilon} = 0$ with width proportional to Γ_S , and has a simple physical meaning: When $\bar{\epsilon}$ lies closely to the Fermi level of the superconductor, the hybridization between the singlet and empty states is maximized. Cooper pairs injected in the separate dots can then tunnel into the corresponding leads through single-electron events generating a current. The transport window broadens with increasing Γ_S as it leads to a stronger hybridization.

The transport mechanism can be better understood with the help of Fig. 4.3. When the leads are negatively biased, the double dot in the singlet state $|S\rangle$ decays into a singly-occupied state ($|\alpha\sigma\rangle$) through a single-electron tunneling event, giving up an electron to one of the leads, at the incoherent rate Γ . Similarly, the remaining electron will tunnel out, leaving the double dot in the empty state $|0\rangle$, see Fig. 4.3(a). However, the empty and the singlet state are coherently coupled with amplitude Γ_S , allowing the cycle to restart and giving rise to the steady current pictured in Fig. 4.2.

An interesting situation appears when the charge states are only *weakly* hybridized, i.e., whenever $|\epsilon| \gtrsim \Gamma_S$. In this case, for positive ϵ , the Andreev bound state $|+\rangle$ is “mostly” the singlet state, while the state $|-\rangle$ is “mostly” empty, see Fig. 4.3(b). This leads to a strong asymmetry of the transition rates $|+\rangle \leftrightarrow |\alpha\sigma\rangle$ and $|-\rangle \leftrightarrow |\alpha\sigma\rangle$. The situation is reversed when $\epsilon < 0$, as weak hybridization implies $|+\rangle \approx |0\rangle$ and $|-\rangle \approx |S\rangle$. This strong asymmetry lies at the heart of the photon transfer mechanism that I

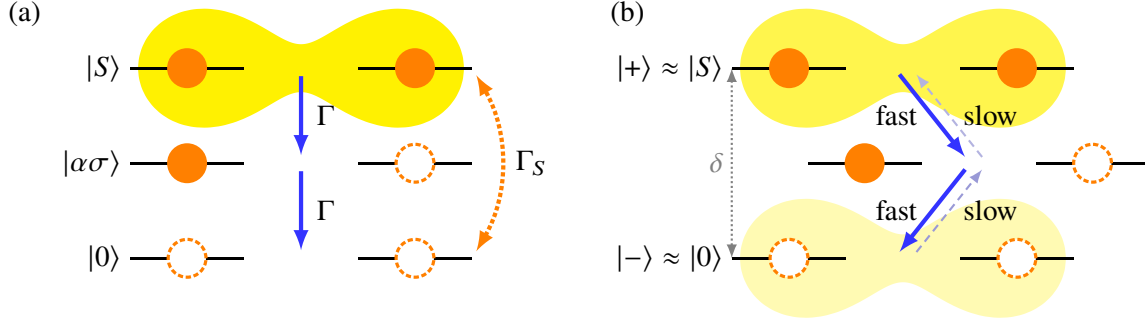


Figure 4.3: (a) For negatively biased leads, subsequent incoherent tunneling events bring the singlet state into the empty state. The two states are coherently coupled due to the superconductors, leading to a stationary current. (b) The coherent coupling leads to the formation of the Andreev bound states $|\pm\rangle$, with energy separation δ . For weak hybridization ($|\epsilon| \gtrsim \Gamma_S$) the transition rates $|+\rangle \leftrightarrow |\alpha\sigma\rangle$ and $|-\rangle \leftrightarrow |\alpha\sigma\rangle$ are strongly asymmetric. Here, the situation for $\epsilon > 0$ is pictured.

will describe below.

4.4 Polaron transformation and effective Hamiltonian

Before showing the main features of the system through numerical calculations, I perform a polaron transformation on Hamiltonian (4.8), which facilitates the unraveling of the physical processes I want to address. For a given operator O , let us define the unitary transformation

$$\bar{O} = e^{\xi} O e^{-\xi}, \quad \text{with} \quad \xi = \sum_{\alpha\sigma} \Pi_{\alpha} N_{\alpha\sigma} \quad \text{and} \quad \Pi_{\alpha} = \frac{g_{\alpha}}{\omega_{\alpha}} (b_{\alpha}^{\dagger} - b_{\alpha}). \quad (4.20)$$

Equation (4.20) is an example of polaron transformation [272], widely used also in the context of quantum transport [273, 274]. The application of Eq. (4.20) to Eq. (4.8) leads to the polaron-transformed Hamiltonian

$$\bar{H} = \sum_{\alpha\sigma} \bar{\epsilon}_{\alpha} \left(N_{\alpha\sigma} + \frac{|S\rangle\langle S|}{2} \right) - \frac{\Gamma_S}{\sqrt{2}} \left(|S\rangle\langle 0|X + |0\rangle\langle S|X^{\dagger} \right) + \sum_{\alpha} \omega_{\alpha} b_{\alpha}^{\dagger} b_{\alpha}, \quad (4.21)$$

with $\bar{\epsilon}_{\alpha} = \epsilon_{\alpha} - \frac{g_{\alpha}^2}{\omega_{\alpha}}$ and $X = \exp(\sum_{\alpha} \Pi_{\alpha})$. In this representation, the linear interaction term appearing in Eq. (4.8) now emerges as a transverse interaction between the $|S\rangle$ and $|0\rangle$ states and the resonators, to *all* orders in g_{α} , through the operator X . More intriguingly, this interaction is purely nonlocal since it vanishes for $\Gamma_S = 0$.

At this point, I make the assumption of small coupling, $g_{\alpha} \ll \omega_{\alpha}$. The operators X and X^{\dagger} can be expanded up to second order in g_{α} , such that the interaction term in Eq. (4.21) becomes:

$$\bar{H}_{\text{int}} = -\frac{\Gamma_S}{\sqrt{2}} \left[i\sigma_y \Pi + \sigma_x \left(1 + \frac{\Pi^2}{2} \right) \right] + \mathcal{O}(\Pi^3), \quad (4.22)$$

with the definitions: $i\Pi = \sum_{\alpha} i\Pi_{\alpha}$ (generalized total momentum), $\sigma_x = |0\rangle\langle S| + \text{H.c.}$, and $\sigma_y =$

$-i|0\rangle\langle S| + \text{H.c.}$ By diagonalizing the interaction in the electronic subspace, we obtain the renormalized hybridized states

$$|\bar{+}\rangle = \cos\left(\frac{\bar{\theta}}{2}\right)|0\rangle + \sin\left(\frac{\bar{\theta}}{2}\right)|S\rangle, \quad (4.23)$$

$$|\bar{-}\rangle = -\sin\left(\frac{\bar{\theta}}{2}\right)|0\rangle + \cos\left(\frac{\bar{\theta}}{2}\right)|S\rangle, \quad (4.24)$$

with $\bar{\theta} = \arctan\left(\frac{\sqrt{2}\Gamma_S}{\bar{\epsilon}_L + \bar{\epsilon}_R}\right)$. The renormalized energy splitting then reads $\bar{\delta} = \sqrt{(\bar{\epsilon}_L + \bar{\epsilon}_R)^2 + 2\Gamma_S^2}$. Using this new basis, we define the Pauli algebra with matrices $\tau_+ = |\bar{+}\rangle\langle\bar{-}|$, $\tau_- = (\tau_+)^{\dagger}$, $\tau_x = \tau_+ + \tau_-$, $\tau_y = -i(\tau_+ - \tau_-)$, $\tau_z = [\tau_+, \tau_-]$, through which Eq. (4.21) up to second order becomes

$$\bar{H} = \sum_{\alpha\sigma} \bar{\epsilon}_{\alpha} N_{\alpha\sigma} + \frac{\bar{\delta}}{2} \tau_z + \sum_{\alpha} \omega_{\alpha} b_{\alpha}^{\dagger} b_{\alpha} - \frac{\Gamma_S}{2\sqrt{2}} \left[2i\tau_y \Pi + (\sin \bar{\theta} \tau_z + \cos \bar{\theta} \tau_x) \Pi^2 \right] + O(\Pi^3). \quad (4.25)$$

We now move to the interaction picture with respect to the free Hamiltonian $H_0 = \sum_{\alpha\sigma} \bar{\epsilon}_{\alpha} N_{\alpha\sigma} + \frac{\bar{\delta}}{2} \tau_z + \sum_{\alpha} \omega_{\alpha} b_{\alpha}^{\dagger} b_{\alpha}$. We obtain the time-dependent interaction Hamiltonian

$$\begin{aligned} \bar{H}_{\text{int}}(t) = & - \sum_{\alpha} \frac{g_{\alpha} \Gamma_S}{\omega_{\alpha} \sqrt{2}} \left(e^{i\omega_{\alpha} t} b_{\alpha}^{\dagger} - e^{-i\omega_{\alpha} t} b_{\alpha} \right) \left(e^{i\bar{\delta} t} \tau_+ - e^{-i\bar{\delta} t} \tau_- \right) \\ & - \frac{\Gamma_S g_L g_R}{\sqrt{2} \omega_L \omega_R} \left[e^{i\Omega t} b_L^{\dagger} b_R^{\dagger} + e^{-i\Omega t} b_L b_R - e^{i(\Delta\omega)t} b_L^{\dagger} b_R - e^{-i(\Delta\omega)t} b_L b_R^{\dagger} \right] \\ & \times \left[\sin(\bar{\theta}) \tau_z + \cos(\bar{\theta}) \left(e^{i\bar{\delta} t} \tau_+ + e^{-i\bar{\delta} t} \tau_- \right) \right] \\ & - \sum_{\alpha} \frac{\Gamma_S g_{\alpha}^2}{2\sqrt{2} \omega_{\alpha}^2} \left[e^{2i\omega_{\alpha} t} \left(b_{\alpha}^{\dagger} \right)^2 + e^{-2i\omega_{\alpha} t} b_{\alpha}^2 - 2b_{\alpha}^{\dagger} b_{\alpha} - 1 \right] \\ & \times \left[\sin(\bar{\theta}) \tau_z + \cos(\bar{\theta}) \left(e^{i\bar{\delta} t} \tau_+ + e^{-i\bar{\delta} t} \tau_- \right) \right] + O(g_{\alpha}^3 / \omega_{\alpha}^3). \end{aligned} \quad (4.26)$$

I have introduced the sum, $\Omega = \omega_L + \omega_R$, and the difference, $\Delta\omega = \omega_L - \omega_R$, of the resonator frequencies. Equation (4.26) is the central object that contains the resonant processes I will discuss below using a suitable rotating-wave approximation.

4.5 Simultaneous ground-state cooling of nanoresonators

The first main feature offered by our system is the possibility to obtain *simultaneous* ground-state cooling of the resonators, as well as simultaneous heating. To achieve this, we tune the dots' energy levels to the same value $\epsilon_L = \epsilon_R = \epsilon$ and assume two identical resonators, with $\omega_L = \omega_R = \omega$, $g_L = g_R = g$, and $Q_L = Q_R = Q$. Furthermore, we move close to the resonance condition $\bar{\delta} = \omega$. Notice that this is fulfilled by two values of ϵ of opposite sign, namely $\epsilon = \pm \sqrt{\omega^2 - 2\Gamma_S^2}$. Close to the resonance, we can perform a rotating-wave approximation in Eq. (4.26), obtaining to first order in g/ω the simple, time-independent interaction

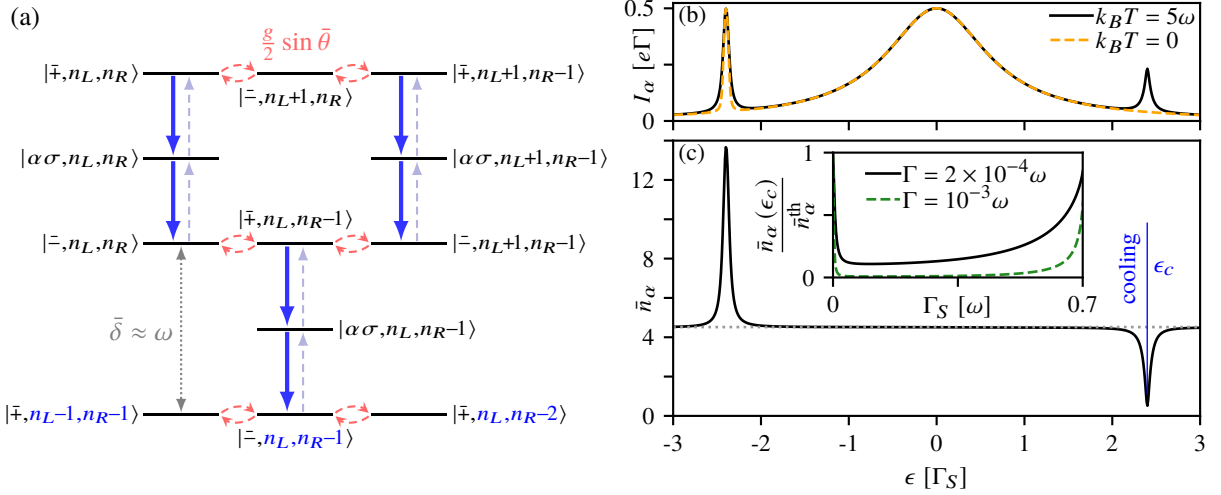


Figure 4.4: Simultaneous cooling of resonators due to cross-Andreev reflection. (a) For two identical resonators, when $|\epsilon| \gtrsim \Gamma_S$ and $\epsilon > 0$, the weak charge hybridization leads to an asymmetry in the transition rates $|\bar{+}\rangle \leftrightarrow |\alpha\sigma\rangle$ and $|\bar{-}\rangle \leftrightarrow |\alpha\sigma\rangle$. Fast rates are depicted by blue solid arrows, slow transition with dashed light blue arrows. The coherent effective coupling [Eq. (4.27), curved dashed arrows] mixes states with different photon numbers close to the resonance $\bar{\delta} = \omega$. In the steady nonequilibrium state of the system, the cavities are effectively cooled down. (b) Current I_α as a function of the on-site dot energy ϵ at zero (red dashed line) and finite temperature (solid black line). (c) Average cavity occupation in one of the cavities, for $k_B T = 5\omega$. The horizontal dotted line corresponds to the thermal occupation. Inset: Photon occupation at the cooling resonance, $\epsilon = \epsilon_c$, as a function of Γ_S , for two different values of the electron tunneling rate Γ . The curves are rescaled to the thermal occupation. Parameters: $\Gamma = 2 \times 10^{-4}\omega$, $g = 0.02\omega$, $Q = 10^5$, $\Gamma_S = 0.2\omega$.

$$\bar{H}_{\text{loc}} = \sum_{\alpha} \frac{g}{2} \sin \bar{\theta} (b_{\alpha} \tau_{+} + b_{\alpha}^{\dagger} \tau_{-}). \quad (4.27)$$

Equation (4.27) describes hopping between the Andreev states $|\bar{+}\rangle$ and $|\bar{-}\rangle$ associated with one-photon loss and absorption in the cavities, through a Jaynes-Cummings interaction. Notice that the effective coupling is proportional to $\sin \bar{\theta} = \sqrt{2}\Gamma_S/\bar{\delta}$, and is therefore a direct consequence of nonlocal Andreev reflection.

We can illustrate how this effective interaction leads to ground-state cooling of both cavities with the help of Fig. 4.4(a). The interaction (4.27) coherently mixes the states $|\bar{+}, n_L, n_R\rangle$, $|\bar{-}, n_L + 1, n_R\rangle$, and $|\bar{-}, n_L, n_R + 1\rangle$, which are degenerate for $\bar{H}_{\text{loc}} = 0$. When $|\epsilon| \gtrsim \Gamma_S$, the hybridization of the states $|0\rangle$ and $|S\rangle$ is weak. What happens now depends on the sign of ϵ : If $\epsilon < 0$, then $|\bar{+}\rangle \approx |0\rangle$ and $|\bar{-}\rangle \approx |S\rangle$. Conversely, for $\epsilon > 0$, $|\bar{+}\rangle \approx |S\rangle$ and $|\bar{-}\rangle \approx |0\rangle$. Let us consider the latter case. As discussed in Sec. 4.3.1, the weak hybridization leads to the *fast* transitions $|\bar{+}\rangle \rightarrow |\alpha\sigma\rangle \rightarrow |\bar{-}\rangle$ and the *slow* transitions $|\bar{+}\rangle \leftarrow |\alpha\sigma\rangle \leftarrow |\bar{-}\rangle$, which conserve the photon number. When an electron reaches the state $|\bar{-}\rangle \approx |0\rangle$, the coherent cycle restarts due to the effective coupling, leading to further $|\bar{+}\rangle \rightarrow |\alpha\sigma\rangle \rightarrow |\bar{-}\rangle$ transitions. During each cycle, however, a boson is subtracted from both cavities, see Fig. 4.4(a). The process continues until the loss mechanisms in the resonators lead to a steady nonequilibrium state, which leaves the cavities cooled down. The opposite occurs for $\epsilon < 0$: In this case, the cavities are heated as in each coherent cycle a photon is pumped into them.

To prove the qualitative description I have just presented, I show in Fig. 4.4(b)-(c) the electric current through one lead and the average photon occupation, $\bar{n}_{\alpha} = \langle b_{\alpha}^{\dagger} b_{\alpha} \rangle$, for one cavity as a function of ϵ ,

finding the numerical steady solution of Eq. (4.14) with the full Hamiltonian (4.8). The current presents the characteristic broad resonance described in Sec. 4.3.1. However, at zero temperature, the inelastic peak appears at $\epsilon = -\sqrt{\omega^2 - 2\Gamma_S^2}$, which is associated to heating. At finite temperature, the second sideband peak emerges at positive ϵ , associated with cavity cooling.

In the inset of Fig. 4.4(c) I further demonstrate how the cooling can be very effective, robustly bringing the resonators into their ground state, as witnessed by the value of $\bar{n}_\alpha \ll 1$. The inset shows an optimal cooling region over a wide range of values of Γ_S , which is the result of the interplay between the effective coupling $g/2 \sin \bar{\theta}$, vanishing for $\Gamma_S \rightarrow 0$, and the hybridization between $|0\rangle$ and $|S\rangle$: A strong hybridization (achieved with large Γ_S) reduces the asymmetry between the transition rates $|\pm\rangle \leftrightarrow |\alpha\sigma\rangle$, deteriorating the cooling effect.

4.6 Photon transfer between resonators

The local cooling mechanism presented in Sec. 4.5 is due to one-photon resonances, and can be simply explained by analyzing the first-order term of Eq. (4.26). By keeping the second-order term, it is possible to describe the resonance $\bar{\delta} = \omega_L - \omega_R$. Let us assume, without loss of generality, $\omega_L > \omega_R$. For $\bar{\delta} = \omega_L - \omega_R$, the rotating-wave approximation yields the effective coupling Hamiltonian

$$H_{\text{RWA}}^{(-)} = \sum_{\alpha} \frac{\Gamma_S g_{\alpha}^2}{2\sqrt{2}\omega_{\alpha}^2} (2n_{\alpha} + 1) \sin \bar{\theta} \tau_z + g_{\text{NL}} \left(b_L^{\dagger} b_R \tau_- + \text{H.c.} \right), \quad (4.28)$$

with the effective nonlocal coupling strength

$$g_{\text{NL}} = \frac{\Gamma_S g_L g_R}{\sqrt{2}\omega_L \omega_R} \cos \bar{\theta}. \quad (4.29)$$

Notice that, once again, Hamiltonian (4.28) is purely nonlocal as it vanishes for $\Gamma_S = 0$. It is composed of two terms. Let us focus first on the second term. It describes coherent processes in which the superconductor mediates photon transfer between the resonators, by coupling the subspaces $|\bar{+}, n_L - 1, n_R + 1\rangle$ and $|\bar{-}, n_L, n_R\rangle$ [see Fig. 4.5(a)]. This term vanishes for identical resonators, as it would require $\bar{\delta} = 0$ and therefore $\Gamma_S = 0$. The mechanism which leads to a steady photon flow between the cavities is similar to the cooling mechanism described in Sec. 4.5: The unbalance in the transition rates due to the weak charge hybridization facilitates the processes whereby the left resonator loses a photon, which is transferred to the right cavity. In the steady state, a stationary heat flow is established between the oscillators [see also the inset of Fig. 4.6(b)]. In Fig. 4.5(b), I also report the electronic current calculated numerically with the full Hamiltonian for the case of two resonators with different frequencies. A number of resonances appear, including the one-photon resonances discussed in Sec. 4.5, the two-photon resonance $\bar{\delta} = \omega_L - \omega_R$, as well as multiphoton resonances which are described in Sec. 4.8 and are a generalization of the process I just described.

The first term in Hamiltonian (4.28) is proportional to $n_{\alpha} \tau_z$, and can be regarded as a dispersive shift of the cavity frequencies, depending on the Andreev bound state. This translates into a fine double-peak

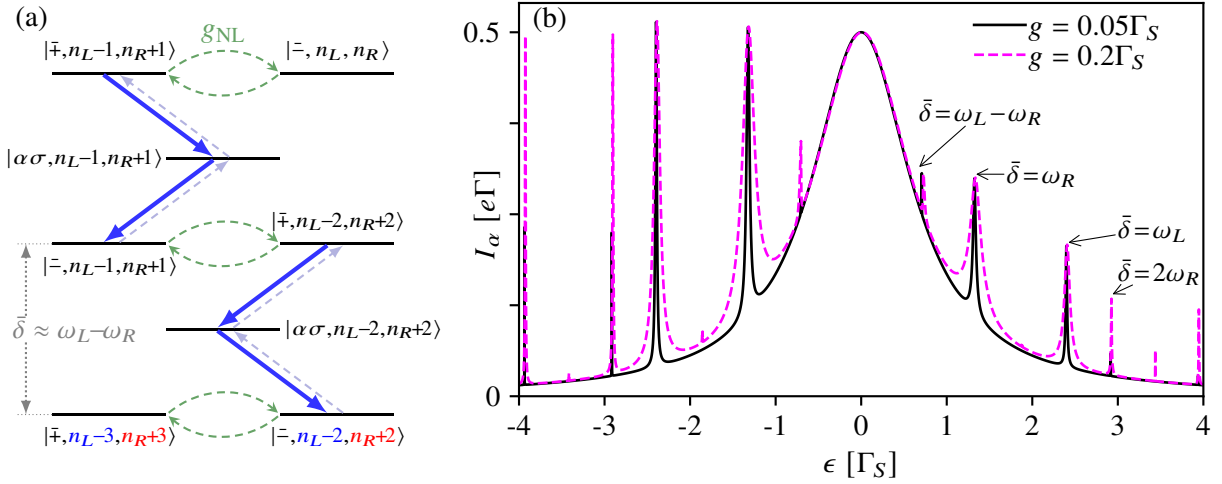


Figure 4.5: (a) Sketch of the nonlocal photon transfer mechanism, occurring when $\bar{\delta} \approx \omega_L - \omega_R$. (b) Electronic current through one lead, as a function of the dots' level ϵ , for two different values of $g = g_L = g_R$. A few resonances described by Eq. (4.32) are indicated by arrows. Parameters: $\Gamma = 10^{-4}\Gamma_S$, $\omega_L = 5\Gamma_S$, $\omega_R = 3\Gamma_S$, $Q_L = Q_R = 10^5$, $k_B T = 5\Gamma_S$.

structure of the nonlocal resonance, see Fig. 4.6(b), because the quantities calculated using Eq. (4.14) are density-matrix averages.

4.7 Efficiency

To understand the extent to which the system is able to cool the cavities locally or transfer photons between them, we can quantify the efficiency of these processes with the help of Eq. (4.18). The quantity $\dot{Q}_\alpha^{\text{ph}}$ measures the stationary heat current flowing from the bosonic reservoir α to the corresponding resonator. It is negative (positive) when the resonator is cooled (heated), and vanishes for an oscillator in thermal equilibrium. For the case of local cooling, dividing this quantity by the resonator frequency ω_α gives us an estimate of the energy quanta lost by the resonator on average per unit time. We can then compare this number to the rate at which Cooper pairs are injected into the system, which is given by $|I_S|/2e$. The Andreev current through the superconductor $I_S = -I_L - I_R$ follows from current conservation. The natural definition of the local cooling efficiency for the α -resonator is then

$$\eta_{\text{loc}}^{(\alpha)} = \frac{|\dot{Q}_\alpha^{\text{ph}}|}{\omega_\alpha} \frac{2e}{|I_S|}. \quad (4.30)$$

In a similar fashion, when around the resonance $\bar{\delta} = \omega_L - \omega_R$, the photon transfer efficiency is defined as

$$\eta_{\text{NL}} = \frac{|\dot{Q}_L^{\text{ph}} - \dot{Q}_R^{\text{ph}}|}{\omega_L - \omega_R} \frac{2e}{|I_S|}. \quad (4.31)$$

The results for Eqs. (4.30) and (4.31) are shown in Fig. 4.6, close to the corresponding resonances. In both cases, the efficiency can reach 90%: Almost one photon is absorbed from each cavity (local cooling) or transferred from the left to the right cavity (nonlocal transfer) for each Cooper pair split into the dots.

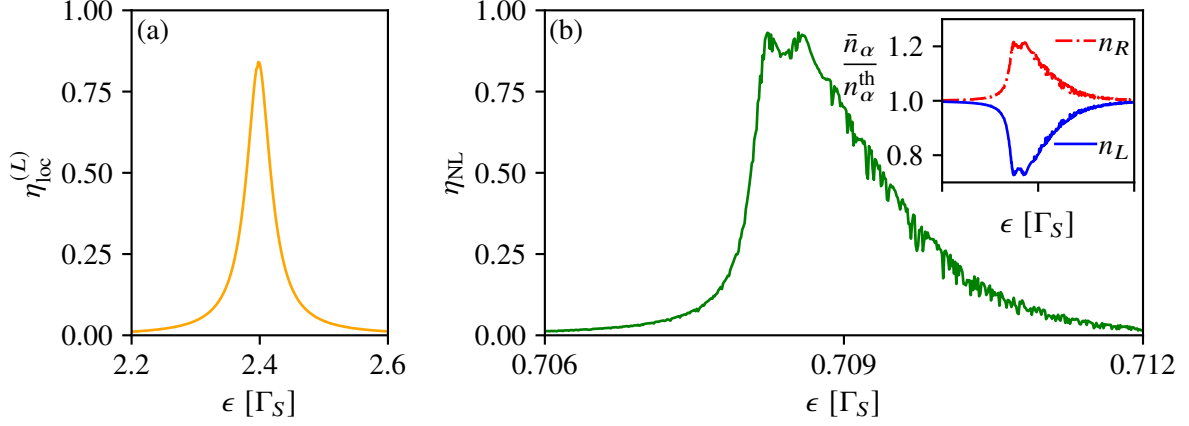


Figure 4.6: (a) Local cooling efficiency for the left cavity in the vicinity of the resonance $\bar{\delta} \approx \omega_L$. (b) Photon transfer efficiency, around $\bar{\delta} \approx \omega_L - \omega_R$. The inset shows the average cavity occupations, normalized to the thermal occupancy. The parameters are the same as in Fig. 4.5.

The efficiency is essentially limited by two factors: (i) an elastic contribution to the current (exemplified by the results of Sec. 4.3.1) where electrons flow into the leads without exchanging energy with the cavities; (ii) a finite fraction of the injected electrons acting against the dominant process (cooling or photon transfer), as illustrated by the dashed arrows in Figs. 4.4, 4.5. Both processes become relevant when Γ_S is increased, and are a byproduct of the finite hybridization between the empty and the singlet state. However, we remark that the hybridization is necessary to achieve a nonzero efficiency.

4.8 Higher-order resonances

The polaron-transformed Hamiltonian (4.21) reveals that Eqs. (4.27) and (4.28) are in fact two particular cases stemming from a more general resonance condition given by

$$\bar{\delta} \approx |p\omega_L \pm q\omega_R|, \quad (4.32)$$

where p and q are nonnegative integers. By expanding the operator Π in Eq. (4.22) up to n -th order, one obtains terms $(b_\alpha)^n$ and $(b_\alpha^\dagger)^n$, which, after moving to the interaction picture and performing a suitable rotating-wave approximation, will yield n -photon local absorption or emission processes. The expansion contains also terms of the form $(b_\alpha^\dagger)^p (b_{\bar{\alpha}})^q$ and $(b_\alpha^\dagger)^p (b_{\bar{\alpha}}^\dagger)^q$ together with their Hermitian conjugates, with the constraint $p + q = n$ ($\bar{\alpha} = R$ if $\alpha = L$ and vice versa). The former term describes the coherent transfer of $|p - q|$ photons between the cavities, while the latter describes coherent emission and re-absorption of p and q photons from the α and $\bar{\alpha}$ cavity, respectively. When either p or q is zero, the corresponding resonant process entails local cooling or heating of the cavities. An example for $p = 0$ and $q = 2$ is indicated in Fig. 4.5(b), at the resonance $\bar{\delta} = 2\omega_R$: This is a two-photon resonance at which two photons are absorbed (at $\epsilon < 0$) or lost (at $\epsilon > 0$) by the R -cavity.

4.9 Conclusions

In this Chapter, I have considered a double-quantum-dot-based CPS, with linear capacitive coupling to local resonators. The main feature of this device is the activation of a nonlocal coupling between the cavities, that allows to transfer photon and control the heat exchange between them with single-photon precision. This energy flow can also be channeled to cool or heat locally a single cavity. The origin of this indirect coupling resides in the quantum correlations in the Cooper pairs of the superconductor, which are maintained even when electrons are split into the distant quantum dots, affecting the charge-vibration interaction. As a result, this platform is a versatile tool to inspect quantum thermodynamical effects involving electronic and bosonic degrees of freedom. Because the effective interaction is at a single-photon level, one can also devise few-photon or -phonon control and manipulation techniques [134, 275, 276] by implementing time-dependent protocols on the gate voltages acting on the dots: By moving around the interesting resonances, one can tune the strength of the nonlocal interactions dynamically.

To conclude, I briefly point out the experimental practicability of the setup. The capacitive coupling $g_\alpha/2\pi$ between quantum dots and microwave resonators can be as high as 100 MHz with quality factors $Q \sim 10^4$ and frequencies $\omega_\alpha/2\pi \approx 7$ GHz [137, 277]. For mechanical resonators, the typical coupling strength is only ~ 100 kHz, but for much lower resonance frequencies in the MHz regime and larger quality factors up to 10^6 [102, 122]. The ratio $g_\alpha/\omega_\alpha \sim 10^{-2}$ assumed in the analysis above is then experimentally achievable. Finally, the magnitude of the cross-Andreev reflection rate in a CPS is approximately $\Gamma_S \lesssim \sqrt{\Gamma_{SL}\Gamma_{SR}}$, when the distance between the dots is much shorter than the coherence length in the superconducting contact. The local Andreev reflection rates $\Gamma_{S\alpha}$ can be several tens of microelectronvolts [266], which is orders of magnitude lower than the superconducting gap Δ but comparable to the energy of microwave radiation, as assumed in the calculations.

Chapter 5

Theory of double Cooper-pair tunneling and light emission mediated by a resonator

The results presented in this Chapter are published in Ref. [278]. I am responsible for the numerical calculations that led to the results of Figs. 5.2, 5.3; moreover, I have independently implemented the code written by the first author, W. T. Morley, to reproduce the results presented in Figs. 5.4, 5.5.

5.1 Introduction

The purpose of this Chapter is to present an example of how resonators coupled to mesoscopic conductors can influence dramatically the charge transport, even changing the effective charge that tunnels through. In standard mesoscopic conductors or in scanning tunneling microscopy (STM), the charge tunneling often comes together with photon emission, and this mechanism can be enhanced through the coupling to a resonator [279–284]. Conversely, it has been shown how a resonator can mediate correlated tunneling of *two* electrons across a junction, in order to generate a cavity photon at a energy higher than the single-electron one. This phenomenon is known as overbias emission [283, 285–288]. Here, I consider a solid-state device consisting of a Josephson junction (JJ) coupled to a LC-resonator, and theoretically analyze the correlated tunneling of *two* Cooper pairs across the JJ [278]. This higher-order tunneling process is enhanced and becomes resonant when the bias voltage applied to the junction is such that two Cooper pairs are required to tunnel to cooperatively emit a photon at the cavity frequency. I will present an effective Hamiltonian formulation of the problem and discuss how the double-Cooper-pair tunneling (DCPT) rate can exceed the single-Cooper-pair one. Further, I will reveal how this unconventional transport channel leads to an unusual form of photon blockade [289–292] that makes the system an ideal single-photon source [293].

5.2 Josephson junction coupled to a microwave cavity

The system considered in Ref. [278] consists of a LC-resonator of frequency $\omega_0 = 1/\sqrt{LC}$ (realized with a superconducting microwave cavity [185, 186, 284] or a lumped-element oscillator [294]) in series with

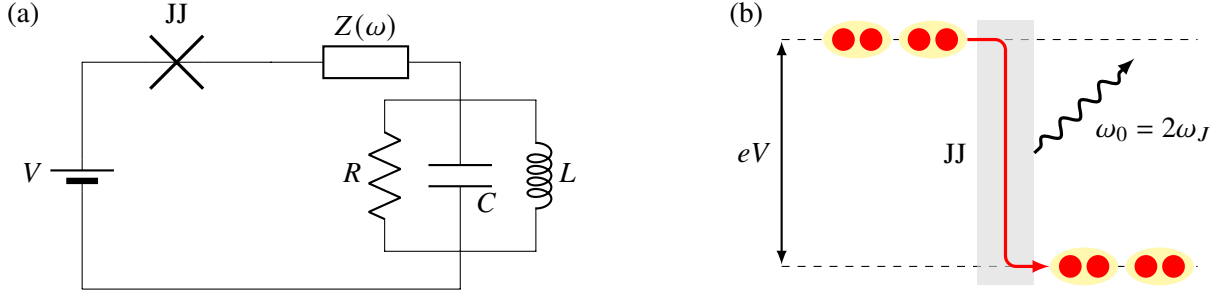


Figure 5.1: (a) Model circuit. A damped microwave resonator of frequency $\omega_0 = (LC)^{-1/2}$ is in series to a Josephson junction with applied bias voltage V . Low-frequency voltage fluctuations in the circuit may be modeled by an impedance $Z(\omega)$ in series with the junction. (b) When the bias voltage is such that $\omega_J = \omega_0/2$, photon emission in the cavity is mediated by tunneling of two Cooper pairs.

a voltage-biased Josephson junction. It is schematically pictured in Fig. 5.1(a). We assume that the resonator capacitance is much larger than the capacitance of the Josephson junction [295, 296]. The system can then be described by the following time-dependent Hamiltonian [297–299]:

$$H(t) = \omega_0 a^\dagger a - E_J \cos[\omega_J t - \phi + \Delta_0(a + a^\dagger)], \quad (5.1)$$

where a is the bosonic annihilation operator for the cavity mode, $\omega_J = 2eV$ is the Josephson frequency (V is the voltage applied to the junction and e is the electron's charge), E_J is the Josephson energy and $\Delta_0 = \sqrt{2e^2}(L/C)^{1/4}$ is the zero-point flux fluctuations amplitude of the resonator, given in units of the flux quantum. Further, we have included the phase ϕ which is conjugate to the Cooper-pair number N passing through the junction. The operator

$$e^{ip\phi} = \sum_{N=0}^{\infty} |N+p\rangle \langle N|, \quad p \in \mathbb{N}, \quad (5.2)$$

describes transfer of p Cooper pairs across the junction. The value of Δ_0 is determined by the impedance of the resonator, and can range from $\Delta_0 \ll 1$ [185, 186, 284] to values close to unity [294].

Losses in the resonator due to the resistance give rise to a quality factor $Q = \omega_0/\kappa$, with κ the decay rate. The presence of low-frequency impedances in the circuit causes voltage fluctuations that dephase the charge on the junction, with rate γ_ϕ [300]. These decoherence effects can be described by a standard Lindblad master equation [297]

$$\dot{\rho} = -i[H(t), \rho] + \frac{\kappa}{2} \mathcal{D}[a]\rho + \frac{\gamma_\phi}{2} \mathcal{D}[N]\rho, \quad (5.3)$$

where we have assumed the limit of low temperature. Typically, $\gamma_\phi \ll \kappa$, hence the phase ϕ can be treated as constant neglecting the dephasing term [295, 300].

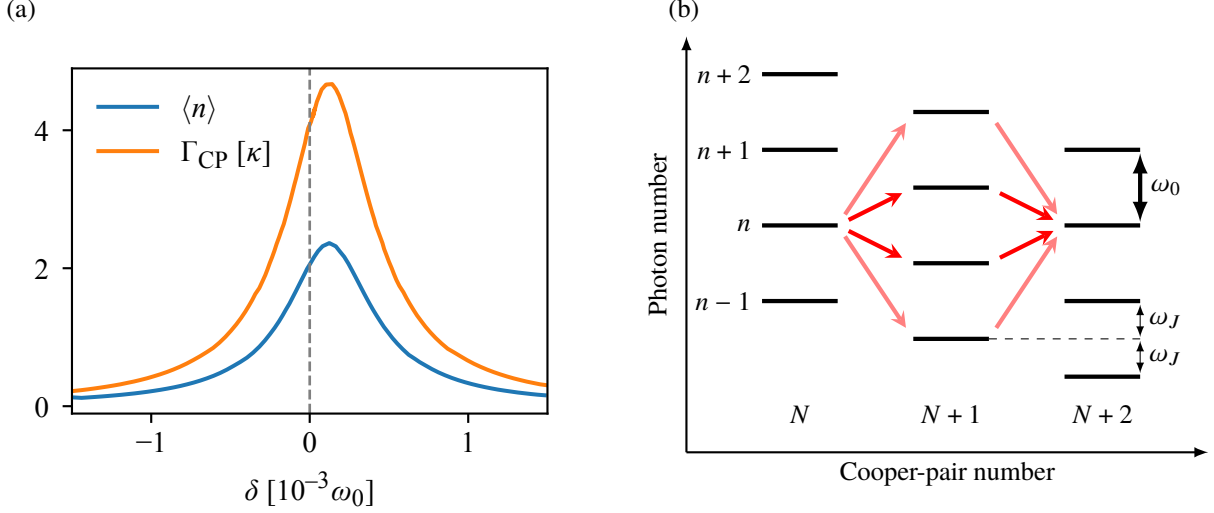


Figure 5.2: (a) Time-averaged cavity photon number (solid blue line) and Cooper-pair tunneling rate (solid orange line) as a function of $\delta = \omega_0 - 2\omega_J$, calculated using the full Hamiltonian (5.1) and the master equation (5.3). Parameters: $\Delta_0 = 0.15$, $Q = 1500$, $E_J = 0.5\omega_0$, $\gamma_\phi = 0$. Notice that, close to the resonance, $\frac{\Gamma_{\text{CP}}}{\kappa \langle n \rangle} \approx 2$, i.e., two Cooper pairs tunnel for each emitted photon. (b) Schematic diagram of the energy levels for n cavity photons and N tunneling Cooper pairs, at the resonance $2\omega_J \approx \omega_0$, illustrating a few effective second-order processes included in the effective Hamiltonian (5.6).

5.3 Effective Hamiltonian description

The study of photon emission and tunneling of individual Cooper pairs across a voltage-biased JJ has been extensively investigated, both in theory [295, 297, 299, 301–310] and experiment [185, 186, 284, 293, 294, 311, 312], and it is resonantly enhanced when the Josephson frequency ω_J matches the resonator frequency ω_0 . The goal of this Section is instead to derive an effective Hamiltonian for the system, by considering the resonance $\omega_0 \approx 2\omega_J$. As Fig. 5.1(b) illustrates, for an applied bias voltage $V = \frac{\omega_0}{4e}$ to the junction, two Cooper pairs are expected to contribute to the emission of a single photon at frequency ω_0 . We then take Hamiltonian Eq. (5.1) and move to a frame rotating at frequency $2\omega_J$, obtaining

$$\tilde{H} = \delta a^\dagger a - \frac{\tilde{E}_J}{2} \sum_{q=0}^{\infty} [O_q e^{i(2q+1)\omega_J t} + \text{H.c.}], \quad (5.4)$$

with the detuning $\delta = \omega_0 - 2\omega_J$. We have defined the rescaled Josephson energy $\tilde{E}_J = E_J e^{-\Delta_0^2/2}$ and the operator

$$O_q = : i^q (a^\dagger)^{q+1} e^{-i\phi} \frac{J_q(2\Delta_0 \sqrt{n})}{n^{q/2}} + (-i)^{q+1} (a^\dagger)^{(q+1)} e^{i\phi} \frac{J_{q+1}(2\Delta_0 \sqrt{n})}{n^{(q+1)/2}} :. \quad (5.5)$$

Here, $J_q(z)$ denotes the Bessel function of order q , $n = a^\dagger a$ is the photon number operator, and $: \dots :$ implies normal ordering of the operators. The next step in the derivation consists in performing a second-order rotating-wave approximation to Hamiltonian (5.4), in order to obtain an effective time-independent operator [313, 314]. By averaging the operator over short time scales of order ω_J^{-1} we obtain

$$H_{\text{eff}} = \delta a^\dagger a + \frac{\tilde{E}_J^2}{4\omega_J} \sum_{q=0}^{\infty} \frac{[O_q, O_q^\dagger]}{2q+1} = \left(\delta + \frac{\tilde{E}_J^2 \mathcal{G}}{4\omega_J} \right) n - i \frac{\tilde{E}_J^2}{4\omega_J} [\mathcal{F} a^\dagger e^{2i\phi} - \text{H.c.}]. \quad (5.6)$$

We have introduced two highly nonlinear functions of Δ_0 and of the number operator, namely $\mathcal{F}(\Delta_0, n)$ and $\mathcal{G}(\Delta_0, n)$. In Appendix D we provide their explicit expressions, and we describe their matrix elements in the Fock state basis.

The effective Hamiltonian (5.6) provides an insight on the relevant physical processes that we want to address. The first nonlinear term describes a shift in the resonator frequency [296] which can be observed, e.g., by computing the average photon number in the cavity and the Cooper-pair tunneling rate (see below, Sec. 5.5), as is reported in Fig. 5.2(a). Similarly to the ac-Stark effect in atomic levels [313, 314], this frequency shift is due to the presence of a strong off-resonant drive (at frequency ω_J). However, the nonlinearity of $\mathcal{G}(\Delta_0, n)$ also up-converts the off-resonant drive into the resonant process of DCPT. Indeed, the factor $a^\dagger e^{2i\phi}$ in the second term of Hamiltonian (5.6) describes a coherent process in which a photon is created in the cavity, and two Cooper pairs tunnel through the junction [see Eq. (5.2)]. To visualize this second-order process, which is realized through intermediate virtual levels, a diagram of the energy levels involved is provided in Fig. 5.2(b).

When both Δ_0 and the average photon number $\langle n \rangle$ are much smaller than 1, an expansion of Eq. (5.6) to lowest order in Δ_0 yields the following effective Hamiltonian:

$$H_{\text{eff}}^{(0)} = \delta' n + i \frac{\tilde{E}_J^2 \Delta_0^3}{3\omega_J} [a e^{-2i\phi} - a^\dagger e^{2i\phi}], \quad (5.7)$$

with the linearized frequency shift

$$\delta' = \delta + \frac{8\tilde{E}_J^2 \Delta_0^4}{15\omega_J}. \quad (5.8)$$

Equations (5.6) and (5.7), together with the master equation (5.3), can be used to compare the effective Hamiltonian description to the numerical results obtained by time-averaging the expectation values in the long-time limit using the full time-dependent Hamiltonian $H(t)$ of Eq. (5.1).

5.4 Results for the average photon number

Armed with the effective Hamiltonian description, we first analyze the photonic properties on the system in the low-photon-number limit described by Eq. (5.7). With the master equation (5.3) we write the equations of motion

$$\frac{d}{dt} \langle a \rangle = - \left(i\delta' + \frac{\kappa}{2} \right) \langle a \rangle - X \langle e^{2i\phi} \rangle, \quad (5.9)$$

$$\frac{d}{dt} \langle e^{2i\phi} \rangle = -2\gamma_\phi \langle e^{2i\phi} \rangle, \quad (5.10)$$

with $X = \frac{\bar{E}_J^2 \Delta_0^3}{3\omega_J}$. With the help of the quantum regression theorem [157] we obtain

$$\langle a^\dagger(t) e^{2i\phi}(t+\tau) \rangle = \langle a^\dagger(t) e^{2i\phi}(t) \rangle e^{-2\gamma_\phi \tau}, \quad (5.11)$$

$$\langle a^\dagger(t) a(t+\tau) \rangle = \langle a^\dagger(t) a(t) \rangle e^{-(\kappa/2 + i\delta')\tau} - X \frac{\langle a^\dagger(t) e^{2i\phi}(t) \rangle}{\frac{\kappa}{2} - 2\gamma_\phi + i\delta'} \left(e^{-2\gamma_\phi \tau} - e^{-(\kappa/2 + i\delta')\tau} \right). \quad (5.12)$$

For $t \rightarrow \infty$, we get the steady-state values

$$\langle n \rangle = \langle a^\dagger a \rangle = \frac{X^2 \left(1 + \frac{4\gamma_\phi}{\kappa} \right)}{\frac{\kappa^2}{4} \left(1 + \frac{4\gamma_\phi}{\kappa} \right)^2 + (\delta')^2}, \quad (5.13)$$

$$\langle a^\dagger e^{2i\phi} \rangle = \frac{-X}{\frac{\kappa}{2} + 2\gamma_\phi - i\delta'}. \quad (5.14)$$

Plugging Eqs. (5.13)-(5.14) into Eq. (5.12) leads to the first-order coherence function for the field:

$$\langle a^\dagger a(\tau) \rangle = \langle n \rangle e^{-(i\delta' + \kappa/2)\tau} + \frac{X^2 \left(e^{-2\gamma_\phi \tau} - e^{-(i\delta' + \kappa/2)\tau} \right)}{\left[i\delta' + \left(\frac{\kappa}{2} - 2\gamma_\phi \right) \right] \left[-i\delta' + \left(\frac{\kappa}{2} + 2\gamma_\phi \right) \right]}, \quad (5.15)$$

which in the low-dephasing limit ($\gamma_\phi \ll \kappa$) simplifies to

$$\langle a^\dagger a(\tau) \rangle \approx \langle n \rangle e^{-2\gamma_\phi \tau}. \quad (5.16)$$

Equation (5.16) shows that the first-order coherence function decays at a rate $2\gamma_\phi$, meaning that the resonator linewidth is four times larger than for the single-Cooper-pair resonance $\omega_J \approx \omega_0$ [297]. Hence, signatures of DCPT can be easily found by looking at the resonator spectrum. The average cavity occupation in Eq. (5.13) shows a lowest-order E_J^4 -dependence and is instead only weakly dependent on γ_ϕ . In the following, we set $\gamma_\phi = 0$ as voltage fluctuations can be negligible in experiments [284, 297, 300].

In Fig. 5.3 (upper panel) we solve numerically [208, 315] the Lindblad equation Eq. (5.3) with the full Hamiltonian (5.1) and compare the average cavity occupation with the effective Hamiltonian (5.6). It is apparent that the E_J^4 -scaling is valid only at intermediate values: At higher values of E_J , the lowest-order Hamiltonian $H_{\text{eff}}^{(0)}$ is insufficient, and one must take into account the higher-order contributions described by Eq. (5.6), while the nonlinear components from the $\mathcal{F}(\Delta_0, n)$ and $\mathcal{G}(\Delta_0, n)$ functions lead to a saturation of the photon number. At the same time, H_{eff} is also not valid at very low E_J : It describes adequately the resonant process at $2\omega_J \approx \omega_0$, but the dominant process at low E_J is the single-Cooper-pair tunneling oscillating at the Josephson frequency ω_J .

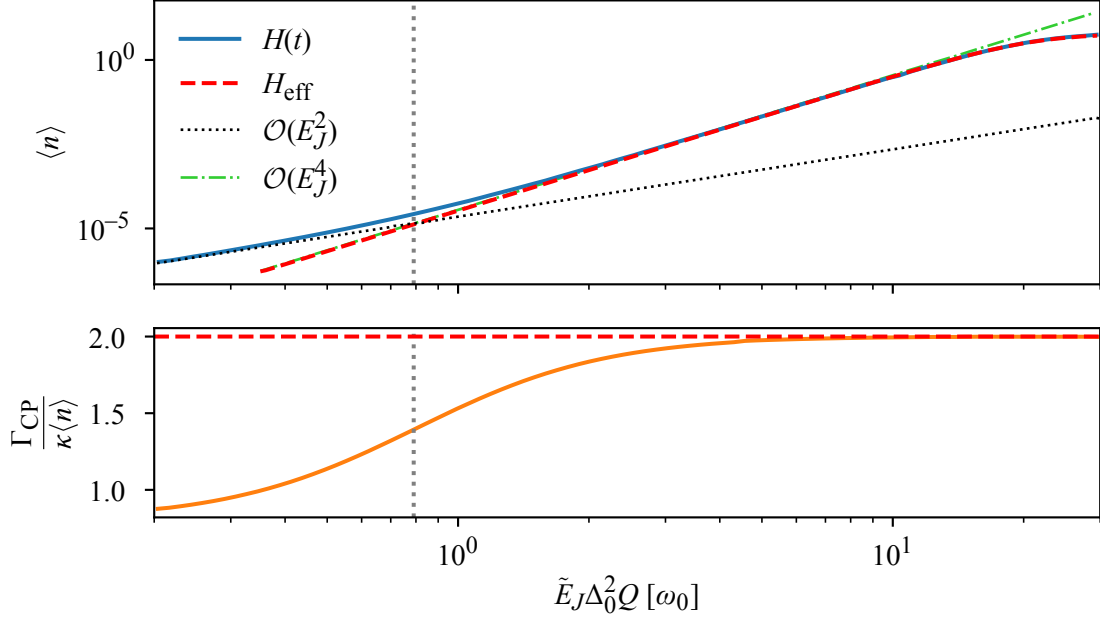


Figure 5.3: Upper panel: time-averaged cavity occupation calculated with the full Hamiltonian (5.1) (solid blue line), and with H_{eff} (dashed red line). The semiclassical analysis at low E_J gives the quadratic and quartic contributions (black dotted and green dash-dotted lines, respectively). The crossover from single- to double-Cooper pair tunneling occurs for $\tilde{E}_J \Delta_0^2 Q / \omega_0 = \sqrt{5}/8$ (vertical dotted line). Lower panel: ratio between Cooper-pair tunneling rate and average photon number, calculated using Eq. (5.23). The effective-Hamiltonian prediction taken with Eq. (5.26) gives exactly 2 (red dashed line). Parameters in both panels are: $\omega_J = \omega_0/2$, $Q = 1500$, $\Delta_0 = 0.15$, $\gamma_\phi = 0$.

5.4.1 Semiclassical interpretation

For $\gamma_\phi = 0$, the system can be mapped onto a nonlinearly driven harmonic oscillator [295, 296, 316]. At low- E_J , we can write semiclassical equations of motion for the resonator to better understand the competition between the E_J^2 and E_J^4 behaviors. In the limit $\gamma_\phi \rightarrow 0$, setting $\phi = 0$ without loss of generality, and assuming that the resonator is in a coherent state $|\alpha\rangle$, we arrive at the equation of motion

$$\frac{d\alpha}{dt} = -\left(i\omega_0 + \frac{\kappa}{2}\right)\alpha - i\tilde{E}_J \Delta_0 \sin[\omega_J t + \Delta_0(\alpha + \alpha^*)]. \quad (5.17)$$

Close to the resonance $2\omega_J \approx \omega_0$ and for very small E_J , the resonator is off-resonantly driven at two frequencies $\pm\omega_J$, and in the long-time limit $\alpha \approx \alpha_- e^{-i\omega_J t} + \alpha_+ e^{i\omega_J t}$, with the constants α_\pm . When E_J gets larger, however, nonlinearities come into play and the oscillations will be up-converted into an effective drive at frequency $2\omega_J$. We thus make the ansatz of a solution of the kind

$$\alpha = \alpha_0 e^{-2i\omega_J t} + \alpha_- e^{-i\omega_J t} + \alpha_+ e^{i\omega_J t}, \quad (5.18)$$

leading to:

$$\alpha_0 = -i \frac{\tilde{E}_J \Delta_0^2}{2} \frac{\alpha_- + \alpha_+^*}{i(\omega_0 - 2\omega_J) + \frac{\kappa}{2}}, \quad (5.19)$$

$$\alpha_- = \frac{\tilde{E}_J \Delta_0}{2} \frac{1 - i\Delta_0 \alpha_0}{i(\omega_0 - \omega_J) + \frac{\kappa}{2}}, \quad (5.20)$$

$$\alpha_+ = -\frac{\tilde{E}_J \Delta_0}{2} \frac{1 + i\Delta_0 \alpha_0^*}{i(\omega_0 + \omega_J) + \frac{\kappa}{2}}. \quad (5.21)$$

Setting $\omega_J \approx \omega_0/2$, and since $\kappa \ll \omega_J$, we can write an expression for the average photon number to fourth order in E_J :

$$\overline{\langle n \rangle} = |\alpha_0|^2 + |\alpha_+|^2 + |\alpha_-|^2 \approx \frac{\tilde{E}_J^2 \Delta_0^2}{2} \left[\frac{\omega_0^2 + \omega_J^2}{(\omega_0^2 - \omega_J^2)^2} \right] \left\{ 1 + \frac{\tilde{E}_J^2 \Delta_0^4}{2} \frac{\omega_0^2}{[\omega_0^2 + \omega_J^2] \left[(\omega_0 - 2\omega_J)^2 + \frac{\kappa^2}{4} \right]} \right\}. \quad (5.22)$$

The bar over n implies a time average. It is clear that the $\pm\omega_J$ oscillations give a $\tilde{E}_J^2 \Delta_0^2$ contribution, while the $2\omega_J$ oscillations give a $\tilde{E}_J^2 \Delta_0^6$ contribution. Both are plotted as $O(E_J^2)$ and $O(E_J^4)$ in the upper panel of Fig. 5.3. The two contributions have the same weight for $\tilde{E}_J \Delta_0^2 Q = \sqrt{5/8} \omega_0$.

5.5 Analysis of the charge transport

5.5.1 Average current and Cooper-pair tunneling rate

We now turn to a quantitative description of the Cooper-pair transport across the junction. To begin with, we notice that the dissipative terms in the master equation (5.3) do not contribute to charge transfer, and is therefore possible to define a Cooper-pair current operator simply as [297, 316]

$$I_{\text{CP}}(t) = 2e \frac{dN}{dt} = 2ie[H(t), N] = 2eE_J \sin[\omega_J t - \phi + \Delta_0(a + a^\dagger)]. \quad (5.23)$$

Averaging over a time $T \gg \omega_J^{-1}$ yields an average dc-current operator

$$\bar{I}_{\text{CP}} = \frac{1}{T} \int_{t_0}^{t_0+T} dt I_{\text{CP}}(t), \quad (5.24)$$

which leads to the definition of an effective, average Cooper-pair tunneling rate

$$\Gamma_{\text{CP}} = \frac{\bar{I}_{\text{CP}}}{2e}. \quad (5.25)$$

The effective Hamiltonian (5.6) offers a direct, alternative definition of the average current as

$$\bar{I}_{\text{CP}} = 2ie[H_{\text{eff}}, N]. \quad (5.26)$$

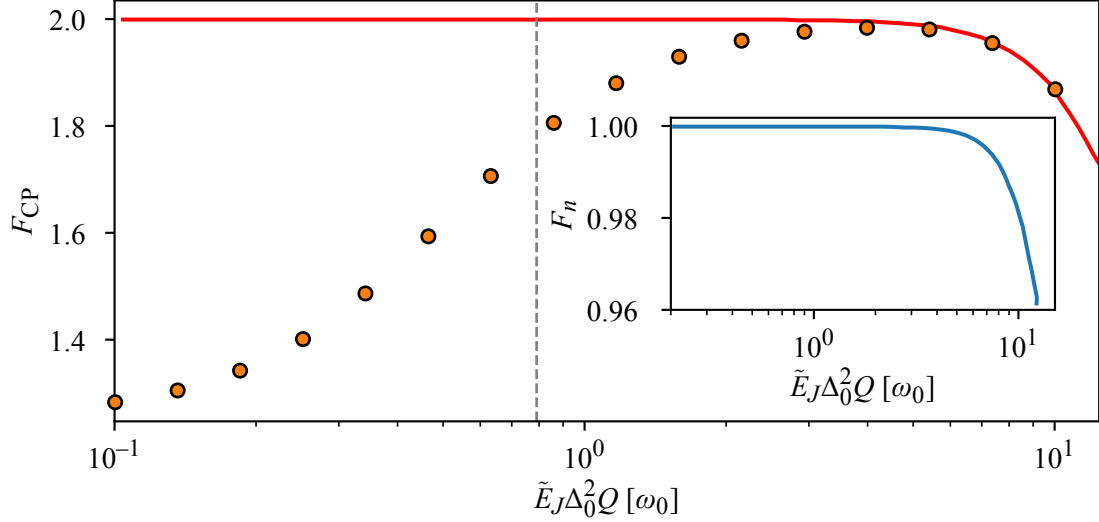


Figure 5.4: Current Fano factor as a function of E_J . The solid red line is obtained with H_{eff} , while the orange dots are calculated with the full Hamiltonian (5.1) and the current noise Eq. (5.28). The dashed gray line marks the semiclassical crossover at $\tilde{E}_J \Delta_0^2 Q = \sqrt{5/8} \omega_0$. Inset: Fano factor of the resonator number, using the effective Hamiltonian H_{eff} . Parameters are the same as in Fig. 5.3.

Using the master equation (5.3), Eq. (5.26) predicts, in the steady state, the remarkably simple relation

$$\frac{\Gamma_{\text{CP}}}{\kappa \langle n \rangle} = 2. \quad (5.27)$$

Equation (5.27) has a likewise simple interpretation: The effective Hamiltonian describes a resonator oscillating at the frequency $2\omega_J$, and photons are generated and destroyed only when two Cooper pairs tunnel. Accordingly, the lower panel of Fig. 5.3 shows how Eq. (5.27) is in agreement with the full-Hamiltonian calculation at sufficiently large E_J . For low E_J , oscillations at the Josephson frequency cannot be neglected, and Γ_{CP} drops below 2 as the single-Cooper-pair tunneling contribution grows.

5.5.2 From incoherent to coherent double-Cooper-pair tunneling

Next, we characterize the transport statistics by defining the time-averaged current noise [214]:

$$S_{\text{CP}} = 2\text{Re} \int_0^\infty d\tau \int_{t_0}^{t_0+T} \frac{dt}{T} [\langle I_{\text{CP}}(t+\tau) I_{\text{CP}}(t) \rangle - \langle I_{\text{CP}}(t+\tau) \rangle \langle I_{\text{CP}}(t) \rangle]. \quad (5.28)$$

We also define the current Fano factor

$$F_{\text{CP}} = \frac{S_{\text{CP}}}{2e \langle \bar{I}_{\text{CP}} \rangle}, \quad (5.29)$$

which relates the fluctuations in the current to the noise of a Poissonian process of single-Cooper-pair tunneling [316]. In Fig. 5.4, we plot the Fano factor using both definitions of Eqs. (5.24) and (5.26) in Eq. (5.29). For small E_J , using the effective Hamiltonian, $F_{\text{CP}} \approx 2$, meaning that *incoherent* DCPT takes place (i.e., an effective charge $4e$ is transferred) [317]. At larger E_J , the value of F_{CP} drops, and since $\Gamma_{\text{CP}}/\kappa \langle n \rangle \approx 2$ in this regime (see Fig. 5.3), this implies that DCPT is *coherent* [318]. In the inset of

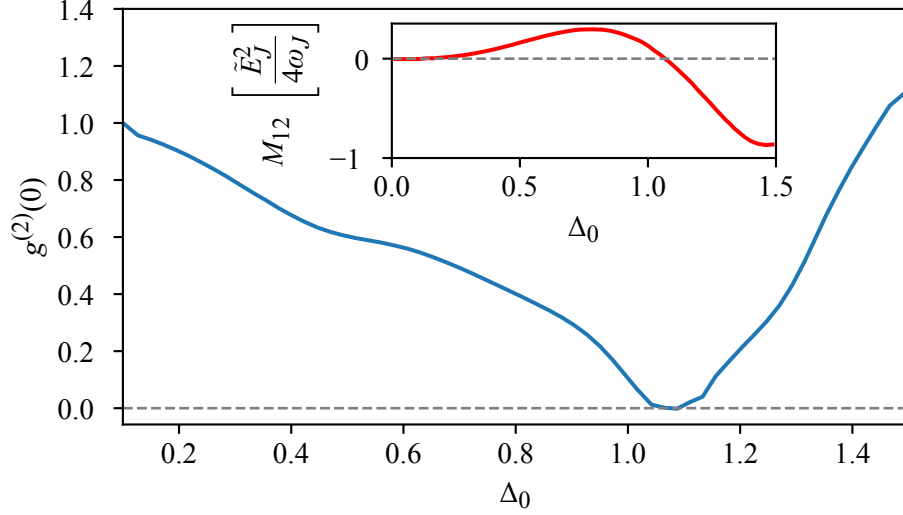


Figure 5.5: Second-order correlation function of the cavity field, calculated using Eqs. (5.6) and (5.31), as a function of the zero-point amplitude Δ_0 . The inset shows the behavior of the matrix element $M_{12} = |\langle 1|H_{\text{eff}}|2\rangle|$. The parameters used are: $\tilde{E}_J = 0.1\omega_0$, $\omega_J = \omega_0/2$, $Q = 500$, $\gamma_\phi = 0$.

Fig. 5.4 we also consider the cavity Fano factor, $F_n = (\langle n^2 \rangle - \langle n \rangle^2) / \langle n \rangle$, which drops below 1 witnessing a sub-Poissonian photon emission statistics. This mechanism is in close analogy to the crossover between incoherent and coherent *single*-Cooper-pair tunneling occurring when $\omega_J \approx \omega_0$ [297, 316]. The orange dots in Fig. 5.4 calculated using Eq. (5.28) show that F_{CP} drops below 2 at small E_J , again because of single-Cooper-pair tunneling contributions.

By considering the validity regime of Eq. (5.7) we can pinpoint the parameter region dominated by incoherent DCPT, where $F_{\text{CP}} \approx 2$: the lower limit is determined by the crossover from the E_J^2 and the E_J^4 behaviour, at $\tilde{E}_J \Delta_0^2 Q \approx \sqrt{5/8} \omega_0$, while the upper limit is fixed by the onset of strong nonlinearities, when $\langle n \rangle \approx (4\Delta_0^2)^{-1}$. Therefore, incoherent behaviour dominates for

$$\sqrt{\frac{5}{8}} \ll \frac{\tilde{E}_J \Delta_0^2 Q}{\omega_0} \ll \sqrt{\frac{3Q}{8}}, \quad (5.30)$$

indicating that a high- Q resonator is required to discern this regime from other transport mechanism.

5.6 Photon blockade and single-photon emission

For large resonator impedance, zero-point flux fluctuations become large and Δ_0 can approach unity [294]. In this regime, the light emission from the resonator becomes strongly nonclassical, and its properties can be investigated by looking at the second-order field correlation function defined as [6]

$$g^{(2)}(0) = \frac{\langle a^\dagger a^\dagger a a \rangle}{\langle a^\dagger a \rangle^2}, \quad (5.31)$$

where the average is performed on the state of the oscillator in the long-time limit. When $g^{(2)}(0) \ll 1$, the photon-emission statistics is strongly sub-Poissonian: photons are preferably emitted singularly and the resonator can function as a single-photon source. This mechanism is in close relation to the photon

blockade of cQED experiments, which arises from the anharmonic spectrum of the coupled light-matter Hamiltonian [289–292, 294, 319].

In Fig. 5.5, we report the behavior of $g^{(2)}(0)$ as a function of Δ_0 . The value of the correlation function is close to zero for $\Delta_0 \approx 1.07$, indicating a strong photon blockade leading to single-photon emission. It is possible to interpret this result in terms of the effective Hamiltonian of Eq. (5.6). Specifically, as shown in Appendix D, the matrix element $\langle 1|H_{\text{eff}}|2\rangle$ can be calculated analytically in closed form. When it vanishes, the resonator remains trapped in the two-state basis spanned by the Fock states $|0\rangle$ and $|1\rangle$ and further photon emission is blocked. Consequently, the photon-photon correlation function drops to zero. In the inset of Fig. 5.5, we show that the matrix element M_{12} has indeed a zero for $\Delta_0 \approx 1.07$, corresponding to the minimum of $g^{(2)}(0)$. The presence of vanishing matrix elements of H_{eff} in the Fock basis witnesses a destructive interference of many processes, each contributing to the photon-blockade effect. It is worth noticing here that the value $\Delta_0 \approx 1.07$ is significantly lower than the matrix-element zero corresponding to the single-Cooper-pair tunneling resonance ($\omega_J \approx \omega_0$), occurring for $\Delta_0 = \sqrt{2}$ [297, 307] and only slightly higher than the experimentally achieved value [294].

5.7 Conclusions

In this Chapter, I have analyzed the emergence of double-Cooper-pair tunneling in a voltage-biased Josephson junction, when it is coupled to a microwave resonator: When the Josephson frequency is half the resonator frequency, two Cooper pairs are required to emit a photon at the cavity frequency. By developing an effective Hamiltonian theory and performing numerical simulations, I have shown a crossover from incoherent to coherent double-Cooper-pair tunneling when increasing the Josephson energy E_J . Despite being higher-order processes in both the Josephson energy and the resonator impedance, this remarkable transport regime is readily accessible in experiment, as both quantities can be tuned beyond the perturbative regime (both $E_J \gtrsim \omega_0$ [185] and $\Delta_0 \approx 1$ [294] have been reached experimentally).

When the impedance resonator becomes large, the single-photon nonlinearity in the spectrum leads to a photon blockade mechanism which can be exploited to use this system as a single-photon source. This is readily verified by computing second-order photon correlation functions for the cavity. Beyond this practical advantage, the results presented here will stimulate experimental and theoretical investigation of hitherto unexplored higher-order tunneling processes in JJ-resonator systems, and overbias photon emission mechanisms in superconducting STM [320].

Chapter 6

Conclusions and outlook

In this work, I have presented different hybrid quantum circuits composed of quantum dots or Josephson junctions coupled to electromagnetic or mechanical cavities. These ensembles offer an extremely rich and diverse physics, which goes beyond the standard light-matter interaction originally studied in cavity QED, using real atoms and optical or microwave cavities. Indeed, quantum dots and superconducting qubits are exceptionally versatile and tunable, allowing to carefully design a solid-state chip where interactions and energy-exchange mechanisms can be controlled.

The first system I considered is a realization of a single-atom laser which takes advantage of a spin-polarized current to pump energy with high efficiency into a resonator, such that the standard rotating-wave approximation (RWA) for the model Hamiltonian no longer holds even at weak couplings. After numerical solution of the full master equation, I have interpreted the unconventional results for the state of the resonator within a semiclassical picture, showing that the RWA breakdown, induced by a strongly nonlinear interaction between electron spin and cavity, leads to a multistable lasing regime where multiple stable amplitudes of oscillation can coexist. I have further shown that these remarkable features can be detected through simple monitoring of the electric current in real time, without resorting to more complicated techniques involving optical detection or tomography of the cavity state. The described model carries important theoretical results, as it provides a way to investigate coherent dynamics beyond the RWA outside the ultrastrong coupling regime. From a more practical point of view, our work raises interesting questions about the extent to which a multistable laser can be controlled and exploited, e.g., in nonlinear amplifiers or force-sensing devices.

Secondly, I discussed a device consisting of a quantum-dot-based Cooper-pair splitter (CPS) with local capacitive coupling to two harmonic cavities. Here, I have shown that the Cooper-pair breaking from a central superconductor induces nonlocal correlations in the two resonators. More specifically, by tuning the gate voltages controlling the electrostatic energy of the dots, photons can be transferred efficiently from one cavity to the other, establishing a steady nonequilibrium heat flow. Such energy flow can further be channeled to cool down one or both cavities into their ground state, enabling few-photon (or few-phonon) coherent manipulation. The proposed setup is therefore a versatile tool to fully inspect heat exchange mechanisms in hybrid circuits, leading to nanoscale heat pumps and cooling devices.

Finally, in a third work, I have investigated the double-Cooper pair tunneling mechanism in a Josephson junction coupled to a microwave LC-resonator. By deriving an effective Hamiltonian description for the

circuit when the Josephson frequency is half of the resonator frequency, it is possible to distinguish two regimes where the transport across the junction and the photon emission from the cavity are determined by tunneling of two Cooper pairs: an incoherent regime, when double-Cooper pair transport first begins to dominate, and a coherent regime emerging at larger Josephson frequencies. Furthermore, by examining the second-order correlation functions for the emitted photons, it is possible to show that the system displays an unusual form of photon blockade and therefore can be used as a single-photon source. The system considered can be used as a testbed to explore how microwave resonators can control electron transport and has potential implications in the study of overbias photon emission in superconducting scanning tunneling microscopy.

The above discussion demonstrates how hybrid systems are a powerful tool to explore novel regimes of interactions, or to gain deeper knowledge on the mechanisms underlying the standard QED architectures. Besides, they offer a practical advantage as they can be integrated into several architectures such as cooling devices, detectors, sensors and quantum computers. The rich physics of the systems presented requires a more profound analysis: Future research directions might focus on a closer investigation of the single-atom lasing regime attainable using quantum dots. Specifically, the increasing experimental effort towards the realization of a controllable strong spin-photon and spin-vibration coupling can be strengthened and stimulated by our work of Ref. 168. Alternative implementations can be constructed using multiple quantum dots, or exploiting a thermal gradient between two normal-metal electrodes comprising a double quantum dot. The latter represents a mesoscopic single-emitter quantum heat engine, which can attract the interest of the quantum thermodynamics community. From a theoretical point of view, an accurate description of the phase diffusion dynamics for this type of single-atom laser can be significant. The CPS device presented in Ref. 227 might be further investigated including time-dependent protocols controlling the gate voltages applied to the dots, which can in turn fine-tune the coherent photon transfer between the cavities to generate entanglement and perform quantum state engineering. Moreover, coupling CPSs to microwave cavities is essential to demonstrate the coherence of Cooper-pair injection, due to coherent cross-Andreev reflection, through microwave spectroscopy [321, 322].

Appendix A

Complements to the derivation of the master equation

I clarify here a few assumptions made throughout the derivation of the master equation outlined in Ch 2.

A.1 Hermiticity of the interaction operators

In Sec. 2.2.2, I have argued that the hermiticity of operators A_α and B_α making up the interaction Hamiltonian H_I does not affect the generality of the results. It is sufficient that the resulting H_I is hermitian. Indeed, if A_α and B_α are not hermitian but $H_I = H_I^\dagger$, we must conclude that H_I contains operators A_α and B_α as well as their hermitian conjugates. It is then possible to construct linear combinations of A_α, B_α and $A_\alpha^\dagger, B_\alpha^\dagger$ such that we can write $H_\alpha = \sum_\alpha \tilde{A}_\alpha \otimes \tilde{B}_\alpha$, with $\tilde{A}_\alpha = \tilde{A}_\alpha^\dagger$ and $\tilde{B}_\alpha = \tilde{B}_\alpha^\dagger$.

As a simple example, given the hermitian Hamiltonian

$$H_I = A \otimes B^\dagger + A^\dagger \otimes B, \quad (\text{A.1})$$

with A and B nonhermitian, it is sufficient to define the hermitian operators

$$\begin{aligned} \tilde{A}_1 &= \frac{1}{\sqrt{2}}(A + A^\dagger), & \tilde{B}_1 &= \frac{1}{\sqrt{2}}(B + B^\dagger), \\ \tilde{A}_2 &= \frac{i}{\sqrt{2}}(A - A^\dagger), & \tilde{B}_2 &= \frac{i}{\sqrt{2}}(B - B^\dagger), \end{aligned} \quad (\text{A.2})$$

through which one has $H_I = \sum_{i=1}^2 \tilde{A}_i \otimes \tilde{B}_i$.

A.2 Vanishing expectation values of single operator

Here, we show that it is always possible to construct an Hamiltonian that satisfies Eq. (2.19). It is sufficient to rewrite

$$H'_I = \sum_{\alpha} A_{\alpha} \otimes (B_{\alpha} - \langle B_{\alpha} \rangle_E) = H_I - \sum_{\alpha} A_{\alpha} \otimes (\langle B_{\alpha} \rangle_E \mathbb{1}), \quad (\text{A.3})$$

where $\langle B_{\alpha} \rangle_E = \text{Tr}_E\{B_{\alpha}\rho_E\}$. It is easy to check that $\langle H'_I \rangle_E = 0$. One can then reabsorb this term through a shift in the energy of the system Hamiltonian, since

$$\begin{aligned} H_I &= H_S \otimes \mathbb{1}_E + \mathbb{1}_E \otimes H_E + H_I \\ &= H_S \otimes \mathbb{1}_E + \mathbb{1}_E \otimes H_E + H'_I + \sum_{\alpha} A_{\alpha} \otimes (\langle B_{\alpha} \rangle_E \mathbb{1}) \\ &= \left(H_S + \sum_{\alpha} \langle B_{\alpha} \rangle_E A_{\alpha} \right) \otimes \mathbb{1}_E + \mathbb{1}_E \otimes H_E + H'_I. \end{aligned} \quad (\text{A.4})$$

Appendix B

Steady-state Fock distribution for the resonator in RWA

In this Appendix, I derive the analytical expression in RWA for the steady-state Fock distribution p_n of the harmonic oscillator in the single-atom laser setup (see Ch. 3), in the fully polarized case case ($P = 1$), and at resonance ($\Delta\epsilon = \omega_0$). I further assume $\Gamma_L = \Gamma_R = \Gamma$. The derivation follows the seminal works of Scully and Lamb [6, 172]. Starting from the master equation (3.8), I label the matrix elements of ρ as $\rho_{ss'}^{nn'}$, with the upper index referring to the oscillator states and the lower index referring to the quantum dot states ($s, s' \in \{0, \downarrow, \uparrow\}$). The three equations for the diagonal dot part of the density matrix read

$$\begin{aligned} \dot{\rho}_{\uparrow\uparrow}^{nn'} = & -ig \left(\sqrt{n+1} \rho_{\downarrow\uparrow}^{n+1,n'} - \sqrt{n'+1} \rho_{\uparrow\downarrow}^{n,n'+1} \right) \\ & + \frac{\kappa}{2} (1 + n_B) \left(2\sqrt{(n+1)(n'+1)} \rho_{\uparrow\uparrow}^{n+1,n'+1} - (n+n') \rho_{\uparrow\uparrow}^{nn'} \right) \\ & + \frac{\kappa}{2} n_B \left(2\sqrt{nn'} \rho_{\uparrow\uparrow}^{n-1,n'-1} - (n+n'+2) \rho_{\uparrow\uparrow}^{nn'} \right) \\ & + \Gamma \rho_{00}^{nn'}, \end{aligned} \quad (\text{B.1})$$

$$\begin{aligned} \dot{\rho}_{\downarrow\downarrow}^{nn'} = & -ig \left(\sqrt{n} \rho_{\uparrow\downarrow}^{n-1,n'} - \sqrt{n'} \rho_{\downarrow\uparrow}^{n,n'-1} \right) \\ & + \frac{\kappa}{2} (1 + n_B) \left(2\sqrt{(n+1)(n'+1)} \rho_{\downarrow\downarrow}^{n+1,n'+1} - (n+n') \rho_{\downarrow\downarrow}^{nn'} \right) \\ & + \frac{\kappa}{2} n_B \left(2\sqrt{nn'} \rho_{\downarrow\downarrow}^{n-1,n'-1} - (n+n'+2) \rho_{\downarrow\downarrow}^{nn'} \right) \\ & - \Gamma \rho_{\downarrow\downarrow}^{nn'}, \end{aligned} \quad (\text{B.2})$$

$$\begin{aligned} \dot{\rho}_{00}^{nn'} = & \frac{\kappa}{2} (1 + n_B) \left(2\sqrt{(n+1)(n'+1)} \rho_{00}^{n+1,n'+1} - (n+n') \rho_{00}^{nn'} \right) \\ & + \frac{\kappa}{2} n_B \left(2\sqrt{nn'} \rho_{00}^{n-1,n'-1} - (n+n'+2) \rho_{00}^{nn'} \right) \\ & - \Gamma \rho_{00}^{nn'} + \Gamma \rho_{\downarrow\downarrow}^{nn'}. \end{aligned} \quad (\text{B.3})$$

The equations couple to the off-diagonal elements of the dot ($\uparrow\downarrow$ and $\downarrow\uparrow$) and the $n+1, n'+1$ and $n-1, n'-1$ elements of the resonators, and thus cannot form a closed set of equations. However, one can find a closed form using the fact that $\{\Gamma; g\} \gg \kappa$: the electron dynamics is much faster than the

decay and excitation processes of the resonator through the thermal bath. We therefore neglect the terms proportional to κ in Eqs. (B.1)-(B.3). When calculating the equations of motion for $\rho_{\downarrow\uparrow}^{n+1,n'}$ and $\rho_{\uparrow\downarrow}^{n,n'+1}$ we obtain the system:

$$\dot{\rho}_{\uparrow\uparrow}^{nn'} = -ig \left[\sqrt{n+1} \rho_{\downarrow\uparrow}^{n+1,n'} - \sqrt{n'+1} \rho_{\uparrow\downarrow}^{n,n'+1} \right] + \Gamma \rho_{00}^{nn'}, \quad (\text{B.4})$$

$$\dot{\rho}_{\uparrow\downarrow}^{n,n'+1} = -ig \left[\sqrt{n+1} \rho_{\downarrow\downarrow}^{n+1,n'+1} - \sqrt{n'+1} \rho_{\uparrow\uparrow}^{n,n'} \right] - \frac{\Gamma}{2} \rho_{\uparrow\downarrow}^{n,n'+1}, \quad (\text{B.5})$$

$$\dot{\rho}_{\downarrow\uparrow}^{n+1,n'} = -ig \left[\sqrt{n+1} \rho_{\uparrow\uparrow}^{n,n'} - \sqrt{n'+1} \rho_{\downarrow\downarrow}^{n+1,n'+1} \right] - \frac{\Gamma}{2} \rho_{\downarrow\uparrow}^{n+1,n'}, \quad (\text{B.6})$$

$$\dot{\rho}_{\downarrow\downarrow}^{n+1,n'+1} = -ig \left[\sqrt{n+1} \rho_{\uparrow\downarrow}^{n,n'+1} - \sqrt{n'+1} \rho_{\downarrow\uparrow}^{n+1,n'} \right] - \Gamma \rho_{\downarrow\downarrow}^{n+1,n'+1}, \quad (\text{B.7})$$

$$\dot{\rho}_{00}^{nn'} = -\Gamma \rho_{00}^{nn'} + \Gamma \rho_{\downarrow\downarrow}^{nn'}. \quad (\text{B.8})$$

Since we are interested in the stationary state, we put all time derivatives to zero. Now, from the last equation, we obtain $\rho_{00}^{nn'} = \rho_{\downarrow\downarrow}^{nn'}$, and from the relation $\rho^{nn'} = \rho_{00}^{nn'} + \rho_{\downarrow\downarrow}^{nn'} + \rho_{\uparrow\uparrow}^{nn'}$ we obtain $\rho_{00}^{nn'} = \frac{1}{2} \rho^{nn'} - \frac{1}{2} \rho_{\uparrow\uparrow}^{nn'}$, which can be inserted in Eq. (B.4). We are left with a linear system of four unknowns which has the matrix form

$$\underline{\underline{\mathbf{M}}} \mathbf{R} - \mathbf{A} = \mathbf{0}. \quad (\text{B.9})$$

We have defined:

$$\mathbf{R} = \begin{pmatrix} \rho_{\uparrow\uparrow}^{nn'} \\ \rho_{\uparrow\downarrow}^{n,n'+1} \\ \rho_{\downarrow\uparrow}^{n+1,n'} \\ \rho_{\downarrow\downarrow}^{n+1,n'+1} \end{pmatrix}, \quad \mathbf{A} = \frac{\Gamma}{2} \begin{pmatrix} \rho_{\uparrow\uparrow}^{nn'} \\ 0 \\ 0 \\ 0 \end{pmatrix}, \quad \underline{\underline{\mathbf{M}}} = \begin{pmatrix} \frac{\Gamma}{2} & -ig\sqrt{n'+1} & ig\sqrt{n+1} & 0 \\ -ig\sqrt{n'+1} & \frac{\Gamma}{2} & 0 & ig\sqrt{n+1} \\ ig\sqrt{n+1} & 0 & \frac{\Gamma}{2} & -ig\sqrt{n'+1} \\ 0 & ig\sqrt{n+1} & -ig\sqrt{n'+1} & \Gamma \end{pmatrix}. \quad (\text{B.10})$$

The steady-state equation for the matrix elements of the oscillator reads:

$$\begin{aligned} 0 = & - \left[\frac{\mathcal{N}_{nn'}' \kappa (g/g_{\text{thr}})^2}{1 + \mathcal{N}_{nn'}' (A_s^2)^{-1} (g/g_{\text{thr}})^2} \right] \rho^{nn'} + \left[\frac{\sqrt{nn'} \kappa (g/g_{\text{thr}})^2}{1 + \mathcal{N}_{n-1,n'-1} (A_s^2)^{-1} (g/g_{\text{thr}})^2} \right] \rho^{n-1,n'-1} \\ & + \frac{\mathcal{C}_d}{2} \left[2\sqrt{(n+1)(n'+1)} \rho^{n+1,n'+1} - (n+n') \rho^{nn'} \right] \\ & + \frac{\mathcal{C}_e}{2} \left[2\sqrt{nn'} \rho^{n-1,n'-1} - (n+1+n'+1) \rho^{nn'} \right], \end{aligned} \quad (\text{B.11})$$

with the following quantities:

$$g_{\text{thr}} = \frac{1}{2}\sqrt{\Gamma\kappa} \quad (\text{threshold coupling}), \quad A_s^2 = \frac{\Gamma}{3\kappa} \quad (\text{saturation number}) \quad (\text{B.12})$$

$$\mathcal{N}_{nn'} = \frac{1}{2}(n+1+n'+1) + \frac{(n-n')^2}{36} \frac{1}{A_s^2} \left(\frac{g}{g_{\text{thr}}}\right)^2, \quad (\text{B.13})$$

$$\mathcal{N}'_{nn'} = \frac{1}{2}(n+1+n'+1) + \frac{(n-n')^2}{12} \frac{1}{A_s^2} \left(\frac{g}{g_{\text{thr}}}\right)^2, \quad (\text{B.14})$$

$$\mathcal{C}_d = \kappa(1+n_B), \quad \mathcal{C}_e = \kappa n_B. \quad (\text{B.15})$$

We are interested in the diagonal elements, and thus we put $n = n'$, obtaining the equation for the distribution p_n :

$$\begin{aligned} & - \left[\frac{(n+1)\kappa \left(\frac{g}{g_{\text{thr}}}\right)^2}{1 + (n+1)(A_s^2)^{-1} \left(\frac{g}{g_{\text{thr}}}\right)^2} \right] p_n + \left[\frac{n\kappa \left(\frac{g}{g_{\text{thr}}}\right)^2}{1 + n(A_s^2)^{-1} \left(\frac{g}{g_{\text{thr}}}\right)^2} \right] p_{n-1} \\ & - \mathcal{C}_d n p_n + \mathcal{C}_d (n+1) p_{n+1} - \mathcal{C}_e (n+1) p_n + \mathcal{C}_e n p_{n-1} \\ & = 0. \end{aligned} \quad (\text{B.16})$$

To find the steady-state distribution which solves Eq. (B.16) we first rearrange the terms:

$$\begin{aligned} 0 = & - \left\{ \left[\frac{(n+1)\kappa \left(\frac{g}{g_{\text{thr}}}\right)^2}{1 + (n+1)(A_s^2)^{-1} \left(\frac{g}{g_{\text{thr}}}\right)^2} \right] p_n - \mathcal{C}_d (n+1) p_{n+1} + \mathcal{C}_e (n+1) p_n \right\} \\ & + \left[\frac{n\kappa \left(\frac{g}{g_{\text{thr}}}\right)^2}{1 + n(A_s^2)^{-1} \left(\frac{g}{g_{\text{thr}}}\right)^2} \right] p_{n-1} - \mathcal{C}_d n p_n + \mathcal{C}_e n p_{n-1}. \end{aligned} \quad (\text{B.17})$$

Then, we notice that the equation is in the form $0 = f_n - f_{n-1}$ and thus f has to be zero (detailed balance condition). We obtain the recursive equation:

$$\left[\frac{n\kappa \tilde{g}^2}{1 + n \frac{\tilde{g}^2}{A_s^2}} + \mathcal{C}_e n \right] p_{n-1} = \mathcal{C}_d p_n, \quad (\text{B.18})$$

with the shorthand $\tilde{g} = g/g_{\text{thr}}$. Equation (B.18) is equivalent to Eq. (3.12).

The solution can be written in terms of a finite product series or rising factorials:

$$p_n = p_0 \prod_{k=1}^n \left[\frac{\frac{\tilde{g}^2}{n_B+1}}{1 + k \frac{\tilde{g}^2}{A_s^2}} + \frac{n_B}{n_B+1} \right] = p_0 \frac{\left(\frac{A_s^2}{n_B} + \frac{A_s^2}{\tilde{g}^2} + 1 \right)_n}{\left(\frac{A_s^2}{\tilde{g}^2} + 1 \right)_n} \left(\frac{n_B}{n_B+1} \right)^n, \quad (\text{B.19})$$

equivalent to Eq. (3.14). The derivation outlined here assumes $P = 1$ and equal tunneling rates $\Gamma_L = \Gamma_R$,

but the general case of finite polarization and arbitrary rates simply renormalizes the saturation number A_s^2 and the threshold coupling g_{thr} , yielding the expressions in Eq. (3.13). The form of the solution for p_n remains as in Eq. (B.19).

Appendix C

Full-counting statistics of charge transport

The full-counting statistics (FCS) of charge transport is a method for evaluating the full probability distribution of electron detected by a collector, in order to gain additional information on the transport, beyond the average current. Originally, the FCS method was devised within quantum optics, in the contest of photodetection [323, 324]. Later, it has been extended to the study of quantum transport in mesoscopic conductors [212–216]. Here, I briefly outline the theory of FCS and its application to the calculation of the current noise used in Sec. 3.6.

C.1 Basic concepts

Assuming that the system dynamics is governed by a Markovian master equation as described in Ch. 2,

$$\dot{\rho} = \mathcal{L}\rho, \quad (\text{C.1})$$

we are interested in resolving the dynamics with respect to the detection or no-detection of electrons from, e.g., the right lead of a system. We can write the total Liouvillian \mathcal{L} as $\mathcal{L} = \mathcal{L}_0 + \mathcal{L}_1$, where \mathcal{L}_0 contains the detection-free evolution (the isolated dynamics of the system and the un-monitored detections) and \mathcal{L}_1 contains the detections. The propagator solving Eq. (C.1) has the general form

$$\mathcal{P}(t) = e^{\mathcal{L}t}. \quad (\text{C.2})$$

To make explicit the appearance of the quantum jumps (electron being detected in the right lead) in the evolution, we consider the Laplace transform $\mathcal{P}(z) = \int_0^\infty dt \mathcal{P}(t) e^{-zt}$ of the propagator, obtaining

$$\mathcal{P}(z) = \frac{1}{z\mathbb{1} - \mathcal{L}_0 - \mathcal{L}_1} = \frac{1}{(z\mathbb{1} - \mathcal{L}_0) \left(\mathbb{1} - \frac{\mathcal{L}_1}{z\mathbb{1} - \mathcal{L}_0} \right)}. \quad (\text{C.3})$$

Introducing the free propagator

$$\mathcal{P}_0(z) = \frac{1}{z\mathbb{1} - \mathcal{L}_0} = \int_0^\infty dt e^{\mathcal{L}_0 t} e^{-zt}, \quad (\text{C.4})$$

we can expand Eq. (C.3) as

$$\mathcal{P}(z) = \sum_{n=0}^{\infty} [\mathcal{P}_0(z) \mathcal{L}_1]^n \mathcal{P}_0(z) = \mathcal{P}_0(z) + \mathcal{P}_0(z) \mathcal{L}_1 \mathcal{P}_0(z) + \mathcal{P}_0(z) \mathcal{L}_1 \mathcal{P}_0(z) \mathcal{L}_1 \mathcal{P}_0(z) + \dots \quad (\text{C.5})$$

Using the convolution theorem, it can be shown that in the time domain we obtain

$$\mathcal{P}(t) = e^{\mathcal{L}_0 t} + \int_0^t dt_1 e^{\mathcal{L}_0(t-t_1)} \mathcal{L}_1 e^{\mathcal{L}_0 t_1} + \int_0^t dt_2 \int_0^{t_2} dt_1 e^{\mathcal{L}_0(t-t_2)} \mathcal{L}_1 e^{\mathcal{L}_0(t_2-t_1)} \mathcal{L}_1 e^{\mathcal{L}_0 t_1} + \dots \quad (\text{C.6})$$

which can be interpreted as periods of free evolution interrupted by single jump events. Since $\rho(t) = \mathcal{P}(t)\rho_0$, where ρ_0 is the density matrix at $t = 0$, we can write the probability for n jump events to occur during time t :

$$P_n(t) = \text{Tr} \left\{ \int_0^t dt_n \dots \int_0^{t_2} dt_1 e^{\mathcal{L}_0(t-t_n)} \mathcal{L}_1 \dots \mathcal{L}_1 e^{\mathcal{L}_0(t_2-t_1)} \mathcal{L}_1 e^{\mathcal{L}_0 t_1} \rho_0 \right\}. \quad (\text{C.7})$$

In Laplace space, the above equation reads simply

$$P_n(z) = \text{Tr} \{ [\mathcal{P}_0(z) \mathcal{L}_1]^n \mathcal{P}_0(z) \rho_0 \}. \quad (\text{C.8})$$

It is possible to calculate $P_n(t)$ even if we know only the full propagator, $\mathcal{P}(t)$. To this scope, we introduce the counting variable χ , conjugate to n , satisfying the orthonormality relation

$$\frac{1}{2\pi} \int_{-\pi}^{\pi} e^{in\chi} e^{-im\chi} d\chi = \delta_{nm}. \quad (\text{C.9})$$

Now, we make the replacement

$$\mathcal{L}_1 \rightarrow \mathcal{L}_1 e^{i\chi}, \quad \mathcal{L} \rightarrow \mathcal{L}(\chi) = \mathcal{L}_0 + \mathcal{L}_1 e^{i\chi}, \quad (\text{C.10})$$

in the full propagator $\mathcal{P}(\chi, t) = e^{\mathcal{L}(\chi)t}$, now depending explicitly on the counting variable χ . Using Eq. (C.9) in Eq. (C.7) we obtain

$$P_n(t) = \frac{1}{2\pi} \int_{-\pi}^{\pi} d\chi \text{Tr} \{ \mathcal{P}(\chi, t) \rho_0 \} e^{-in\chi}, \quad P_n(z) = \frac{1}{2\pi} \int_{-\pi}^{\pi} d\chi \text{Tr} \{ \mathcal{P}(\chi, z) \rho_0 \} e^{-in\chi}. \quad (\text{C.11})$$

C.2 Vector representation

For practical calculations, it is common to use a representation in which \mathcal{L} is a matrix and ρ is a column vector. To avoid confusion with the usual quantum mechanical operators acting in the Hilbert space of the usual state vectors (bras and kets) of the system, we call Liouville space the linear space of the usual operators. Operators acting in the Liouville space are called superoperators. In the following, superoperators are denoted by calligraphic symbols; operators acting in the Hilbert space will be distinguished from the usual bras and kets through double brackets, i.e., with the correspondence $O \leftrightarrow |o\rangle\rangle$. We can write a matrix representation for the superoperator O in a similar way to the Hilbert space case:

$$O = \sum_{kl} \sum_{mn} |kl\rangle\rangle \langle\langle kl|O|mn\rangle\rangle = \sum_{kl} \sum_{mn} O_{kl,mn} |kl\rangle\rangle \langle\langle mn|. \quad (\text{C.12})$$

Here, $\{|mn\rangle\rangle \equiv |m\rangle\langle n|\}$ is the system of all the projectors onto states forming an orthonormal basis of the Hilbert space, which in turn is an orthonormal basis for the Liouville space, with respect to the scalar product $\langle\langle a|b\rangle\rangle = \text{Tr}(A^\dagger B)$. The trace is performed on the system. We denote with $O_{kl,mn}$ the matrix elements of the superoperator, having four indices. The operator $O = \sum_{m,n} O_{mn} |m\rangle\langle n|$ represented by the matrix O_{mn} corresponds to the vector $|o\rangle\rangle = \sum_{m,n} O_{mn} |mn\rangle\rangle$, represented by a column vector with entries $\mathbf{o} = (O_{11}, O_{12}, O_{13}, \dots, O_{N1}, O_{N2}, \dots, O_{NN})^T$, where N is the dimension of the Hilbert space. The exact ordering depends on the chosen ordering of the indices. We can now write the total Liouvillian \mathcal{L} with its eigendecomposition:

$$\mathcal{L} = \sum_{k=0}^{N^2-1} \lambda_k |\phi_k\rangle\rangle \langle\langle \phi_k|. \quad (\text{C.13})$$

Since the Liouvillian is in general non-hermitian, the left eigenvector $|\phi_k\rangle\rangle$ and the right eigenvector $\langle\langle \phi_k|$ are in general different. However, since we assume that the system reaches a stationary state, there is an eigenvalue $\lambda_0 = 0$, with right eigenvector $|\phi_0\rangle\rangle \equiv |0\rangle\rangle = \rho_{\text{st}}$. The stationary state is assumed unique and normalized. From the orthonormality condition, $\langle\langle \phi_j|\phi_k\rangle\rangle = \delta_{jk}$ we deduce that the left eigenvector corresponding to the eigenvalue $\lambda_0 = 0$ corresponds to the identity matrix in the Liouville space, or equivalently to performing the trace $\text{Tr}(\rho_{\text{st}}) = 1$ in the Hilbert space. We denote with $\langle\langle \tilde{0}|$ the left eigenvalue. Similarly, for the χ -dependent Liouvillian we have the decomposition:

$$\mathcal{L}(\chi) = \sum_{k=0}^{N^2-1} \lambda_k(\chi) |\phi_k(\chi)\rangle\rangle \langle\langle \phi_k(\chi)|, \quad (\text{C.14})$$

with the assumption that $\lambda_0(\chi) \rightarrow 0$ for $\chi \rightarrow 0$, and all the other eigenvalues have a larger negative real part near $\chi = 0$.

C.3 Moments and cumulants

We can identify in Eq. (C.11) the moment-generating function (MGF):

$$M(\chi, t) = \text{Tr} \left\{ e^{\mathcal{L}(\chi)t} \rho_0 \right\}, \quad (\text{C.15})$$

since it is defined as the Fourier transform of the probability distribution.

From the MGF it is possible to compute all the moments by differentiation with respect to the counting field:

$$\langle n^k \rangle_t = \sum_{n=0}^{\infty} n^k P_n(t) = (-i)^n \left. \frac{\partial M(\chi, t)}{\partial \chi^n} \right|_{\chi=0}, \quad (\text{C.16})$$

where $\langle n^k \rangle_t$ denotes the k -th moment of the probability distribution at time t . Note that the MGF can also be written as

$$M(\chi, t) = \sum_{n=0}^{\infty} e^{in\chi} P_n(t), \quad (\text{C.17})$$

which is the inverse Fourier transform of Eq. (C.11). The cumulant-generating function (CGF) is obtained by taking the logarithm of the MGF,

$$C(\chi, t) = \ln M(\chi, t), \quad (\text{C.18})$$

and all the cumulants are recovered from

$$\langle\langle n^k \rangle\rangle_t = (-i)^n \left. \frac{\partial C(\chi, t)}{\partial \chi^n} \right|_{\chi=0}. \quad (\text{C.19})$$

We recall that, in contrast to moments, higher cumulants are inert when a trivial transformation such as a translation is performed on the probability distribution. It is possible to show that in the long-time limit, $t \rightarrow \infty$, the CGF is linear in time and depends on the lowest eigenvalue of the χ -dependent Liouvillian $\mathcal{L}(\chi, t)$. Evaluating Eq. (C.15) on the stationary state, and using the vector representation, we can write

$$M(\chi, t) = e^{C(\chi, t)} = \sum_k \langle\langle \tilde{0} | \phi_k(\chi) \rangle\rangle \langle\langle \phi_k(\chi) | 0 \rangle\rangle e^{\lambda_k(\chi)t}. \quad (\text{C.20})$$

In the long-time limit, the only term that survives is that with $\lambda_0(\chi)$ in the exponent, since all other terms yield exponentially damped contributions. Therefore, we have

$$e^{C(\chi, t)} \approx c(\chi) e^{\lambda_0(\chi)t}, \quad (\text{C.21})$$

with $c(\chi) = \langle\langle \tilde{0} | \phi_0(\chi) \rangle\rangle \langle\langle \phi_0(\chi) | 0 \rangle\rangle$. Taking the logarithm, we obtain $C(\chi, t) = \lambda_0(\chi)t + \ln c$, and therefore, to exponential accuracy

$$C(\chi, t) \approx \lambda_0(\chi)t. \quad (\text{C.22})$$

We can therefore find every cumulant by differentiation of the χ -dependent eigenvalue λ_0 .

C.4 Expression for the average current and the current noise

Equation (C.22) expresses the CGF for the distribution $P_n(t)$ in the long-time limit, which is the probability of n jumps events occurring in a time interval t . By identifying the jump processes with electrons entering the right lead, we can derive Eq. (C.22) with respect to time and find the current cumulants in the stationary limit:

$$\langle\langle I^m \rangle\rangle = e^m \frac{d}{dt} \lim_{t \rightarrow \infty} \langle\langle n^m \rangle\rangle(t), \quad (\text{C.23})$$

with e being the electron charge. To achieve this, we resolve the density matrix $\rho(t)$ and the master equation with respect to n . We introduce the superoperator $\mathcal{J}^{(e)}$ which is relative to the tunneling of electrons from the system to the right lead, and the superoperator $\mathcal{J}^{(h)}$, relative to the tunneling from the right lead to the system (viz., holes entering the collector). The n -resolved master equation has the form:

$$\dot{\rho}^{(n)}(t) = (\mathcal{L} - \mathcal{J}^{(e)} - \mathcal{J}^{(h)})\rho(t) + \mathcal{J}^{(e)}\rho^{(n-1)}(t) + \mathcal{J}^{(h)}\rho^{(n+1)}(t). \quad (\text{C.24})$$

It is possible to find the expression for the average current as

$$I = \langle\langle I \rangle\rangle = e \langle\langle \tilde{0} | \mathcal{J}^{(e)} - \mathcal{J}^{(h)} | 0 \rangle\rangle = e \text{Tr} [(-\mathcal{J}^{(e)} - \mathcal{J}^{(h)})\rho_{\text{st}}], \quad (\text{C.25})$$

while for the second cumulant, i.e., the zero-frequency current noise, one finds [216]

$$S(0) = \langle\langle I^2 \rangle\rangle = e \text{Tr} [(\mathcal{J}^{(e)} + \mathcal{J}^{(h)})\rho_{\text{st}}] - e^2 \text{Tr} [(\mathcal{J}^{(e)} - \mathcal{J}^{(h)})\mathcal{R}(\mathcal{J}^{(e)} - \mathcal{J}^{(h)})\rho_{\text{st}}]. \quad (\text{C.26})$$

We have introduced the pseudoinverse of the Liouvillian $\mathcal{R} = \mathcal{Q}\mathcal{L}^{-1}\mathcal{Q}$, where \mathcal{Q} is the projector out of the null-space of \mathcal{L} , which is spanned by ρ_{st} . If $\mathcal{P} \equiv |0\rangle\langle\tilde{0}|$ is the projector onto the stationary state then $\mathcal{Q} = \mathbb{1} - \mathcal{P}$. The pseudoinverse \mathcal{R} is well defined, since the inversion is performed in the subspace spanned by \mathcal{Q} , where \mathcal{L} is regular. In the infinite-bias limit, transport from right to left is blocked, thus $\mathcal{J}^{(h)} = 0$ and $\mathcal{J}^{(e)} \pm \mathcal{J}^{(h)} = \mathcal{J}^{(e)} \equiv \mathcal{J}$. Then we have

$$I = e \text{Tr} [\mathcal{J}\rho_{\text{st}}], \quad S(0) = eI - 2e^2 \text{Tr} [\mathcal{J}\mathcal{R}\mathcal{J}\rho_{\text{st}}], \quad (\text{C.27})$$

C.5 Note on the numerical evaluation of the noise

The quantum dot + resonator system described in Ch. 3 requires working with a very large Hilbert space, due to the necessity of including many Fock states (up to $n \approx 500$) to capture the lasing behavior with low quality factors. As a consequence, the actual calculation of \mathcal{R} is unfeasible. However, it is not necessary

to evaluate \mathcal{R} , but rather its action onto a vector, $\mathcal{R}|y\rangle\rangle$ [325, 326]. The trick to evaluate the second part of Eq. (C.26) is the following. We first write the linear system

$$\mathcal{L}|x\rangle\rangle = Q|y\rangle\rangle, \quad (\text{C.28})$$

where $|x\rangle\rangle$ is an unknown vector and $|y\rangle\rangle$ is known. The r.h.s. ensures that the solution lies in the range of \mathcal{L} . Since \mathcal{L} is singular, the system has infinitely many solutions which we write in the form

$$|x\rangle\rangle = |x_0\rangle\rangle + c|0\rangle\rangle, \quad c \in \mathbb{C}. \quad (\text{C.29})$$

$|x_0\rangle\rangle$ is a particular solution which is found numerically. Now, we apply \mathcal{R} to both sides of Eq. (C.28) and obtain

$$\begin{aligned} \mathcal{R}\mathcal{L}|x\rangle\rangle &= \mathcal{R}Q|y\rangle\rangle \\ Q\mathcal{L}^{-1}Q\mathcal{L}|x\rangle\rangle &= Q\mathcal{L}^{-1}Q^2|y\rangle\rangle \\ Q\mathcal{L}^{-1}\mathcal{L}Q|x\rangle\rangle &= Q\mathcal{L}^{-1}Q|y\rangle\rangle \\ Q|x\rangle\rangle &= \mathcal{R}|y\rangle\rangle. \end{aligned} \quad (\text{C.30})$$

We have used the definition of \mathcal{R} and the identities $Q^2 = Q$ and $Q\mathcal{L} = \mathcal{L}Q$. Therefore, we find numerically the solution $|x_0\rangle\rangle$ to the system (C.28) and then we apply the projector Q to Eq. (C.29), yielding $Q|x_0\rangle\rangle = \mathcal{R}|y\rangle\rangle$, since $Q|0\rangle\rangle = 0$. In our case, we need to choose $|y\rangle\rangle = I|0\rangle\rangle$. The solution of the linear system Eq. (C.29) revealed itself to be a formidable numerical problem due to the size of the matrices involved. We have used the iterative GMRES method [167] to solve the preconditioned system

$$\mathcal{M}\mathcal{L}|x\rangle\rangle = \mathcal{M}Q|y\rangle\rangle. \quad (\text{C.31})$$

The matrix \mathcal{M} is an approximation of the pseudoinverse of \mathcal{L} and it has been crucial for the convergence of the GMRES method. A wrong or absent preconditioner made the convergence impossible or extremely slow. The preconditioner was built in our case with a sparse incomplete LU decomposition (spILU) for the Liouvillian \mathcal{L} [166].

Appendix D

Operators $\mathcal{G}(\Delta_0, n)$, $\mathcal{F}(\Delta_0, n)$ and matrix element $\langle 1|H_{\text{eff}}|2\rangle$

I describe here the nonlinear operators $\mathcal{G}(\Delta_0, n)$ and $\mathcal{F}(\Delta_0, n)$ appearing in the effective Hamiltonian (Eq. 5.6) of the JJ-resonator system described in Ch. 5. They are defined by the relations:

$$\mathcal{G}(\Delta_0, n)n = \sum_{p=1}^{\infty} \frac{4p}{p^2 - 1} [A_p, A_p^\dagger], \quad (\text{D.1})$$

$$a\mathcal{F}(\Delta_0, n) = \sum_{p=0}^{\infty} \frac{(-1)^p}{2p+1} [A_p, A_{p+1}^\dagger], \quad (\text{D.2})$$

where $A_p = (a^\dagger)^p K_p$, and K_p is an hermitian operator defined as

$$K_p =: \frac{J_p(2\Delta_0\sqrt{n})}{n^{p/2}} := \sum_{m=0}^{\infty} \frac{(-1)^m \Delta_0^{2m+p} (a^\dagger)^m a^m}{m!(m+p)!}. \quad (\text{D.3})$$

Effective Hamiltonian (Eq. 5.6) can be written in the Fock basis as

$$H_{\text{eff}} = \sum_{q=0}^{\infty} (q\delta + \delta E_q) |q\rangle\langle q| + i \sum_{q=0}^{\infty} [M_{q,q+1} |q\rangle\langle q+1| e^{-2i\phi} - \text{H.c.}]. \quad (\text{D.4})$$

The matrix elements are:

$$\begin{aligned} \delta E_q &= \frac{\tilde{E}_J^2}{4\omega_J} \left\{ \sum_{p=1}^q \frac{4p}{4p^2 - 1} \left[\frac{\kappa_p^2 (q-p)q!}{(q-p)!} \right] - \sum_{p=1}^{\infty} \frac{4p}{4p^2 - 1} \left[\frac{\kappa_p^2 (q)(q+p)!}{q!} \right] \right\}, \\ M_{q,q+1} &= \frac{\tilde{E}_J^2}{4\omega_J} \left\{ \sum_{p=0}^q \frac{(-1)^p}{2p+1} \frac{\sqrt{q!(q+1)!}}{(q-p)!} \kappa_p (q-p) \kappa_{p+1} (q-p) \right. \\ &\quad \left. - \sum_{p=0}^{\infty} \frac{(-1)^p}{2p+1} \frac{(q+p+1)!}{\sqrt{q!(q+1)!}} \kappa_{p+1} (q) \kappa_p (q+1) \right\}. \end{aligned} \quad (\text{D.5})$$

$\kappa_p(q)$ represents the q -th eigenvalue of K_p and is given by

$$\kappa_p(q) = q! \sum_{n=0}^q \frac{(-1)^n \Delta_0^{2n+p}}{n!(n+p)!(q-n)!}. \quad (\text{D.6})$$

In this representation, specific matrix elements of the effective Hamiltonian can be written in closed form. We report here the element M_{12} which is of particular relevance as explained in Sec. 5.6:

$$M_{12} = \frac{\tilde{E}_J^2}{4\sqrt{2}\omega_J} \left[\Delta_0 e^{-\Delta_0^2} \left(\frac{2}{3}\Delta_0^4 - \frac{10}{3}\Delta_0^2 + \frac{3}{2} \right) + \sqrt{\pi} \text{erf}(\Delta_0) \left(\frac{2}{3}\Delta_0^6 - 3\Delta_0^4 + \frac{7}{2}\Delta_0^2 - \frac{3}{4} \right) \right], \quad (\text{D.7})$$

where $\text{erf}(x)$ is the error function. The first zero of M_{12} occurs at $\Delta_0 \approx 1.07$.

Scientific contributions

This Section contains a short review of my main scientific contributions during my time as a PhD student in the Quantum Transport Group at the University of Konstanz.

List of publications

1. **M. Mantovani**, W. Belzig, G. Rastelli, and R. Hussein, *Single-photon pump by Cooper-pair splitting*, Phys. Rev. Research **1**, 033098 (2019).
2. W. T. Morley, A. Di Marco, **M. Mantovani**, P. Stadler, W. Belzig, G. Rastelli, and A. D. Armour, *Theory of double Cooper-pair tunneling and light emission mediated by a resonator*, Phys. Rev. B **100**, 054515 (2019).
3. **M. Mantovani**, A. D. Armour, W. Belzig, and G. Rastelli, *Dynamical multistability in a quantum-dot laser*, Phys. Rev. B **99**, 045442 (2019).

Talk contributions

1. APS March Meeting 2020 – Denver, CO (USA), 2-6 March 2020 [virtual].
Title: *Dynamical multistability in a quantum-dot laser*.
2. FisMat2019 – Catania (Italy), 30 September - 4 October 2019.
Title: *Single-atom lasing and single-photon pump in quantum-dot-based hybrid devices*.
3. DPG-Frühjahrstagung 2019, Spring Meeting of the Condensed Matter Section – Regensburg (Germany), 1-5 April 2019.
Title: *Nonlocal heat transfer in mesoscopic QED architectures*.
4. DPG-Frühjahrstagung 2018, Spring Meeting of the Condensed Matter Section – Berlin (Germany), 11-16 March 2018.
Title: *Multistability in nanoelectromechanical single-atom laser: beyond the rotating-wave approximation*.

Poster presentations

1. Final SFB767 Symposium “Controlled Nanosystems” – Konstanz (Germany), 18-19 November 2019.

2. Frontiers of Quantum and Mesoscopic Thermodynamics 2019 – Prague (Czech Republic), 13-20 July 2019.
3. International School of Physics “Enrico Fermi” on Nanoscale Quantum Optics – Varenna (Italy), 23-28 July 2018.
4. Advanced School on Foundations and Applications of Nanomechanics – Trieste (Italy), 18-22 September 2017.
5. Trends in Nanoscience 2017 – Irsee (Germany), 27-30 March 2017.
6. DPG-Frühjahrstagung 2017, Spring Meeting of the Condensed Matter Section – Dresden (Germany), 19-24 March 2017.

Visiting periods

1. Collaboration with Prof. Dr. Andrew Armour at the University of Nottingham (UK), 18-22 February 2019.
2. Collaboration with experimental group of Prof. Dr. Wiebke Hasch-Guichard at the Institut Néel in Grenoble (France), 6-8 September 2017.
3. Collaboration with Prof. Dr. Andrew Armour at the University of Nottingham (UK), 6-10 February 2017.

Curriculum Vitae

Personal information

Name: Mattia Mantovani
Date of birth: 17.09.1991
Place of birth: Novara, Italy
Citizenship: Italian
Email: mattia.mantovani@uni-konstanz.de

Education

2017-2020: **PhD in Condensed Matter Physics**
Universität Konstanz, Germany
2014-2016: **Master's Degree in Physics**
Università degli Studi di Milano, Italy
2010-2014: **Bachelor's Degree in Physics**
Università degli Studi di Milano, Italy
2008-2013: **Preacademic Diploma in Classical Guitar**
Conservatorio "G. Cantelli", Novara, Italy

References

- [1] J.-M. Raimond, M. Brune, and S. Haroche, *Manipulating quantum entanglement with atoms and photons in a cavity*, Rev. Mod. Phys. **73**, 565 (2001).
- [2] H. Walther, B. T. Varcoe, B. G. Englert, and T. Becker, *Cavity quantum electrodynamics*, Rep. Prog. Phys. **69**, 1325 (2006).
- [3] S. Haroche and J.-M. Raimond, *Exploring the Quantum* (Oxford University Press, Oxford, 2006).
- [4] I. I. Rabi, *On the Process of Space Quantization*, Phys. Rev. **49**, 324 (1936).
- [5] I. I. Rabi, *Space Quantization in a Gyating Magnetic Field*, Phys. Rev. **51**, 652 (1937).
- [6] M. O. Scully and M. S. Zubairy, *Quantum Optics* (Cambridge University Press, Cambridge, 1997).
- [7] D. Braak, *Integrability of the Rabi Model*, Phys. Rev. Lett. **107**, 100401 (2011).
- [8] E. T. Jaynes and F. W. Cummings, *Comparison of quantum and semiclassical radiation theories with application to the beam maser*, Proc. IEEE **51**, 89 (1963).
- [9] I. Travěnek, *Solvability of the two-photon Rabi Hamiltonian*, Phys. Rev. A **85**, 043805 (2012).
- [10] V. V. Albert, *Quantum Rabi Model for N-State Atoms*, Phys. Rev. Lett. **108**, 180401 (2012).
- [11] R. H. Dicke, *Coherence in Spontaneous Radiation Processes*, Phys. Rev. **93**, 99 (1954).
- [12] M. Tavis and F. W. Cummings, *Exact Solution for an N-Molecule–Radiation-Field Hamiltonian*, Phys. Rev. **170**, 379 (1968).
- [13] M. Tavis and F. W. Cummings, *Approximate Solutions for an N-Molecule-Radiation-Field Hamiltonian*, Phys. Rev. **188**, 692 (1969).
- [14] E. M. Purcell, *Spontaneous Emission Probabilities at Radio Frequency*, Phys. Rev. **69**, 681 (1946).
- [15] Y. Kaluzny, P. Goy, M. Gross, J. M. Raimond, and S. Haroche, *Observation of Self-Induced Rabi Oscillations in Two-Level Atoms Excited Inside a Resonant Cavity: The Ringing Regime of Superradiance*, Phys. Rev. Lett. **51**, 1175 (1983).
- [16] D. Meschede, H. Walther, and G. Müller, *One-Atom Maser*, Phys. Rev. Lett. **54**, 551 (1985).
- [17] M. Brune, F. Schmidt-Kaler, A. Maali, J. Dreyer, E. Hagley, J. M. Raimond, and S. Haroche, *Quantum Rabi Oscillation: A Direct Test of Field Quantization in a Cavity*, Phys. Rev. Lett. **76**, 1800 (1996).
- [18] B. T. H. Varcoe, S. Brattke, M. Weidinger, and H. Walther, *Preparing pure photon number states of the radiation field*, Nature **403**, 743 (2000).
- [19] R. J. Thompson, G. Rempe, and H. J. Kimble, *Observation of normal-mode splitting for an atom in an optical cavity*, Phys. Rev. Lett. **68**, 1132 (1992).
- [20] G. Rempe, H. Walther, and N. Klein, *Observation of quantum collapse and revival in a one-atom maser*, Phys. Rev. Lett. **58**, 353 (1987).
- [21] G. Rempe, F. Schmidt-Kaler, and H. Walther, *Observation of sub-Poissonian photon statistics in a micro-maser*, Phys. Rev. Lett. **64**, 2783 (1990).
- [22] A. F. Kockum, A. Miranowicz, S. De Liberato, S. Savasta, and F. Nori, *Ultrastrong coupling between light and matter*, Nat. Rev. Phys. **1**, 19 (2019).
- [23] P. Forn-Díaz, L. Lamata, E. Rico, J. Kono, and E. Solano, *Ultrastrong coupling regimes of light-matter interaction*, Rev. Mod. Phys. **91**, 025005 (2019).
- [24] A. L. Boité, *Theoretical Methods for Ultrastrong Light–Matter Interactions*, Adv. Quantum Technol. **3**, 1900140 (2020).
- [25] T. Niemczyk, F. Deppe, H. Huebl, E. P. Menzel, F. Hocke, M. J. Schwarz, J. J. García-Ripoll, D. Zueco, T. Hümmer, E. Solano, A. Marx, and R. Gross, *Circuit quantum electrodynamics in the ultrastrong-coupling regime*, Nat. Phys. **6**, 772 (2010).
- [26] J. Casanova, G. Romero, I. Lizuain, J. J. García-Ripoll, and E. Solano, *Deep Strong Coupling Regime of the Jaynes-Cummings Model*, Phys. Rev. Lett. **105**, 263603 (2010).
- [27] P. Forn-Díaz, J. J. García-Ripoll, B. Peropadre, J.-L. Orgiazzi, M. A. Yurtalan, R. Belyansky, C. M. Wilson, and A. Lupascu, *Ultrastrong coupling of a single artificial atom to an electromagnetic continuum in the nonperturbative regime*, Nature Physics **13**, 39 (2017).

- [28] F. Yoshihara, T. Fuse, S. Ashhab, K. Kakuyanagi, S. Saito, and K. Semba, *Superconducting qubit–oscillator circuit beyond the ultrastrong-coupling regime*, Nat. Phys. **13**, 44 (2017).
- [29] A. Bayer, M. Pozimski, S. Schambeck, D. Schuh, R. Huber, D. Bougeard, and C. Lange, *Terahertz Light–Matter Interaction beyond Unity Coupling Strength*, Nano Lett. **17**, 6340 (2017).
- [30] C. Weisbuch, M. Nishioka, A. Ishikawa, and Y. Arakawa, *Observation of the coupled exciton-photon mode splitting in a semiconductor quantum microcavity*, Phys. Rev. Lett. **69**, 3314 (1992).
- [31] T. Yoshie, A. Scherer, J. Hendrickson, G. Khitrova, H. M. Gibbs, G. Rupper, C. Ell, O. B. Shchekin, and D. G. Deppe, *Vacuum Rabi splitting with a single quantum dot in a photonic crystal nanocavity*, Nature **432**, 200 (2004).
- [32] L. Childress, A. S. Sørensen, and M. D. Lukin, *Mesoscopic cavity quantum electrodynamics with quantum dots*, Phys. Rev. A **69**, 042302 (2004).
- [33] A. Cottet, T. Kontos, and B. Douçot, *Electron-photon coupling in mesoscopic quantum electrodynamics*, Phys. Rev. B **91**, 205417 (2015).
- [34] J. J. Viennot, M. R. Delbecq, L. E. Bruhat, M. C. Dartiailh, M. M. Desjardins, M. Baillergeau, A. Cottet, and T. Kontos, *Towards hybrid circuit quantum electrodynamics with quantum dots*, C. R. Phys. **17**, 705 (2016).
- [35] A. Cottet, M. C. Dartiailh, M. M. Desjardins, T. Cubaynes, L. C. Contamin, M. Delbecq, J. J. Viennot, L. E. Bruhat, B. Douçot, and T. Kontos, *Cavity QED with hybrid nanocircuits: from atomic-like physics to condensed matter phenomena*, J. Phys. Condens. Matter **29**, 433002 (2017).
- [36] G. Burkard, M. J. Gullans, X. Mi, and J. R. Petta, *Superconductor–semiconductor hybrid-circuit quantum electrodynamics*, Nat. Rev. Phys. **2**, 129 (2020).
- [37] A. Blais, R.-S. Huang, A. Wallraff, S. M. Girvin, and R. J. Schoelkopf, *Cavity quantum electrodynamics for superconducting electrical circuits: An architecture for quantum computation*, Phys. Rev. A **69**, 062320 (2004).
- [38] A. Wallraff, D. I. Schuster, A. Blais, L. Frunzio, R. S. Huang, J. Majer, S. Kumar, S. M. Girvin, and R. J. Schoelkopf, *Strong coupling of a single photon to a superconducting qubit using circuit quantum electrodynamics*, Nature **431**, 162 (2004).
- [39] H. Paik, D. I. Schuster, L. S. Bishop, G. Kirchmair, G. Catelani, A. P. Sears, B. R. Johnson, M. J. Reagor, L. Frunzio, L. I. Glazman, S. M. Girvin, M. H. Devoret, and R. J. Schoelkopf, *Observation of High Coherence in Josephson Junction Qubits Measured in a Three-Dimensional Circuit QED Architecture*, Phys. Rev. Lett. **107**, 240501 (2011).
- [40] A. Blais, A. L. Grimsmo, S. M. Girvin, and A. Wallraff, *Circuit Quantum Electrodynamics*, arXiv:2005.12667 (2020).
- [41] O. Dmytruk, M. Trif, and P. Simon, *Cavity quantum electrodynamics with mesoscopic topological superconductors*, Phys. Rev. B **92**, 245432 (2015).
- [42] E. Kim, X. Zhang, V. S. Ferreira, J. Banker, J. K. Iverson, A. Sipahigil, M. Bello, A. Gonzalez-Tudela, M. Mirhosseini, and O. Painter, *Quantum electrodynamics in a topological waveguide*, arXiv:2005.03802 (2020).
- [43] A. Imamoğlu, *Cavity QED Based on Collective Magnetic Dipole Coupling: Spin Ensembles as Hybrid Two-Level Systems*, Phys. Rev. Lett. **102**, 083602 (2009).
- [44] Y. Kubo, F. R. Ong, P. Bertet, D. Vion, V. Jacques, D. Zheng, A. Dréau, J.-F. Roch, A. Auffèves, F. Jelezko, J. Wrachtrup, M. F. Barthe, P. Bergonzo, and D. Esteve, *Strong Coupling of a Spin Ensemble to a Superconducting Resonator*, Phys. Rev. Lett. **105**, 140502 (2010).
- [45] M. Goryachev, W. G. Farr, D. L. Creedon, Y. Fan, M. Kostylev, and M. E. Tobar, *High-Cooperativity Cavity QED with Magnons at Microwave Frequencies*, Phys. Rev. Applied **2**, 054002 (2014).
- [46] D. Zhang, X.-M. Wang, T.-F. Li, X.-Q. Luo, W. Wu, F. Nori, and J. Q. You, *Cavity quantum electrodynamics with ferromagnetic magnons in a small yttrium-iron-garnet sphere*, npj Quantum Inf. **1**, 1 (2015).
- [47] X. Zhang, C.-L. Zou, L. Jiang, and H. X. Tang, *Cavity magnomechanics*, Science Advances **2**, e1501286 (2016).
- [48] A. Osada, R. Hisatomi, A. Noguchi, Y. Tabuchi, R. Yamazaki, K. Usami, M. Sadgrove, R. Yalla, M. Nomura, and Y. Nakamura, *Cavity Optomagnonics with Spin-Orbit Coupled Photons*, Phys. Rev. Lett. **116**, 223601 (2016).
- [49] D. Loss and D. P. DiVincenzo, *Quantum computation with quantum dots*, Phys. Rev. A **57**, 120 (1998).
- [50] L. P. Kouwenhoven, D. G. Austing, and S. Tarucha, *Few-electron quantum dots*, Rep. Prog. Phys. **64**, 701 (2001).
- [51] W. G. van der Wiel, S. De Franceschi, J. M. Elzerman, T. Fujisawa, S. Tarucha, and L. P. Kouwenhoven, *Electron transport through double quantum dots*, Rev. Mod. Phys. **75**, 1 (2002).

- [52] R. Hanson, L. P. Kouwenhoven, J. R. Petta, S. Tarucha, and L. M. K. Vandersypen, *Spins in few-electron quantum dots*, Rev. Mod. Phys. **79**, 1217 (2007).
- [53] E. A. Laird, F. Kuemmeth, G. A. Steele, K. Grove-Rasmussen, J. Nygård, K. Flensberg, and L. P. Kouwenhoven, *Quantum transport in carbon nanotubes*, Rev. Mod. Phys. **87**, 703 (2015).
- [54] X. Mi, M. Benito, S. Putz, D. M. Zajac, J. M. Taylor, G. Burkard, and J. R. Petta, *A coherent spin-photon interface in silicon*, Nature **555**, 599 (2018).
- [55] N. W. Hendrickx, D. P. Franke, A. Sammak, G. Scappucci, and M. Veldhorst, *Fast two-qubit logic with holes in germanium*, Nature **577**, 487 (2020).
- [56] F. Molitor, H. Knowles, S. Dröscher, U. Gasser, T. Choi, P. Roulleau, J. Güttinger, A. Jacobsen, C. Stampfer, K. Ensslin, and T. Ihn, *Observation of excited states in a graphene double quantum dot*, Europhys. Lett. **89**, 67005 (2010).
- [57] L. Banszerus, B. Frohn, A. Epping, D. Neumaier, K. Watanabe, T. Taniguchi, and C. Stampfer, *Gate-Defined Electron-Hole Double Dots in Bilayer Graphene*, Nano Lett. **18**, 4785 (2018).
- [58] A. Kurzman, H. Overweg, M. Eich, A. Pally, P. Rickhaus, R. Pisoni, Y. Lee, K. Watanabe, T. Taniguchi, T. Ihn, and K. Ensslin, *Charge Detection in Gate-Defined Bilayer Graphene Quantum Dots*, Nano Lett. **19**, 5216 (2019).
- [59] A. Kurzman, M. Eich, H. Overweg, M. Mangold, F. Herman, P. Rickhaus, R. Pisoni, Y. Lee, R. Garreis, C. Tong, K. Watanabe, T. Taniguchi, K. Ensslin, and T. Ihn, *Excited States in Bilayer Graphene Quantum Dots*, Phys. Rev. Lett. **123**, 026803 (2019).
- [60] L. Banszerus, S. Möller, E. Icking, K. Watanabe, T. Taniguchi, C. Volk, and C. Stampfer, *Single-Electron Double Quantum Dots in Bilayer Graphene*, Nano Lett., doi:10.1021/acs.nanolett.9b05295 (2020).
- [61] A. Chatterjee, P. Stevenson, S. De Franceschi, A. Morello, N. de Leon, and F. Kuemmeth, *Semiconductor Qubits In Practice*, arXiv:2005.06564 (2020).
- [62] B. D. Josephson, *Possible new effects in superconductive tunnelling*, Phys. Lett. **1**, 251 (1962).
- [63] B. D. Josephson, *Supercurrents through barriers*, Adv. Phys. **14**, 419 (1965).
- [64] B. D. Josephson, *The discovery of tunnelling supercurrents*, Rev. Mod. Phys. **46**, 251 (1974).
- [65] P.-G. de Gennes, *Superconductivity of metals and alloys*, Advanced book classics (Advanced Book Program, Perseus Books, Reading, Mass, 1999).
- [66] M. Tinkham, *Introduction to superconductivity*, 2. ed (Dover, Mineola, NY, 2004).
- [67] G. Wendin, *Quantum information processing with superconducting circuits: a review*, Rep. Prog. Phys. **80**, 106001 (2017).
- [68] X. Gu, A. F. Kockum, A. Miranowicz, Y.-x. Liu, and F. Nori, *Microwave photonics with superconducting quantum circuits*, Phys. Rep. **718-719**, 1 (2017).
- [69] M. Kjaergaard, M. E. Schwartz, J. Braumüller, P. Krantz, J. I.-J. Wang, S. Gustavsson, and W. D. Oliver, *Superconducting Qubits: Current State of Play*, Annu. Rev. Condens. Matter Phys. **11**, 369 (2020).
- [70] Y. Nakamura, Y. A. Pashkin, and J. S. Tsai, *Coherent control of macroscopic quantum states in a single-Cooper-pair box*, Nature **398**, 786 (1999).
- [71] J. Koch, T. M. Yu, J. Gambetta, A. A. Houck, D. I. Schuster, J. Majer, A. Blais, M. H. Devoret, S. M. Girvin, and R. J. Schoelkopf, *Charge-insensitive qubit design derived from the Cooper pair box*, Phys. Rev. A **76**, 042319 (2007).
- [72] F. Arute, K. Arya, R. Babbush, D. Bacon, J. C. Bardin, R. Barends, R. Biswas, S. Boixo, F. G. S. L. Brandao, D. A. Buell, B. Burkett, Y. Chen, Z. Chen, B. Chiaro, R. Collins, W. Courtney, A. Dunsworth, E. Farhi, B. Foxen, A. Fowler, C. Gidney, M. Giustina, R. Graff, K. Guerin, S. Habegger, M. P. Harrigan, M. J. Hartmann, A. Ho, M. Hoffmann, T. Huang, T. S. Humble, S. V. Isakov, E. Jeffrey, Z. Jiang, D. Kafri, K. Kechedzhi, J. Kelly, P. V. Klimov, S. Knysh, A. Korotkov, F. Kostritsa, D. Landhuis, M. Lindmark, E. Lucero, D. Lyakh, S. Mandrà, J. R. McClean, M. McEwen, A. Megrant, X. Mi, K. Michielsen, M. Mohseni, J. Mutus, O. Naaman, M. Neeley, C. Neill, M. Y. Niu, E. Ostby, A. Petukhov, J. C. Platt, C. Quintana, E. G. Rieffel, P. Roushan, N. C. Rubin, D. Sank, K. J. Satzinger, V. Smelyanskiy, K. J. Sung, M. D. Trevithick, A. Vainsencher, B. Villalonga, T. White, Z. J. Yao, P. Yeh, A. Zalcman, H. Neven, and J. M. Martinis, *Quantum supremacy using a programmable superconducting processor*, Nature **574**, 505 (2019).
- [73] J. E. Mooij, T. P. Orlando, L. Levitov, L. Tian, C. H. van der Wal, and S. Lloyd, *Josephson Persistent-Current Qubit*, Science **285**, 1036 (1999).
- [74] C. H. van der Wal, A. C. J. ter Haar, F. K. Wilhelm, R. N. Schouten, C. J. P. M. Harmans, T. P. Orlando, S. Lloyd, and J. E. Mooij, *Quantum Superposition of Macroscopic Persistent-Current States*, Science **290**, 773 (2000).
- [75] J. R. Friedman, V. Patel, W. Chen, S. K. Tolpygo, and J. E. Lukens, *Quantum superposition of distinct macroscopic states*, Nature **406**, 43 (2000).

- [76] I. Chiorescu, Y. Nakamura, C. J. P. M. Harmans, and J. E. Mooij, *Coherent Quantum Dynamics of a Superconducting Flux Qubit*, Science **299**, 1869 (2003).
- [77] M. W. Johnson, M. H. S. Amin, S. Gildert, T. Lanting, F. Hamze, N. Dickson, R. Harris, A. J. Berkley, J. Johansson, P. Bunyk, E. M. Chapple, C. Enderud, J. P. Hilton, K. Karimi, E. Ladizinsky, N. Ladizinsky, T. Oh, I. Perminov, C. Rich, M. C. Thom, E. Tolkacheva, C. J. S. Truncik, S. Uchaikin, J. Wang, B. Wilson, and G. Rose, *Quantum annealing with manufactured spins*, Nature **473**, 194 (2011).
- [78] J. M. Martinis, M. H. Devoret, and J. Clarke, *Energy-Level Quantization in the Zero-Voltage State of a Current-Biased Josephson Junction*, Phys. Rev. Lett. **55**, 1543 (1985).
- [79] J. Clarke, A. N. Cleland, M. H. Devoret, D. Esteve, and J. M. Martinis, *Quantum Mechanics of a Macroscopic Variable: The Phase Difference of a Josephson Junction*, Science **239**, 992 (1988).
- [80] Y. Yu, S. Han, X. Chu, S.-I. Chu, and Z. Wang, *Coherent Temporal Oscillations of Macroscopic Quantum States in a Josephson Junction*, Science **296**, 889 (2002).
- [81] J. M. Martinis, *Superconducting phase qubits*, Quantum Inf. Process. **8**, 81 (2009).
- [82] A. Cottet, D. Vion, A. Aassime, P. Joyez, D. Esteve, and M. Devoret, *Implementation of a combined charge-phase quantum bit in a superconducting circuit*, Physica C: Superconductivity **367**, 197 (2002).
- [83] J. Q. You, X. Hu, S. Ashhab, and F. Nori, *Low-decoherence flux qubit*, Phys. Rev. B **75**, 140515 (2007).
- [84] M. Steffen, M. Ansmann, R. McDermott, N. Katz, R. C. Bialczak, E. Lucero, M. Neeley, E. M. Weig, A. N. Cleland, and J. M. Martinis, *State Tomography of Capacitively Shunted Phase Qubits with High Fidelity*, Phys. Rev. Lett. **97**, 050502 (2006).
- [85] P. Bertet, I. Chiorescu, G. Burkard, K. Semba, C. J. P. M. Harmans, D. P. DiVincenzo, and J. E. Mooij, *Dephasing of a Superconducting Qubit Induced by Photon Noise*, Phys. Rev. Lett. **95**, 257002 (2005).
- [86] F. G. Paauw, A. Fedorov, C. J. P. M. Harmans, and J. E. Mooij, *Tuning the Gap of a Superconducting Flux Qubit*, Phys. Rev. Lett. **102**, 090501 (2009).
- [87] V. E. Manucharyan, J. Koch, L. I. Glazman, and M. H. Devoret, *Fluxonium: Single Cooper-Pair Circuit Free of Charge Offsets*, Science **326**, 113 (2009).
- [88] R. Barends, J. Kelly, A. Megrant, D. Sank, E. Jeffrey, Y. Chen, Y. Yin, B. Chiaro, J. Mutus, C. Neill, P. O'Malley, P. Roushan, J. Wenner, T. C. White, A. N. Cleland, and J. M. Martinis, *Coherent Josephson Qubit Suitable for Scalable Quantum Integrated Circuits*, Phys. Rev. Lett. **111**, 080502 (2013).
- [89] Y. Chen, C. Neill, P. Roushan, N. Leung, M. Fang, R. Barends, J. Kelly, B. Campbell, Z. Chen, B. Chiaro, A. Dunsworth, E. Jeffrey, A. Megrant, J. Y. Mutus, P. J. J. O'Malley, C. M. Quintana, D. Sank, A. Vainsencher, J. Wenner, T. C. White, M. R. Geller, A. N. Cleland, and J. M. Martinis, *Qubit Architecture with High Coherence and Fast Tunable Coupling*, Phys. Rev. Lett. **113**, 220502 (2014).
- [90] T. W. Larsen, K. D. Petersson, F. Kuemmeth, T. S. Jespersen, P. Krogstrup, J. Nygård, and C. M. Marcus, *Semiconductor-Nanowire-Based Superconducting Qubit*, Phys. Rev. Lett. **115**, 127001 (2015).
- [91] A. Gyenis, P. S. Mundada, A. Di Paolo, T. M. Hazard, X. You, D. I. Schuster, J. Koch, A. Blais, and A. A. Houck, *Experimental realization of an intrinsically error-protected superconducting qubit*, arXiv:1910.07542 (2019).
- [92] C. J. Hood, H. J. Kimble, and J. Ye, *Characterization of high-finesse mirrors: Loss, phase shifts, and mode structure in an optical cavity*, Phys. Rev. A **64**, 033804 (2001).
- [93] D. W. Vernooy, A. Furusawa, N. P. Georgiades, V. S. Ilchenko, and H. J. Kimble, *Cavity QED with high- Q whispering gallery modes*, Phys. Rev. A **57**, R2293 (1998).
- [94] D. K. Armani, T. J. Kippenberg, S. M. Spillane, and K. J. Vahala, *Ultra-high- Q toroid microcavity on a chip*, Nature **421**, 925 (2003).
- [95] B. Lev, K. Srinivasan, P. Barclay, O. Painter, and H. Mabuchi, *Feasibility of detecting single atoms using photonic bandgap cavities*, Nanotechnology **15**, S556 (2004).
- [96] M. A. Sillanpää, J. I. Park, and R. W. Simmonds, *Coherent quantum state storage and transfer between two phase qubits via a resonant cavity*, Nature **449**, 438 (2007).
- [97] M. Hofheinz, E. M. Weig, M. Ansmann, R. C. Bialczak, E. Lucero, M. Neeley, A. D. O'Connell, H. Wang, J. M. Martinis, and A. N. Cleland, *Generation of Fock states in a superconducting quantum circuit*, Nature **454**, 310 (2008).
- [98] M. Hofheinz, H. Wang, M. Ansmann, R. C. Bialczak, E. Lucero, M. Neeley, A. D. O'Connell, D. Sank, J. Wenner, J. M. Martinis, and A. N. Cleland, *Synthesizing arbitrary quantum states in a superconducting resonator*, Nature **459**, 546 (2009).
- [99] D. Rugar, R. Budakian, H. J. Mamin, and B. W. Chui, *Single spin detection by magnetic resonance force microscopy*, Nature **430**, 329 (2004).
- [100] J. Chaste, A. Eichler, J. Moser, G. Ceballos, R. Rurali, and A. Bachtold, *A nanomechanical mass sensor with yoctogram resolution*, Nat. Nanotechnol. **7**, 301 (2012).
- [101] M. Poot and H. S. van der Zant, *Mechanical systems in the quantum regime*, Phys. Rep. **511**, 273 (2012).

- [102] J. Moser, A. Eichler, J. Güttinger, M. I. Dykman, and A. Bachtold, *Nanotube mechanical resonators with quality factors of up to 5 million*, Nat. Nanotechnol. **9**, 1007 (2014).
- [103] I. Wilson-Rae, P. Zoller, and A. Imamoglu, *Laser Cooling of a Nanomechanical Resonator Mode to its Quantum Ground State*, Phys. Rev. Lett. **92**, 075507 (2004).
- [104] M. P. Blencowe, J. Imbers, and A. D. Armour, *Dynamics of a nanomechanical resonator coupled to a superconducting single-electron transistor*, New J. Phys. **7**, 236 (2005).
- [105] Y.-C. Liu, Y.-F. Xiao, X. Luan, and C. W. Wong, *Dynamic Dissipative Cooling of a Mechanical Resonator in Strong Coupling Optomechanics*, Phys. Rev. Lett. **110**, 153606 (2013).
- [106] T. Ojanen and K. Børkje, *Ground-state cooling of mechanical motion in the unresolved sideband regime by use of optomechanically induced transparency*, Phys. Rev. A **90**, 013824 (2014).
- [107] P. Stadler, W. Belzig, and G. Rastelli, *Ground-State Cooling of a Carbon Nanomechanical Resonator by Spin-Polarized Current*, Phys. Rev. Lett. **113**, 47201 (2014).
- [108] P. Stadler, W. Belzig, and G. Rastelli, *Ground-State Cooling of a Mechanical Oscillator by Interference in Andreev Reflection*, Phys. Rev. Lett. **117**, 197202 (2016).
- [109] A. Naik, O. Buu, M. D. LaHaye, A. D. Armour, A. A. Clerk, M. P. Blencowe, and K. C. Schwab, *Cooling a nanomechanical resonator with quantum back-action*, Nature **443**, 193 (2006).
- [110] A. D. O'Connell, M. Hofheinz, M. Ansmann, R. C. Bialczak, M. Lenander, E. Lucero, M. Neeley, D. Sank, H. Wang, M. Weides, J. Wenner, J. M. Martinis, and A. N. Cleland, *Quantum ground state and single-phonon control of a mechanical resonator*, Nature **464**, 697 (2010).
- [111] J. D. Teufel, T. Donner, D. Li, J. W. Harlow, M. S. Allman, K. Cicak, A. J. Sirois, J. D. Whittaker, K. W. Lehnert, and R. W. Simmonds, *Sideband cooling of micromechanical motion to the quantum ground state*, Nature **475**, 359 (2011).
- [112] J. Chan, T. P. M. Alegre, A. H. Safavi-Naeini, J. T. Hill, A. Krause, S. Gröblacher, M. Aspelmeyer, and O. Painter, *Laser cooling of a nanomechanical oscillator into its quantum ground state*, Nature **478**, 89 (2011).
- [113] R. W. Peterson, T. P. Purdy, N. S. Kampel, R. W. Andrews, P.-L. Yu, K. W. Lehnert, and C. A. Regal, *Laser Cooling of a Micromechanical Membrane to the Quantum Backaction Limit*, Phys. Rev. Lett. **116**, 063601 (2016).
- [114] J. B. Clark, F. Lecocq, R. W. Simmonds, J. Aumentado, and J. D. Teufel, *Sideband cooling beyond the quantum backaction limit with squeezed light*, Nature **541**, 191 (2017).
- [115] T. Frey, P. J. Leek, M. Beck, A. Blais, T. Ihn, K. Ensslin, and A. Wallraff, *Dipole coupling of a double quantum dot to a microwave resonator*, Phys. Rev. Lett. **108**, 046807 (2012).
- [116] J. Basset, D.-D. Jarausch, A. Stockklauser, T. Frey, C. Reichl, W. Wegscheider, T. M. Ihn, K. Ensslin, and A. Wallraff, *Single-electron double quantum dot dipole-coupled to a single photonic mode*, Phys. Rev. B **88**, 125312 (2013).
- [117] X. Mi, J. V. Cady, D. M. Zajac, P. W. Deelman, and J. R. Petta, *Strong coupling of a single electron in silicon to a microwave photon*, Science **355**, 156 (2017).
- [118] Y. Li, S.-X. Li, F. Gao, H.-O. Li, G. Xu, K. Wang, D. Liu, G. Cao, M. Xiao, T. Wang, J.-J. Zhang, G.-C. Guo, and G.-P. Guo, *Coupling a Germanium Heterostructure Quantum Dot to a Superconducting Microwave Resonator*, Nano Lett. **18**, 2091 (2018).
- [119] R. Wang, R. S. Deacon, J. Sun, J. Yao, C. M. Lieber, and K. Ishibashi, *Gate Tunable Hole Charge Qubit Formed in a Ge/Si Nanowire Double Quantum Dot Coupled to Microwave Photons*, Nano Lett. **19**, 1052 (2019).
- [120] B.-C. Wang, T. Lin, H.-O. Li, S.-S. Gu, M.-B. Chen, G.-C. Guo, H.-W. Jiang, X. Hu, G. Cao, and G.-P. Guo, *Correlated spectrum of distant semiconductor qubits coupled by microwave photons*, arXiv:2001.11303 (2020).
- [121] G. A. Steele, A. K. Hüttel, B. Witkamp, M. Poot, H. B. Meerwaldt, L. P. Kouwenhoven, and H. S. J. van der Zant, *Strong Coupling Between Single-Electron Tunneling and Nanomechanical Motion*, Science **325**, 1103 (2009).
- [122] Y. Okazaki, I. Mahboob, K. Onomitsu, S. Sasaki, and H. Yamaguchi, *Gate-controlled electromechanical backaction induced by a quantum dot*, Nat. Commun. **7**, 11132 (2016).
- [123] A. Pályi, P. R. Struck, M. Rudner, K. Flensberg, and G. Burkard, *Spin-Orbit-Induced Strong Coupling of a Single Spin to a Nanomechanical Resonator*, Phys. Rev. Lett. **108**, 206811 (2012).
- [124] J. J. Viennot, M. C. Dartiailh, A. Cottet, and T. Kontos, *Coherent coupling of a single spin to microwave cavity photons*, Science **349**, 408 (2015).
- [125] X. Mi, S. Kohler, and J. R. Petta, *Landau-Zener interferometry of valley-orbit states in Si/SiGe double quantum dots*, Phys. Rev. B **98**, 161404(R) (2018).

- [126] N. Samkharadze, G. Zheng, N. Kalhor, D. Brousse, A. Sammak, U. C. Mendes, A. Blais, G. Scappucci, and L. M. K. Vandersypen, *Strong spin-photon coupling in silicon*, Science **359**, 1123 (2018).
- [127] A. J. Landig, J. V. Koski, P. Scarlino, U. C. Mendes, A. Blais, C. Reichl, W. Wegscheider, A. Wallraff, K. Ensslin, and T. Ihn, *Coherent spin-photon coupling using a resonant exchange qubit*, Nature **560**, 179 (2018).
- [128] T. Cubaynes, M. R. Delbecq, M. C. Dartiailh, R. Assouly, M. M. Desjardins, L. C. Contamin, L. E. Bruhat, Z. Leghtas, F. Mallet, A. Cottet, and T. Kontos, *Highly coherent spin states in carbon nanotubes coupled to cavity photons*, npj Quantum Inf. **5**, 47 (2019).
- [129] A. Pan, T. E. Keating, M. F. Gyure, E. J. Pritchett, S. Quinn, R. S. Ross, T. D. Ladd, and J. Kerckhoff, *Resonant exchange operation in triple-quantum-dot qubits for spin-photon transduction*, Quantum Sci. Technol. **5**, 034005 (2020).
- [130] J. D. Teufel, D. Li, M. S. Allman, K. Cicak, A. J. Sirois, J. D. Whittaker, and R. W. Simmonds, *Circuit cavity electromechanics in the strong-coupling regime*, Nature **471**, 204 (2011).
- [131] M. Aspelmeyer, T. J. Kippenberg, and F. Marquardt, *Cavity optomechanics*, Rev. Mod. Phys. **86**, 1391 (2014).
- [132] G.-W. Deng, D. Zhu, X.-H. Wang, C.-L. Zou, J.-T. Wang, H.-O. Li, G. Cao, D. Liu, Y. Li, M. Xiao, G.-C. Guo, K.-L. Jiang, X.-C. Dai, and G.-P. Guo, *Strongly Coupled Nanotube Electromechanical Resonators*, Nano Lett. **16**, 5456 (2016).
- [133] G. Luo, Z.-Z. Zhang, G.-W. Deng, H.-O. Li, G. Cao, M. Xiao, G.-C. Guo, L. Tian, and G.-P. Guo, *Strong indirect coupling between graphene-based mechanical resonators via a phonon cavity*, Nat. Commun. **9**, 383 (2018).
- [134] Z.-Z. Zhang, X.-X. Song, G. Luo, Z.-J. Su, K.-L. Wang, G. Cao, H.-O. Li, M. Xiao, G.-C. Guo, L. Tian, G.-W. Deng, and G.-P. Guo, *Coherent phonon dynamics in spatially separated graphene mechanical resonators*, Proc. Natl. Acad. Sci. USA **117**, 5582 (2020).
- [135] J. J. Viennot, M. R. Delbecq, M. C. Dartiailh, A. Cottet, and T. Kontos, *Out-of-equilibrium charge dynamics in a hybrid circuit quantum electrodynamics architecture*, Phys. Rev. B **89**, 165404 (2014).
- [136] A. Stockklauser, V. F. Maisi, J. Basset, K. Cujia, C. Reichl, W. Wegscheider, T. Ihn, A. Wallraff, and K. Ensslin, *Microwave Emission from Hybridized States in a Semiconductor Charge Qubit*, Phys. Rev. Lett. **115**, 046802 (2015).
- [137] L. E. Bruhat, J. J. Viennot, M. C. Dartiailh, M. M. Desjardins, T. Kontos, and A. Cottet, *Cavity Photons as a Probe for Charge Relaxation Resistance and Photon Emission in a Quantum Dot Coupled to Normal and Superconducting Continua*, Phys. Rev. X **6**, 021014 (2016).
- [138] Y.-Y. Liu, K. D. D. Petersson, J. Stehlik, J. M. M. Taylor, and J. R. R. Petta, *Photon Emission from a Cavity-Coupled Double Quantum Dot*, Phys. Rev. Lett. **113**, 036801 (2014).
- [139] Y.-Y. Liu, J. Stehlik, C. Eichler, M. J. Gullans, J. M. Taylor, and J. R. Petta, *Semiconductor double quantum dot micromaser*, Science **347**, 285 (2015).
- [140] Y.-Y. Liu, J. Stehlik, C. Eichler, X. Mi, T. R. Hartke, M. J. Gullans, J. M. Taylor, and J. R. Petta, *Threshold Dynamics of a Semiconductor Single Atom Maser*, Phys. Rev. Lett. **119**, 097702 (2017).
- [141] Y.-Y. Liu, T. R. Hartke, J. Stehlik, and J. R. Petta, *Phase locking of a semiconductor double-quantum-dot single-atom maser*, Phys. Rev. A **96**, 053816 (2017).
- [142] C. Urgell, W. Yang, S. L. D. Bonis, C. Samanta, M. J. Esplandiu, Q. Dong, Y. Jin, and A. Bachtold, *Cooling and self-oscillation in a nanotube electromechanical resonator*, Nat. Phys. **16**, 32 (2019).
- [143] Y. Wen, N. Ares, F. J. Schupp, T. Pei, G. A. D. Briggs, and E. A. Laird, *A coherent nanomechanical oscillator driven by single-electron tunnelling*, Nat. Phys. **16**, 75 (2019).
- [144] K. Willick and J. Baugh, *Self-driven oscillation in Coulomb blockaded suspended carbon nanotubes*, arXiv:2003.01229 (2020).
- [145] L. Hofstetter, S. Csonka, J. Nygård, and C. Schönenberger, *Cooper pair splitter realized in a two-quantum-dot Y-junction*, Nature **461**, 960 (2009).
- [146] L. G. Herrmann, F. Portier, P. Roche, A. L. Yeyati, T. Kontos, and C. Strunk, *Carbon Nanotubes as Cooper-Pair Beam Splitters*, Phys. Rev. Lett. **104**, 026801 (2010).
- [147] M. M. Desjardins, J. J. Viennot, M. C. Dartiailh, L. E. Bruhat, M. R. Delbecq, M. Lee, M.-S. Choi, A. Cottet, and T. Kontos, *Observation of the frozen charge of a Kondo resonance*, Nature **545**, 71 (2017).
- [148] I. V. Borzenets, J. Shim, J. C. H. Chen, A. Ludwig, A. D. Wieck, S. Tarucha, H.-S. Sim, and M. Yamamoto, *Observation of the Kondo screening cloud*, Nature **579**, 210 (2020).
- [149] M. C. Dartiailh, T. Kontos, B. Douçot, and A. Cottet, *Direct Cavity Detection of Majorana Pairs*, Phys. Rev. Lett. **118**, 126803 (2017).
- [150] M. Trif and P. Simon, *Braiding of Majorana Fermions in a Cavity*, Phys. Rev. Lett. **122**, 236803 (2019).

- [151] V. Gorini, A. Kossakowski, and E. C. G. Sudarshan, *Completely positive dynamical semigroups of N -level systems*, J. Math. Phys. **17**, 821 (1976).
- [152] G. Lindblad, *On the generators of quantum dynamical semigroups*, Commun. Math. Phys. **48**, 119 (1976).
- [153] A. G. Redfield, *On the Theory of Relaxation Processes*, IBM J. Res. Develop. **1**, 19 (1957).
- [154] H. J. Carmichael, *An Open Systems Approach to Quantum Optics* (Springer-Verlag, Berlin, 1993).
- [155] H.-P. Breuer and F. Petruccione, *The Theory of Open Quantum Systems* (Oxford University Press, Oxford, 2002).
- [156] K. Blum, *Density matrix theory and applications*, 3rd ed. (Springer-Verlag, Heidelberg, 2012).
- [157] H. J. Carmichael, *Statistical Methods in Quantum Optics 1: Master Equations and Fokker-Planck Equations* (Springer-Verlag, Berlin, 1999).
- [158] C. W. Gardiner and P. Zoller, *Quantum Noise* (Springer-Verlag, Berlin, 2004).
- [159] J. L. Schiff, *The Laplace Transform* (Springer, New York, NY, 1999).
- [160] U. M. Ascher and L. R. Petzold, *Computer methods for ordinary differential equations and differential-algebraic equations* (Society for Industrial and Applied Mathematics, Philadelphia, 1998).
- [161] J. Dalibard, Y. Castin, and K. Mølmer, *Wave-function approach to dissipative processes in quantum optics*, Phys. Rev. Lett. **68**, 580 (1992).
- [162] K. Mølmer, Y. Castin, and J. Dalibard, *Monte Carlo wave-function method in quantum optics*, J. Opt. Soc. Am. B **10**, 524 (1993).
- [163] H. J. Carmichael, *Statistical Methods in Quantum Optics 2: Non-Classical Fields* (Springer-Verlag, Berlin, 2008).
- [164] D. F. Walls and G. J. Milburn, *Quantum Optics*, 2nd ed. (Springer-Verlag, Berlin, 2008).
- [165] H. M. Wiseman and G. J. Milburn, *Quantum Measurement and Control* (Cambridge University Press, Cambridge, 2010).
- [166] Y. Saad, *Iterative Methods for Sparse Linear Systems*, Other Titles in Applied Mathematics (Society for Industrial and Applied Mathematics, 2003).
- [167] Y. Saad and M. H. Schultz, *GMRES: A Generalized Minimal Residual Algorithm for Solving Nonsymmetric Linear Systems*, SIAM J. Sci. and Stat. Comput. **7**, 856 (1986).
- [168] **M. Mantovani**, A. D. Armour, W. Belzig, and G. Rastelli, *Dynamical multistability in a quantum-dot laser*, Phys. Rev. B **99**, 045442 (2019).
- [169] H. Haken, *Laser Theory* (Springer-Verlag, Berlin, 1984).
- [170] A. E. Siegman, *Lasers* (University Science Books, Mill Valley, CA, 1986).
- [171] M. O. Scully and W. E. Lamb, *Quantum Theory of an Optical Maser*, Phys. Rev. Lett. **16**, 853 (1966).
- [172] M. O. Scully and W. E. Lamb, *Quantum Theory of an Optical Maser. I. General Theory*, Phys. Rev. **159**, 208 (1967).
- [173] M. Sargent, M. O. Scully, and W. E. Lamb, *Laser Physics* (Addison-Wesley, Reading, Massachusetts, 1993).
- [174] Y. Mu and C. M. Savage, *One-atom lasers*, Phys. Rev. A **46**, 5944 (1992).
- [175] J. McKeever, A. Boca, A. D. Boozer, J. R. Buck, and H. J. Kimble, *Experimental realization of a one-atom laser in the regime of strong coupling*, Nature **425**, 268 (2003).
- [176] H. J. Carmichael and L. A. Orozco, *Single atom lases orderly light*, Nature **425**, 246 (2003).
- [177] P. Filipowicz, J. Javanainen, and P. Meystre, *Theory of a microscopic maser*, Phys. Rev. A **34**, 3077 (1986).
- [178] L. A. Lugiato, M. O. Scully, and H. Walther, *Connection between microscopic and macroscopic maser theory*, Phys. Rev. A **36**, 740 (1987).
- [179] O. Astafiev, K. Inomata, A. O. Niskanen, T. Yamamoto, Y. A. Pashkin, Y. Nakamura, and J. S. Tsai, *Single artificial-atom lasing*, Nature **449**, 588 (2007).
- [180] S. André, V. Brosco, A. Shnirman, and G. Schön, *Phase diffusion and locking in single-qubit lasers*, Phys. Rev. A **79**, 053848 (2009).
- [181] S. Ashhab, J. R. Johansson, A. M. Zagoskin, and F. Nori, *Single-artificial-atom lasing using a voltage-biased superconducting charge qubit*, New J. Phys. **11**, 023030 (2009).
- [182] M. Nomura, N. Kumagai, S. Iwamoto, Y. Ota, and Y. Arakawa, *Laser oscillation in a strongly coupled single-quantum-dot-nanocavity system*, Nat. Phys. **6**, 279 (2010).
- [183] D. A. Rodrigues, J. Imbers, and A. D. Armour, *Quantum dynamics of a resonator driven by a superconducting single-electron transistor: A solid-state analogue of the micromaser*, Phys. Rev. Lett. **98**, 067204 (2007).
- [184] D. A. Rodrigues, J. Imbers, T. J. Harvey, and A. D. Armour, *Dynamical instabilities of a resonator driven by a superconducting single-electron transistor*, New J. Phys. **9**, 84 (2007).

- [185] F. Chen, J. Li, A. D. Armour, E. Brahim, J. Stettenheim, A. J. Sirois, R. W. Simmonds, M. P. Blencowe, and A. J. Rimberg, *Realization of a single-Cooper-pair Josephson laser*, Phys. Rev. B **90**, 020506(R) (2014).
- [186] M. C. Cassidy, A. Bruno, S. Rubbert, M. Irfan, J. Kammhuber, R. N. Schouten, A. R. Akhmerov, and L. P. Kouwenhoven, *Demonstration of an ac Josephson junction laser*, Science **355**, 939 (2017).
- [187] P.-Q. Jin, M. Marthaler, J. H. Cole, A. Shnirman, and G. Schön, *Lasing and transport in a quantum-dot resonator circuit*, Phys. Rev. B **84**, 035322 (2011).
- [188] J. Jin, M. Marthaler, P.-Q. Jin, D. Golubev, and G. Schön, *Noise spectrum of a quantum dot-resonator lasing circuit*, New J. Phys. **15**, 025044 (2013).
- [189] M. Kulkarni, O. Cotlet, and H. E. Türeci, *Cavity-coupled double-quantum dot at finite bias: Analogy with lasers and beyond*, Phys. Rev. B **90**, 125402 (2014).
- [190] N. Lambert, F. Nori, and C. Flindt, *Bistable Photon Emission from a Solid-State Single-Atom Laser*, Phys. Rev. Lett. **115**, 216803 (2015).
- [191] M. J. Gullans, Y.-Y. Liu, J. Stehlik, J. R. Petta, and J. M. Taylor, *Phonon-Assisted Gain in a Semiconductor Double Quantum Dot Maser*, Phys. Rev. Lett. **114**, 196802 (2015).
- [192] B. K. Agarwalla, M. Kulkarni, and D. Segal, *Photon statistics of a double quantum dot micromaser: Quantum treatment*, Phys. Rev. B **100**, 035412 (2019).
- [193] G. Rastelli and M. Governale, *Single atom laser in normal-superconductor quantum dots*, Phys. Rev. B **100**, 085435 (2019).
- [194] S. M. Tabatabaei and N. Jahangiri, *Lasing in a coupled hybrid double quantum dot-resonator system*, Phys. Rev. B **101**, 115135 (2020).
- [195] K. Vahala, M. Herrmann, S. Knünz, V. Batteiger, G. Saathoff, T. W. Hänsch, and T. Udem, *A phonon laser*, Nat. Phys. **5**, 682 (2009).
- [196] I. Mahboob, K. Nishiguchi, A. Fujiwara, and H. Yamaguchi, *Phonon Lasing in an Electromechanical Resonator*, Phys. Rev. Lett. **110**, 127202 (2013).
- [197] P. Stadler, W. Belzig, and G. Rastelli, *Control of vibrational states by spin-polarized transport in a carbon nanotube resonator*, Phys. Rev. B **91**, 085432 (2015).
- [198] A. V. Parafilo, S. I. Kulinich, L. Y. Gorelik, M. N. Kiselev, R. I. Shekhter, and M. Jonson, *Spin-mediated Photomechanical Coupling of a Nanoelectromechanical Shuttle*, Phys. Rev. Lett. **117**, 057202 (2016).
- [199] M. Benito, X. Mi, J. M. Taylor, J. R. Petta, and G. Burkard, *Input-output theory for spin-photon coupling in Si double quantum dots*, Phys. Rev. B **96**, 235434 (2017).
- [200] A. J. Landig, J. V. Koski, P. Scarlino, C. Müller, J. C. Abadillo-Uriel, B. Kratochwil, C. Reichl, W. Wegscheider, S. N. Coppersmith, M. Friesen, A. Wallraff, T. Ihn, and K. Ensslin, *Virtual-photon-mediated spin-qubit-transmon coupling*, Nat. Commun. **10**, doi:10.1038/s41467-019-13000-z (2019).
- [201] M. Braun, J. König, and J. Martinek, *Theory of transport through quantum-dot spin valves in the weak-coupling regime*, Phys. Rev. B **70**, 195345 (2004).
- [202] S. Sahoo, T. Kontos, J. Furer, C. Hoffmann, M. Gräber, A. Cottet, and C. Schönenberger, *Electric field control of spin transport*, Nat. Phys. **1**, 99 (2005).
- [203] A. Bordoloi, V. Zannier, L. Sorba, C. Schönenberger, and A. Baumgartner, *A Double Quantum Dot Spin Valve*, arXiv:1912.02136 (2019).
- [204] A. Khaetskii, V. N. Golovach, X. Hu, and I. Žutić, *Proposal for a Phonon Laser Utilizing Quantum-Dot Spin States*, Phys. Rev. Lett. **111**, 186601 (2013).
- [205] C. Timm, *Tunneling through molecules and quantum dots: Master-equation approaches*, Phys. Rev. B **77**, 195416 (2008).
- [206] M. Cattaneo, G. L. Giorgi, S. Maniscalco, and R. Zambrini, *Local versus global master equation with common and separate baths: superiority of the global approach in partial secular approximation*, New J. Phys. **21**, 113045 (2019).
- [207] M. Ziese, *Extrinsic magnetotransport phenomena in ferromagnetic oxides*, Rep. Prog. Phys. **65**, 143 (2002).
- [208] J. Johansson, P. Nation, and F. Nori, *QuTiP: An open-source Python framework for the dynamics of open quantum systems*, Comput. Phys. Commun. **183**, 1760 (2012).
- [209] U. Fano, *Ionization Yield of Radiations. II. The Fluctuations of the Number of Ions*, Phys. Rev. **72**, 26 (1947).
- [210] F. Marquardt, J. G. Harris, and S. M. Girvin, *Dynamical multistability induced by radiation pressure in high-finesse micromechanical optical cavities*, Phys. Rev. Lett. **96**, 103901 (2006).
- [211] S. H. Strogatz, *Nonlinear dynamics and chaos*, 2nd ed. (Westview Press, Boulder, CO, 2015).
- [212] L. S. Levitov and G. B. Lesovik, *Charge distribution in quantum shot noise*, JETP Lett. **58**, 230 (1993).
- [213] L. S. Levitov, H. Lee, and G. B. Lesovik, *Electron counting statistics and coherent states of electric current*, J. Math. Phys. **37**, 4845 (1996).

- [214] Y. M. Blanter and M. Büttiker, *Shot noise in mesoscopic conductors*, Phys. Rep. **336**, 1 (2000).
- [215] D. A. Bagrets and Y. V. Nazarov, *Full counting statistics of charge transfer in Coulomb blockade systems*, Phys. Rev. B **67**, 85316 (2003).
- [216] C. Flindt, T. Novotný, and A. P. Jauho, *Full counting statistics of nano-electromechanical systems*, Europhys. Lett. **69**, 475 (2005).
- [217] P. G. Kirton and A. D. Armour, *Nonlinear dynamics of a driven nanomechanical single-electron transistor*, Phys. Rev. B **87**, 155407 (2013).
- [218] T. J. Harvey, D. A. Rodrigues, and A. D. Armour, *Current noise of a superconducting single-electron transistor coupled to a resonator*, Phys. Rev. B **78**, 024513 (2008).
- [219] A. V. Khaetskii and Y. V. Nazarov, *Spin relaxation in semiconductor quantum dots*, Phys. Rev. B **61**, 12639 (2000).
- [220] H. O. H. Churchill, F. Kuemmeth, J. W. Harlow, A. J. Bestwick, E. I. Rashba, K. Flensberg, C. H. Stwertka, T. Taychatanapat, S. K. Watson, and C. M. Marcus, *Relaxation and Dephasing in a Two-Electron C₁₃ Nanotube Double Quantum Dot*, Phys. Rev. Lett. **102**, 166802 (2009).
- [221] W. D. Rice, R. T. Weber, P. Nikolaev, S. Arepalli, V. Berka, A.-L. Tsai, and J. Kono, *Spin relaxation times of single-wall carbon nanotubes*, Phys. Rev. B **88**, 041401 (2013).
- [222] C. Laurent, E. Flahaut, and A. Peigney, *The weight and density of carbon nanotubes versus the number of walls and diameter*, Carbon **48**, 2994 (2010).
- [223] G. Liu, Y. Zhao, K. Deng, Z. Liu, W. Chu, J. Chen, Y. Yang, K. Zheng, H. Huang, W. Ma, L. Song, H. Yang, C. Gu, G. Rao, C. Wang, S. Xie, and L. Sun, *Highly Dense and Perfectly Aligned Single-Walled Carbon Nanotubes Fabricated by Diamond Wire Drawing Dies*, Nano Lett. **8**, 1071 (2008).
- [224] H. B. Meerwaldt, G. A. Steele, and H. S. J. van der Zant, in *Fluctuating Nonlinear Oscillators*, edited by M. Dykman (Oxford University Press, 2012), pp. 312–340.
- [225] W. Yang, C. Urgell, S. L. De Bonis, M. Marganska, M. Grifoni, and A. Bachtold, *Crossover from Fabry-Pérot to charging oscillations in correlated carbon nanotubes*, arXiv:2003.08226 (2020).
- [226] F. Borjans, X. G. Croot, X. Mi, M. J. Gullans, and J. R. Petta, *Resonant microwave-mediated interactions between distant electron spins*, Nature **577**, 195 (2020).
- [227] M. Mantovani, W. Belzig, G. Rastelli, and R. Hussein, *Single-photon pump by Cooper-pair splitting*, Phys. Rev. Research **1**, 033098 (2019).
- [228] P. Recher, E. V. Sukhorukov, and D. Loss, *Andreev tunneling, Coulomb blockade, and resonant transport of nonlocal spin-entangled electrons*, Phys. Rev. B **63**, 165314 (2001).
- [229] D. Chevallier, J. Rech, T. Jonckheere, and T. Martin, *Current and noise correlations in a double-dot Cooper-pair beam splitter*, Phys. Rev. B **83**, 125421 (2011).
- [230] J. Rech, D. Chevallier, T. Jonckheere, and T. Martin, *Current correlations in an interacting Cooper-pair beam splitter*, Phys. Rev. B **85**, 035419 (2012).
- [231] Z. Scherübl, A. Pályi, and S. Csonka, *Probing individual split Cooper pairs using the spin qubit toolkit*, Phys. Rev. B **89**, 205439 (2014).
- [232] P. Trocha and I. Weymann, *Spin-resolved Andreev transport through double-quantum-dot Cooper pair splitters*, Phys. Rev. B **91**, 235424 (2015).
- [233] S. E. Nigg, R. P. Tiwari, S. Walter, and T. L. Schmidt, *Detecting nonlocal Cooper pair entanglement by optical Bell inequality violation*, Phys. Rev. B **91**, 94516 (2015).
- [234] A. Schroer and P. Recher, *Detection of nonlocal spin entanglement by light emission from a superconducting $p - n$ junction*, Phys. Rev. B **92**, 054514 (2015).
- [235] B. Probst, F. Domínguez, A. Schroer, A. L. Yeyati, and P. Recher, *Signatures of nonlocal Cooper-pair transport and of a singlet-triplet transition in the critical current of a double-quantum-dot Josephson junction*, Phys. Rev. B **94**, 155445 (2016).
- [236] F. Domínguez and A. L. Yeyati, *Quantum interference in a Cooper pair splitter: The three sites model*, Phys. E Low Dimens. Syst. Nanostruct. **75**, 322 (2016).
- [237] E. Amitai, R. P. Tiwari, S. Walter, T. L. Schmidt, and S. E. Nigg, *Nonlocal quantum state engineering with the Cooper pair splitter beyond the Coulomb blockade regime*, Phys. Rev. B **93**, 75421 (2016).
- [238] R. Hussein, L. Jaurigue, M. Governale, and A. Braggio, *Double quantum dot Cooper-pair splitter at finite couplings*, Phys. Rev. B **94**, 235134 (2016).
- [239] K. Wrześniewski, P. Trocha, and I. Weymann, *Current cross-correlations in double quantum dot based Cooper pair splitters with ferromagnetic leads*, J. Phys. Condens. Matter **29**, 195302 (2017).
- [240] N. Walldorf, C. Padurariu, A.-P. Jauho, and C. Flindt, *Electron Waiting Times of a Cooper Pair Splitter*, Phys. Rev. Lett. **120**, 087701 (2018).
- [241] K. Bocian, W. Rudziński, and I. Weymann, *Splitting efficiency and interference effects in a Cooper pair splitter based on a triple quantum dot with ferromagnetic contacts*, Phys. Rev. B **97**, 195441 (2018).

- [242] K. Wrześniewski and I. Weymann, *Current cross-correlations and waiting time distributions in Andreev transport through Cooper pair splitters based on a triple quantum dot system*, Phys. Rev. B **101**, 155409 (2020).
- [243] L. Hofstetter, S. Csonka, A. Baumgartner, G. Fülöp, S. d'Hollosy, J. Nygård, and C. Schönenberger, *Finite-bias Cooper pair splitting*, Phys. Rev. Lett. **107**, 136801 (2011).
- [244] A. Das, Y. Ronen, M. Heiblum, D. Mahalu, A. V. Kretinin, and H. Shtrikman, *High-efficiency Cooper pair splitting demonstrated by two-particle conductance resonance and positive noise cross-correlation*, Nat. Commun. **3**, 1165 (2012).
- [245] J. Schindele, A. Baumgartner, and C. Schönenberger, *Near-Unity Cooper Pair Splitting Efficiency*, Phys. Rev. Lett. **109**, 157002 (2012).
- [246] J. Schindele, A. Baumgartner, R. Maurand, M. Weiss, and C. Schönenberger, *Nonlocal spectroscopy of Andreev bound states*, Phys. Rev. B **89**, 045422 (2014).
- [247] G. Fülöp, S. d'Hollosy, A. Baumgartner, P. Makk, V. A. Guzenko, M. H. Madsen, J. Nygård, C. Schönenberger, and S. Csonka, *Local electrical tuning of the nonlocal signals in a Cooper pair splitter*, Phys. Rev. B **90**, 235412 (2014).
- [248] G. Fülöp, F. Domínguez, S. d'Hollosy, A. Baumgartner, P. Makk, M. H. Madsen, V. A. Guzenko, J. Nygård, C. Schönenberger, A. Levy Yeyati, and S. Csonka, *Magnetic Field Tuning and Quantum Interference in a Cooper Pair Splitter*, Phys. Rev. Lett. **115**, 227003 (2015).
- [249] Z. B. Tan, D. Cox, T. Nieminen, P. Lähteenmäki, D. Golubev, G. B. Lesovik, and P. J. Hakonen, *Cooper Pair Splitting by Means of Graphene Quantum Dots*, Phys. Rev. Lett. **114**, 96602 (2015).
- [250] I. V. Borzenets, Y. Shimazaki, G. F. Jones, M. F. Craciun, S. Russo, M. Yamamoto, and S. Tarucha, *High Efficiency CVD Graphene-lead (Pb) Cooper Pair Splitter*, Sci. Rep. **6**, 23051 (2016).
- [251] S. Baba, C. Jünger, S. Matsuo, A. Baumgartner, Y. Sato, H. Kamata, K. Li, S. Jeppesen, L. Samuelson, H. Q. Xu, C. Schönenberger, and S. Tarucha, *Cooper-pair splitting in two parallel InAs nanowires*, New J. Phys. **20**, 063021 (2018).
- [252] Z. Cao, T.-F. Fang, L. Li, and H.-G. Luo, *Thermoelectric-induced unitary Cooper pair splitting efficiency*, Appl. Phys. Lett. **107**, 212601 (2015).
- [253] R. Sánchez, P. Burset, and A. L. Yeyati, *Cooling by Cooper pair splitting*, Phys. Rev. B **98**, 241414(R) (2018).
- [254] R. Hussein, M. Governale, S. Kohler, W. Belzig, F. Giazotto, and A. Braggio, *Nonlocal thermoelectricity in a Cooper-pair splitter*, Phys. Rev. B **99**, 075429 (2019).
- [255] N. S. Kirsanov, Z. B. Tan, D. S. Golubev, P. J. Hakonen, and G. B. Lesovik, *Heat switch and thermoelectric effects based on Cooper-pair splitting and elastic cotunneling*, Phys. Rev. B **99**, 115127 (2019).
- [256] P. P. Hofer, J.-R. Souquet, and A. A. Clerk, *Quantum heat engine based on photon-assisted Cooper pair tunneling*, Phys. Rev. B **93**, 041418 (2016).
- [257] A. Ronzani, B. Karimi, J. Senior, Y.-C. Chang, J. T. Peltonen, C. Chen, and J. P. Pekola, *Tunable photonic heat transport in a quantum heat valve*, Nat. Phys. **14**, 991 (2018).
- [258] S. Dambach, P. Egetmeyer, J. Ankerhold, and B. Kubala, *Quantum thermodynamics with a Josephson-photonics setup*, Eur. Phys. J. Spec. Top. **227**, 2053 (2019).
- [259] J. Senior, A. Gubaydullin, B. Karimi, J. T. Peltonen, J. Ankerhold, and J. P. Pekola, *Heat rectification via a superconducting artificial atom*, Commun. Phys. **3**, 1 (2020).
- [260] G. Thomas, A. Gubaydullin, D. S. Golubev, and J. P. Pekola, *Thermally pumped on-chip maser*, arXiv:2003.12199 (2020).
- [261] P. A. Erdman, F. Mazza, R. Bosisio, G. Benenti, R. Fazio, and F. Taddei, *Thermoelectric properties of an interacting quantum dot based heat engine*, Phys. Rev. B **95**, 245432 (2017).
- [262] P. A. Erdman, B. Bhandari, R. Fazio, J. P. Pekola, and F. Taddei, *Absorption refrigerators based on Coulomb-coupled single-electron systems*, Phys. Rev. B **98**, 45433 (2018).
- [263] B. Dutta, D. Majidi, N. W. Talarico, N. L. Gullo, C. B. Winkelmann, and H. Courtois, *A Single-Quantum-Dot Heat Valve*, arXiv:2001.08183 (2020).
- [264] A. V. Rozhkov and D. P. Arovas, *Interacting-impurity Josephson junction: Variational wave functions and slave-boson mean-field theory*, Phys. Rev. B **62**, 6687 (2000).
- [265] J. Eldridge, M. G. Pala, M. Governale, and J. König, *Superconducting proximity effect in interacting double-dot systems*, Phys. Rev. B **82**, 184507 (2010).
- [266] J. Gramich, A. Baumgartner, and C. Schönenberger, *Resonant and Inelastic Andreev Tunneling Observed on a Carbon Nanotube Quantum Dot*, Phys. Rev. Lett. **115**, 216801 (2015).
- [267] G.-W. Deng, D. Wei, S. X. Li, J. R. Johansson, W. C. Kong, H. O. Li, G. Cao, M. Xiao, G.-C. Guo, F. Nori, H. W. Jiang, and G.-P. Guo, *Coupling Two Distant Double Quantum Dots with a Microwave Resonator*, Nano Lett. **15**, 6620 (2015).

- [268] O. Sauret, D. Feinberg, and T. Martin, *Quantum master equations for the superconductor-quantum dot entangler*, Phys. Rev. B **70**, 245313 (2004).
- [269] M. Governale, M. G. Pala, and J. König, *Real-time diagrammatic approach to transport through interacting quantum dots with normal and superconducting leads*, Phys. Rev. B **77**, 134513 (2008).
- [270] G. Benenti, G. Casati, K. Saito, and R. S. S. Whitney, *Fundamental aspects of steady-state conversion of heat to work at the nanoscale*, Phys. Rep. **694**, 1 (2017).
- [271] L. N. Trefethen and D. Bau, *Numerical linear algebra* (Society for Industrial and Applied Mathematics, Philadelphia, 1997).
- [272] G. Lang and Y. A. Firsov, *Kinetic Theory of Semiconductors with Low Mobility*, Zh. Eksp. Teor. Fiz. **43**, 1843 (1962).
- [273] T. Brandes and B. Kramer, *Spontaneous Emission of Phonons by Coupled Quantum Dots*, Phys. Rev. Lett. **83**, 3021 (1999).
- [274] T. Brandes, *Coherent and collective quantum optical effects in mesoscopic systems*, Phys. Rep. **408**, 315 (2005).
- [275] H. Okamoto, A. Gourgout, C.-Y. Chang, K. Onomitsu, I. Mahboob, E. Y. Chang, and H. Yamaguchi, *Coherent phonon manipulation in coupled mechanical resonators*, Nat. Phys. **9**, 480 (2013).
- [276] D. Zhu, X.-H. Wang, W.-C. Kong, G.-W. Deng, J.-T. Wang, H.-O. Li, G. Cao, M. Xiao, K.-L. Jiang, X.-C. Dai, G.-C. Guo, F. Nori, and G.-P. Guo, *Coherent Phonon Rabi Oscillations with a High-Frequency Carbon Nanotube Phonon Cavity*, Nano Lett. **17**, 915 (2017).
- [277] A. Stockklauser, P. Scarlino, J. V. Koski, S. Gasparinetti, C. K. Andersen, C. Reichl, W. Wegscheider, T. Ihn, K. Ensslin, and A. Wallraff, *Strong Coupling Cavity QED with Gate-Defined Double Quantum Dots Enabled by a High Impedance Resonator*, Phys. Rev. X **7**, 011030 (2017).
- [278] W. T. Morley, A. Di Marco, **M. Mantovani**, P. Stadler, W. Belzig, G. Rastelli, and A. D. Armour, *Theory of double Cooper-pair tunneling and light emission mediated by a resonator*, Phys. Rev. B **100**, 054515 (2019).
- [279] R. Berndt, J. K. Gimzewski, and P. Johansson, *Inelastic tunneling excitation of tip-induced plasmon modes on noble-metal surfaces*, Phys. Rev. Lett. **67**, 3796 (1991).
- [280] R. Berndt, J. K. Gimzewski, and P. Johansson, *Electromagnetic interactions of metallic objects in nanometer proximity*, Phys. Rev. Lett. **71**, 3493 (1993).
- [281] T. Holst, D. Esteve, C. Urbina, and M. H. Devoret, *Effect of a Transmission Line Resonator on a Small Capacitance Tunnel Junction*, Phys. Rev. Lett. **73**, 3455 (1994).
- [282] T. Atay, J.-H. Song, and A. V. Nurmikko, *Strongly Interacting Plasmon Nanoparticle Pairs: From Dipole-Dipole Interaction to Conductively Coupled Regime*, Nano Lett. **4**, 1627 (2004).
- [283] N. L. Schneider, G. Schull, and R. Berndt, *Optical Probe of Quantum Shot-Noise Reduction at a Single-Atom Contact*, Phys. Rev. Lett. **105**, 026601 (2010).
- [284] M. Hofheinz, F. Portier, Q. Baudouin, P. Joyez, D. Vion, P. Bertet, P. Roche, and D. Esteve, *Bright Side of the Coulomb Blockade*, Phys. Rev. Lett. **106**, 217005 (2011).
- [285] P.-J. Peters, F. Xu, K. Kaasbjerg, G. Rastelli, W. Belzig, and R. Berndt, *Quantum Coherent Multielectron Processes in an Atomic Scale Contact*, Phys. Rev. Lett. **119**, 066803 (2017).
- [286] F. Xu, C. Holmqvist, and W. Belzig, *Overbias Light Emission due to Higher-Order Quantum Noise in a Tunnel Junction*, Phys. Rev. Lett. **113**, 066801 (2014).
- [287] K. Kaasbjerg and A. Nitzan, *Theory of light emission from quantum noise in plasmonic contacts: Above-threshold emission from higher-order electron-plasmon scattering*, Phys. Rev. Lett. **114**, 126803 (2015).
- [288] F. Xu, C. Holmqvist, G. Rastelli, and W. Belzig, *Dynamical Coulomb blockade theory of plasmon-mediated light emission from a tunnel junction*, Phys. Rev. B **94**, 245111 (2016).
- [289] A. Imamoğlu, H. Schmidt, G. Woods, and M. Deutsch, *Strongly Interacting Photons in a Nonlinear Cavity*, Phys. Rev. Lett. **79**, 1467 (1997).
- [290] A. Biella, L. Mazza, I. Carusotto, D. Rossini, and R. Fazio, *Photon transport in a dissipative chain of nonlinear cavities*, Phys. Rev. A **91**, 053815 (2015).
- [291] C. Vaneph, A. Morvan, G. Aiello, M. Féchant, M. Aprili, J. Gabelli, and J. Estève, *Observation of the Unconventional Photon Blockade in the Microwave Domain*, Phys. Rev. Lett. **121**, 043602 (2018).
- [292] D. E. Chang, V. Vuletić, and M. D. Lukin, *Quantum nonlinear optics — photon by photon*, Nat. Photonics **8**, 685 (2014).
- [293] A. Grimm, F. Blanchet, R. Albert, J. Leppäkangas, S. Jebari, D. Hazra, F. Gustavo, J.-L. Thomassin, E. Dupont-Ferrier, F. Portier, and M. Hofheinz, *Bright On-Demand Source of Antibunched Microwave Photons Based on Inelastic Cooper Pair Tunneling*, Phys. Rev. X **9**, 021016 (2019).

- [294] C. Rolland, A. Peugeot, S. Dambach, M. Westig, B. Kubala, Y. Mukharsky, C. Altimiras, H. le Sueur, P. Joyez, D. Vion, P. Roche, D. Esteve, J. Ankerhold, and F. Portier, *Antibunched Photons Emitted by a dc-Biased Josephson Junction*, Phys. Rev. Lett. **122**, 186804 (2019).
- [295] A. D. Armour, M. P. Blencowe, E. Brahim, and A. J. Rimberg, *Universal Quantum Fluctuations of a Cavity Mode Driven by a Josephson Junction*, Phys. Rev. Lett. **111**, 247001 (2013).
- [296] S. Meister, M. Mecklenburg, V. Gramich, J. T. Stockburger, J. Ankerhold, and B. Kubala, *Resonators coupled to voltage-biased Josephson junctions: From linear response to strongly driven nonlinear oscillations*, Phys. Rev. B **92**, 174532 (2015).
- [297] V. Gramich, B. Kubala, S. Rohrer, and J. Ankerhold, *From Coulomb-Blockade to Nonlinear Quantum Dynamics in a Superconducting Circuit with a Resonator*, Phys. Rev. Lett. **111**, 247002 (2013).
- [298] U. Vool and M. Devoret, *Introduction to quantum electromagnetic circuits*, Int. J. Circ. Theor. Appl. **45**, 897 (2017).
- [299] N. Lörch, C. Bruder, N. Brunner, and P. P. Hofer, *Optimal work extraction from quantum states by photo-assisted Cooper pair tunneling*, Quantum Sci. Technol. **3**, 035014 (2018).
- [300] H. Wang, M. P. Blencowe, A. D. Armour, and A. J. Rimberg, *Quantum dynamics of a Josephson junction driven cavity mode system in the presence of voltage bias noise*, Phys. Rev. B **96**, 104503 (2017).
- [301] C. Padurariu, F. Hassler, and Y. V. Nazarov, *Statistics of radiation at Josephson parametric resonance*, Phys. Rev. B **86**, 054514 (2012).
- [302] J. Leppäkangas, G. Johansson, M. Marthaler, and M. Fogelström, *Nonclassical Photon Pair Production in a Voltage-Biased Josephson Junction*, Phys. Rev. Lett. **110**, 267004 (2013).
- [303] A. D. Armour, B. Kubala, and J. Ankerhold, *Josephson photonics with a two-mode superconducting circuit*, Phys. Rev. B **91**, 184508 (2015).
- [304] M. Trif and P. Simon, *Photon cross-correlations emitted by a Josephson junction in two microwave cavities*, Phys. Rev. B **92**, 014503 (2015).
- [305] S. Dambach, B. Kubala, V. Gramich, and J. Ankerhold, *Time-resolved statistics of nonclassical light in Josephson photonics*, Phys. Rev. B **92**, 054508 (2015).
- [306] J. Leppäkangas, M. Fogelström, A. Grimm, M. Hofheinz, M. Marthaler, and G. Johansson, *Antibunched Photons from Inelastic Cooper-Pair Tunneling*, Phys. Rev. Lett. **115**, 027004 (2015).
- [307] J.-R. Souquet and A. A. Clerk, *Fock-state stabilization and emission in superconducting circuits using dc-biased Josephson junctions*, Phys. Rev. A **93**, 060301 (2016).
- [308] J. Leppäkangas and M. Marthaler, *Inelastic scattering of microwave radiation in the dynamical Coulomb blockade*, Phys. Rev. B **98**, 224511 (2018).
- [309] U. C. Mendes, S. Jezouin, P. Joyez, B. Reulet, A. Blais, F. Portier, C. Mora, and C. Altimiras, *Parametric amplification and squeezing with an ac- and dc-voltage biased superconducting junction*, Phys. Rev. Applied **11**, 034035 (2019).
- [310] L. Arndt and F. Hassler, *Statistics of radiation due to nondegenerate Josephson parametric down-conversion*, Phys. Rev. B **100**, 014505 (2019).
- [311] M. Westig, B. Kubala, O. Parlavacchio, Y. Mukharsky, C. Altimiras, P. Joyez, D. Vion, P. Roche, D. Esteve, M. Hofheinz, M. Trif, P. Simon, J. Ankerhold, and F. Portier, *Emission of Nonclassical Radiation by Inelastic Cooper Pair Tunneling*, Phys. Rev. Lett. **119**, 137001 (2017).
- [312] S. Jebari, F. Blanchet, A. Grimm, D. Hazra, R. Albert, P. Joyez, D. Vion, D. Estève, F. Portier, and M. Hofheinz, *Near-quantum-limited amplification from inelastic Cooper-pair tunnelling*, Nat. Electron. **1**, 223 (2018).
- [313] D. F. V. James and J. Jerke, *Effective Hamiltonian theory and its applications in quantum information*, Can. J. Phys. **85**, 625 (2007).
- [314] O. Gamel and D. F. V. James, *Time-averaged quantum dynamics and the validity of the effective Hamiltonian model*, Phys. Rev. A **82**, 052106 (2010).
- [315] J. Johansson, P. Nation, and F. Nori, *QuTiP 2: A Python framework for the dynamics of open quantum systems*, Comput. Phys. Commun. **184**, 1234 (2013).
- [316] A. D. Armour, B. Kubala, and J. Ankerhold, *Noise switching at a dynamical critical point in a cavity-conductor hybrid*, Phys. Rev. B **96**, 214509 (2017).
- [317] A. A. Clerk, in *New Directions in Mesoscopic Physics (Towards Nanoscience)*, edited by R. Fazio, V. F. Gantmakher, and Y. Imry, NATO Science Series (Springer Netherlands, Dordrecht, 2003), pp. 325–337.
- [318] H. Grabert and G.-L. Ingold, *Identification of Coulomb blockade and macroscopic quantum tunneling by noise*, Europhys. Lett. **58**, 429 (2002).
- [319] K. M. Birnbaum, A. Boca, R. Miller, A. D. Boozer, T. E. Northup, and H. J. Kimble, *Photon blockade in an optical cavity with one trapped atom*, Nature **436**, 87 (2005).

- [320] C. R. Ast, B. Jäck, J. Senkpiel, M. Eltschka, M. Etzkorn, J. Ankerhold, and K. Kern, *Sensing the quantum limit in scanning tunnelling spectroscopy*, Nat. Commun. **7**, 1 (2016).
- [321] A. Cottet, *Probing coherent Cooper pair splitting with cavity photons*, Phys. Rev. B **90**, 125139 (2014).
- [322] L. E. Bruhat, T. Cubaynes, J. J. Vienne, M. C. Dartailh, M. M. Desjardins, A. Cottet, and T. Kontos, *Circuit QED with a quantum-dot charge qubit dressed by Cooper pairs*, Phys. Rev. B **98**, 155313 (2018).
- [323] L. Mandel, *Sub-Poissonian photon statistics in resonance fluorescence*, Optics Lett. **4**, 205 (1979).
- [324] R. J. Cook, *Photon number statistics in resonance fluorescence*, Phys. Rev. A **23**, 1243 (1981).
- [325] C. Flindt, T. Novotný, and A.-P. Jauho, *Current noise in a vibrating quantum dot array*, Phys. Rev. B **70**, 205334 (2004).
- [326] C. Flindt, T. Novotný, A. Braggio, and A.-P. Jauho, *Counting statistics of transport through Coulomb blockade nanostructures: High-order cumulants and non-Markovian effects*, Phys. Rev. B **82**, 155407 (2010).